DISSERTATION

# EXPERIMENTAL FLUME AND NUMERICAL STUDIES INTO THE INFLUENCE OF FLOODPLAIN VEGETATION ON RIVER-CORRIDOR HYDRODYNAMIC PROCESSES

Submitted by

Daniel C. White

Department of Civil and Environmental Engineering

In partial fulfillment of the requirements

For the Degree of Doctor of Philosophy

Colorado State University

Fort Collins, Colorado

Fall 2023

Doctoral Committee:

Advisor: Ryan Morrison
Co-Advisor: Peter Nelson

Chris Thornton
Sara Rathburn

# ABSTRACT

## EXPERIMENTAL FLUME AND NUMERICAL STUDIES INTO THE INFLUENCE OF FLOODPLAIN VEGETATION ON RIVER-CORRIDOR HYDRODYNAMIC PROCESSES

The active channel has historically been the primary focus of river hydrodynamic process studies and river engineering. However, increased global flood risk and awareness of ecosystem services provided by floodplains has encouraged managers to broaden their perspective beyond the banks. As water exits and reenters the channel during floods, water, nutrients, and sediment are exchanged with the floodplain. This flux is heavily influenced by both channel-floodplain hydrologic connectivity, or the ability of water to access the floodplain, and by floodplain land cover types. River and hydrologic modifications that result in disconnected floodplains include channel planform and cross-section geometry alterations, diversions and dams, levees, land cover change, and river sediment mining. As river managers, land-use managers, and landowners acknowledge the benefits of functional, laterally connected river corridors, more river restoration projects are undertaken with a primary goal of reconnecting a river channel to the adjacent floodplain.

A major component of large river restoration and river engineering projects includes designing for and predicting future flow scenarios using hydraulic models and other analytical methods. Developing a hydraulic model for river restoration design relies on the theory and science of fluvial morphodynamic processes as well as the parameterization of hydraulic roughness coefficients. Because of the historical emphasis on in-channel processes, the scientific literature related to channel-floodplain hydrodynamics and floodplain roughness

parameterization is sparse. Specifically, there are limited studies investigating the influence of vegetation on channel-floodplain exchange flow, lateral connectivity, and resulting channel topography.

To address this knowledge gap, I conducted a series of physical and numerical modeling experiments where floodplain vegetation and flow parameters were varied. In Chapters 2 and 3, I present the results of flume experiments where I measured bedform topography and the flow field under varied floodplain vegetation conditions at two overbank flow depths. The experiments were conducted in a 1-m wide meandering compound channel inset in a 15.4-m long, 4.9-m wide basin. The channel bed was a mobile sand-and-gravel mixture with a median sediment size of 3.3 mm, and sediment transport occurred only within the channel. I tested bare and vegetated floodplain conditions with 2.7-cm diameter rigid emergent vegetation elements at spacings of 3.0 units $m^{-2}$ and 12.1 units $m^{-2}$. My observations of the flow field indicate that high density vegetation enhances secondary circular flow through the meander bend and reduces momentum exchange at the channel-floodplain interface. At a low relative depth, flow through high density vegetation was deflected away from the down-valley direction and forced to reenter the channel at a steep angle with respect to the channel centerline. However, at a high relative depth, dense vegetation steered in-channel surface flows more closely following the channel centerline. These observations shed light on the hydrodynamic processes leading to flood wave attenuation, enhanced nutrient cycling, and channel altering stresses, and these results may inform river restoration riparian management best practices.

To investigate bedform response, I performed a moving-window analysis of topographic surface metrics including skewness, coefficient of variation, and standard deviation, as well as topographic patch analysis of area and contagion to measure changes in bedform heterogeneity

as flow depth and vegetation density were varied. My results show that both greater density vegetation and larger flows can increase bedform topographic heterogeneity. These findings suggest that floodplain vegetation and natural hydrologic regimes that include overbank flows can enhance stream habitat complexity. Designing for the effects of established vegetation conditions and prioritizing floodplain vegetation planting may be useful for river managers striving to achieve successful biomic river restoration.

Expanding on the observations made in the flume, I explored the ability of a 2D hydraulic model to predict the effects of vegetation on meandering channel flow dynamics. I used the TreeLS point cloud processing tool to automatically extract woody floodplain vegetation characteristics and estimate Manning's roughness coefficients for vegetation from aerial LiDAR. I investigated the influence of varied vegetation densities on channel-floodplain exchange flows in HEC-RAS 2D. I developed hydraulic models for three reaches along the Butokamabetsu River in the Hokkaido University Uryu Experimental Forest in Northern Japan where each reach had distinct biogeomorphic characteristics including channel width, slope, sinuosity, and floodplain vegetation density. I found that in the lower gradient, higher sinuosity reaches, floodplain vegetation density had more influence on channel-floodplain exchange flow attenuation. These results highlight the importance of planning for the presence and density of vegetation in river restoration projects particularly in lower gradient, more sinuous stretches of river.

The results and analysis presented in this dissertation suggest that biological drivers such as rigid emergent floodplain vegetation play an important role in river form and function particularly in conjunction with floods that occasionally access the floodplain. These detailed observations of flow, sediment, and resulting bed morphology as well as analysis of innovative

remote sensing techniques provide a basis for an improved understanding of morphodynamic processes in meandering rivers.

# ACKNOWLEDGEMENTS

First, I would like to thank my advisors Peter Nelson and Ryan Morrison. Their willingness to work with and trust me as I've carried out dissertation research while balancing time away from the lab as a parent has resulted in an extremely positive graduate school experience. Since my master's project, Peter has and continues to inspire me to do rigorous, thorough research by approaching scientific questions with an experimental mindset. I feel very fortunate to have worked with both Peter and Ryan and I can't imagine a better PhD advisor pair. Ryan has consistently looked to involve me in collaborative research opportunities, which has given me invaluable experiences that I'm certain will propel me toward a career in river science. To both Ryan and Peter, thank you for your guidance in this journey, and more importantly for your friendship.

I'm grateful to my committee members Chris Thornton and Sara Rathburn. Constructing and running the flume experiments came with many challenges, not the least of which was the covid lockdown, but thanks to Chris' recommendations I was able to overcome the obstacles I encountered. I'm fortunate to have taken classes from Sara and collaborated with her on other research projects. Sara's genuine excitement for river science is contagious and inspires me to not only be a good scientist, but to live the science and passion for the natural systems we work in. Sara has also been an excellent mentor, providing invaluable career advice and personal support for which I am extremely grateful. Ellen Wohl has participated as my committee member throughout the course of my graduate studies. I have been fortunate to spend a great deal of time with Ellen in the field thinking about and appreciating rivers. She has had a significant influence

on my perspective of fluvial processes, and I will fondly remember the moments I spent learning from her as she so generously shared her wisdom and mentorship.

There are many individuals that contributed to this dissertation through data collection, experimental setup, scientific discussion, content review and feedback, and other forms of support. The flume experiments could not have been completed without the help of Ali Fakhri, Taylor Hogan, Matt Szydlowski, Scott Zusi, Donovan Sweeney, Jeff Ellis, Nick Brouillard, Anna Wikowski, Evan Malloy, Megan Bock, Celeste Wieting, and Collin Barry,

Past and current lab mates have given helpful feedback on presentations, manuscript drafts, many other helpful conversations, and by helping with Lars: Dan Brogan, Ryan Brown, David Cortese, Nick Brouillard, Lindsey Hayter, Phoebe White, Johnny Murray, Elaina Pasero, Marissa Karpack, Kira Simonson, Brady Jones, Evan Shulz, Nick Christensen, Mattea Mobley, and Ashar Ali. To others I have spent time with doing field work for this and other projects, I'm grateful for your friendship and for lively discussions about rivers: Juli Scamardo, John Kemper, Sarah Hinshaw, Sarah Dunn, Anna Marshall, Shayla Triantafillou, Aaron Katz, Emily Iskin, Mickey Means-Brows, Hiromi Uno and others.

Most importantly, I would like to thank Rachelle for her unwavering support and encouragement to pursue advanced degrees doing something I love despite the associated significant sacrifices. I certainly would not have followed this academic trajectory if she hadn't encouraged me to do so. The last two years of my PhD have been extremely meaningful as I have had the chance to not only be Rachelle's partner, but to share in the responsibility and blessing of being a parent to our son Lars and preparing for the birth of our second son. It wasn't easy, but I will always remember these years with fondness.

TABLE OF CONTENTS

LIST OF TABLES

LIST OF FIGURES

# CHAPTER 1: INTRODUCTION

River studies and associated engineering analyses are often conducted with a singular focus on the active channel commonly defined as the area which will convey a peak discharge with a 1-to-2-year recurrence interval. These flows have been described as those which are largely responsible for equilibrium channel form (Andrews, 1980). Rigorous scientific studies of bankfull form and process extend back over a century and often rely on conceptual models to qualitatively describe the physical processes that underpin a channel's geomorphic trajectory through time and equilibrium states (Langbein & Leopold, 1964). These models typically account for a channel's slope, sediment availability, particle size distribution, bank material, and flow (e.g. Lane, 1955; Schumm et al., 1984). As water flows through a river, it meets resistance due to bedforms, particle size, channel planform, vegetation, and wood. Of these roughness elements, vegetation and wood are the least studied and the influence of vegetation on channel equilibrium and morphology is poorly understood, although they are increasingly seen as important elements of river corridor hydrodynamic and ecosystem processes (Buffington & Montgomery, 1999; Gurnell et al., 2002; Nepf, 2012). Even more sparse in the scientific literature is the study of the cross-section-to-reach-scale hydraulics of floods and floodplain flows, the influence of floodplain vegetation, and resulting bed morphology.

A channel-centric approach to river hydraulic and geomorphic analysis may neglect other hydrodynamic interactions that are responsible for maintaining aquatic habitat, influencing channel form, and promoting riparian resilience (Harvey & Gooseff, 2015; Poff et al., 1997; Thoms, 2003). In rivers with a high degree of lateral hydrologic connectivity, or the ability of water to move from the active channel to off-channel environments, ecosystem services such as

flood wave attenuation (Sholtes & Doyle, 2011), nutrient cycling (Baldwin & Mitchell, 2000), and habitat provisioning (Benke, 2001; Junk et al., 1989) are often enhanced. These services are commonly identified as river management goals and may be specific desirable outcomes of river restoration projects. In recent decades, river restoration monitoring and design tools have progressed significantly allowing practitioners to predict hydraulic conditions under a range of flows within the active channel. Monitoring and surveying tools have expanded dramatically to commonly include the use of aerial imagery, LiDAR and handheld GNSS to accurately characterize the river corridor topographic surface and monitor change. The topographic surface is often used as the base for computational grids in 1D, 2D, and occasionally 3D numerical models in river restoration design and analysis. However, accurately surveying or parameterizing flow resistance due to vegetation, whether live or dead, in river corridors remains very difficult because: 1. there is a lack of a qualitative framework describing the influence of vegetation on quasi-equilibrium channel morphodynamics; 2. numerically resolving the hydraulics of flow through river corridors with vegetation is very complex and computationally expensive; and 3. there are few tools available that allow practitioners to accurately estimate flow resistance due to vegetation.

In this dissertation, I present the results of physical and numerical experimental studies that aim to address the three listed problems above directly and indirectly. I conducted these experiments with testable hypotheses investigating river processes such as sediment, topography, and flow within the active channel, as well as floodplain processes which are often strongly tied to the presence of rigid emergent vegetation.

In Chapters 2 and 3, I describe a series of meandering channel flume experiments that I conducted at Colorado State University's Engineering Research Center. The channel was 1-m

wide and inset in a 15.4-m long, 4.9-m wide basin (Figure 1). I simulated flow through the flume with multiple floodplain vegetation configurations that roughly scale to a medium-sized river 15-m across with trees similar in diameter to cottonwoods found in the western United States. I investigated the influence of floodplain vegetation density on the flow field and resulting sediment transport and bed morphology. The focus of Chapter 2 is the quasi-equilibrium bed topography that developed during each of seven flume runs. In these experiments I define quasi-equilibrium as channel topography that is neither aggrading nor incising. I found that greater floodplain vegetation density produced more topographically complex bedforms. I also found that at overbank flow sediment transport was greater than at bankfull flow which is distinct from another flume study investigating meandering channel flows with a mobile bed of sand (Shiono et al., 2009a, 2009b). This may be a result of the low sinuosity or coarse particles used in this experiment.

The focus of Chapter 3 is analysis of the flow field that developed during each of the seven experimental flume runs as well as the influence of vegetation density on channel-floodplain exchange flow. I analyzed the flow field and identified mechanisms associated with floodplain vegetation that led to varied secondary flow patterns for all seven flume runs. I also followed a mass balance approach to quantify flux at the left and right channel banks similar to methods presented by Czuba et al. (2019) and Stone et al. (2017). I found that the influence of floodplain vegetation on meandering compound channel flow is highly three-dimensional and that using a depth-averaged/2D approach to estimate channel forming forces may not fully capture the influence of 3D flow field.

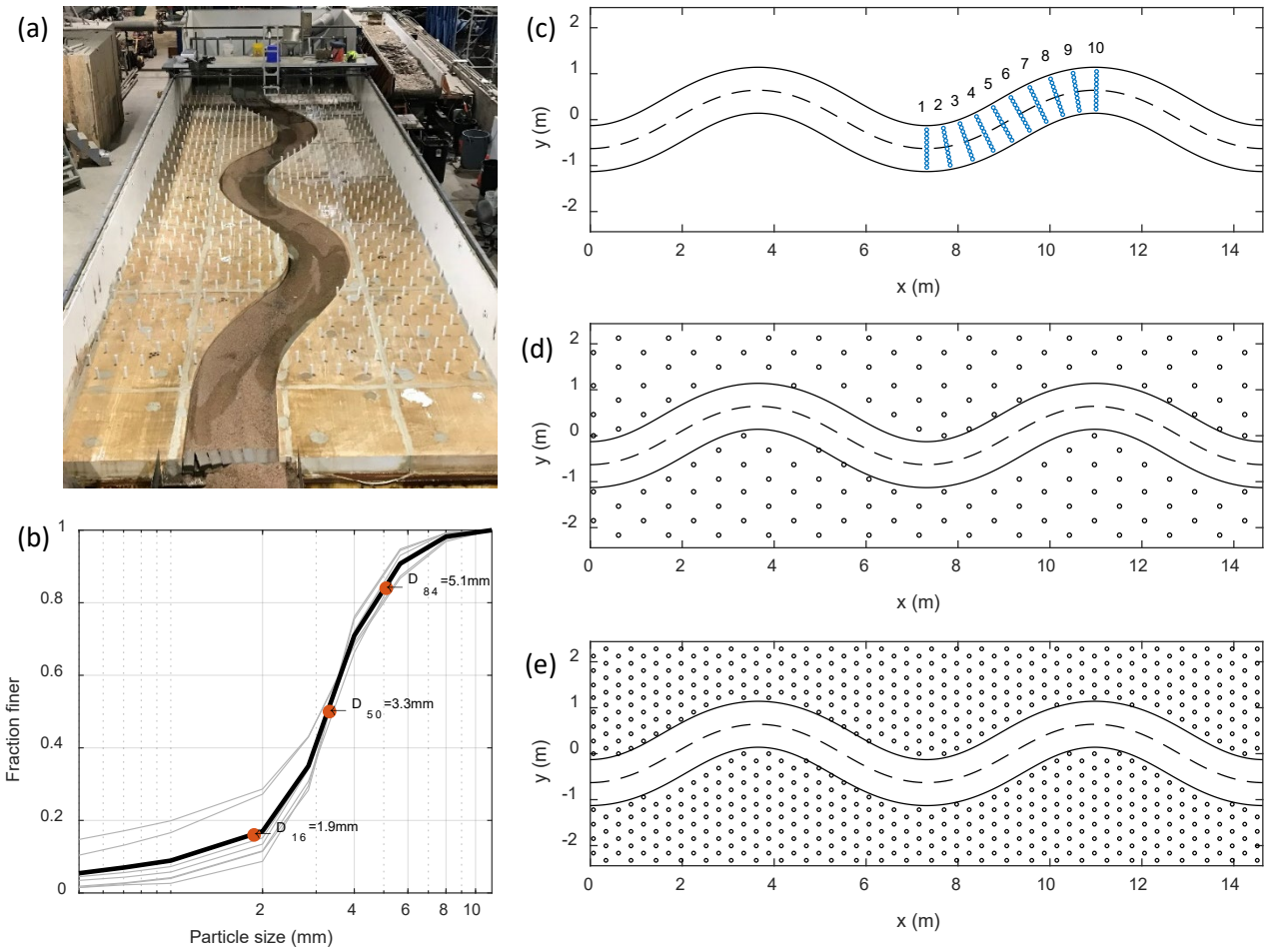


**Figure 1.1.** Meandering channel flume experimental setup described in Chapters 2 and 3. (a) Photo of flume setup. (b) Mobile bed and sediment feed grain size distribution. (c) Cross section location in half meander where flow measurements were taken. (d) Low-density vegetation configuration. (e) High-density vegetation configuration.

The results and analysis that emerged from Chapters 2 and 3 prompted further investigation into the influence of floodplain vegetation in a natural river and the ability of 2D hydraulic simulations to capture the effects of floodplain vegetation on channel-floodplain exchange as reported in Chapters 1 and 2. To do this, I explored remote sensing methods using aerial LiDAR to characterize large woody vegetation in the Butokamabetsu River in Hokkaido, Japan.

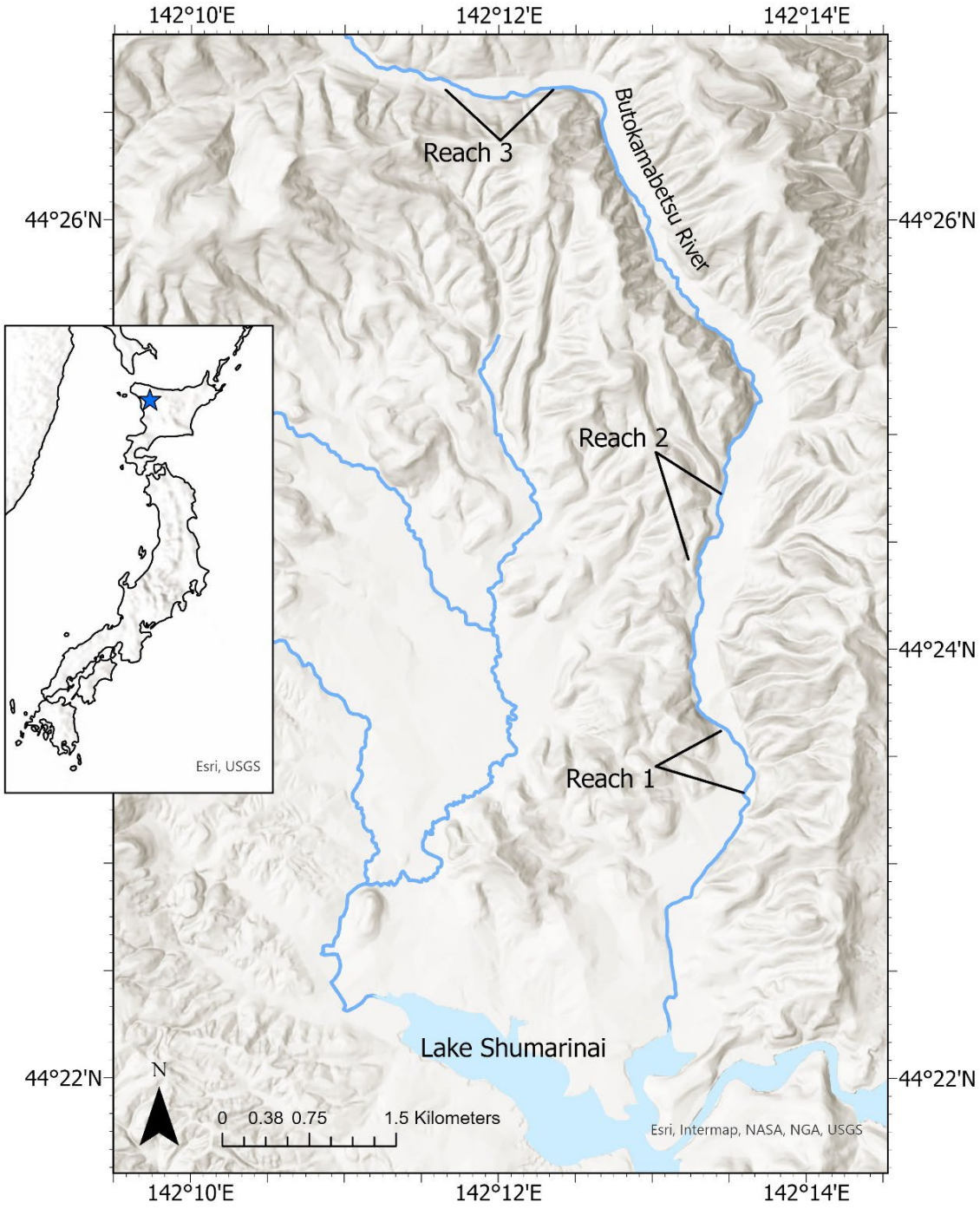


**Figure 1.2.** Location of Reaches 1, 2, and 3 where hydrodynamic models were developed in HEC-RAS 2D

The vegetation classification was then used to parameterize Manning's n in four hydrodynamic modeling scenarios in HEC-RAS 2D. In this study, the intended purpose was not

to accurately calibrate Manning's roughness across the floodplain, but to perform a series of numerical experimental simulations where I estimate hydraulic roughness due to the large rigid woody vegetation elements and artificially simulate variations in floodplain vegetation density. I then measure channel-floodplain connectivity by computing exchange flow at the left and right banks. In this study, I found that for reaches with higher sinuosity and lower slope, dense floodplain vegetation has a greater influence on channel-floodplain exchange flow than in reaches with high slope and low sinuosity. I also found that topographic depressions and side channels were the primary driver of channel-floodplain exchange flow.

In Chapter 5, I provide a concise summary of the findings presented in Chapters 2 through 4 and highlight the results in the context of river management applications.

## 1.1 References


Andrews, E. D. (1980). Effective and bankfull discharges of streams in the Yampa River basin, Colorado and Wyoming. *Journal of Hydrology*, *46*(3), 311–330. https://doi.org/10.1016/0022-1694(80)90084-0

Baldwin, D. S., & Mitchell, A. (2000). The effects of drying and re-flooding on the sediment and soil nutrient dynamics of lowland river–floodplain systems: a synthesis. *Regulated Rivers: Research & Management: An International Journal Devoted to River Research and Management*, *16*(5), 457–467.

Benke, A. C. (2001). Importance of flood regime to invertebrate habitat in an unregulated river–floodplain ecosystem. *Journal of the North American Benthological Society*, *20*(2), 225–240.

Buffington, J. M., & Montgomery, D. R. (1999). Effects of hydraulic roughness on surface textures of gravel-bed rivers. *Water Resources Research*, *35*(11), 3507–3521. https://doi.org/10.1029/1999WR900138

Czuba, J. A., David, S. R., Edmonds, D. A., & Ward, A. S. (2019). Dynamics of Surface-Water Connectivity in a Low-Gradient Meandering River Floodplain. *Water Resources Research*, *55*(3), 1849–1870. https://doi.org/10.1029/2018WR023527

Gurnell, A. M., Piégay, H., Swanson, F. J., & Gregory, S. V. (2002). Large wood and fluvial processes. *Freshwater Biology*, *47*(4), 601–619.

Harvey, J., & Gooseff, M. (2015). River corridor science: Hydrologic exchange and ecological consequences from bedforms to basins. *Water Resources Research*, *51*(9), 6893–6922. https://doi.org/10.1002/2015WR017617

Junk, W. J., Bayley, P. B., & Sparks, R. E. (1989). The flood pulse concept in river-floodplain systems. *Canadian Special Publication of Fisheries and Aquatic Sciences*, *106*(1), 110–127.

Lane, E. W. (1955). Design of stable channels. *Transactions of the American Society of Civil Engineers*, *120*(1), 1234–1260.

Langbein, W. B., & Leopold, L. B. (1964). Quasi-equilibrium states in channel morphology. *American Journal of Science*, *262*(6), 782–794.

Nepf, H. M. (2012). Hydrodynamics of vegetated channels. *Journal of Hydraulic Research*, *50*(3), 262–279.

Poff, N. L., Allan, J. D., Bain, M. B., Karr, J. R., Prestegaard, K. L., Richter, B. D., et al. (1997). The Natural Flow Regime. *BioScience*, *47*(11), 769–784. https://doi.org/10.2307/1313099

Schumm, S. A., Harvey, M. D., & Watson, C. C. (1984). *Incised channels: morphology, dynamics, and control*. Water Resources Publications.

Shiono, K., Chan, T. L., Spooner, J., Rameshwaran, P., & Chandler, J. H. (2009a). The effect of floodplain roughness on flow structures, bedforms and sediment transport rates in meandering channels with overbank flows: Part I. *Journal of Hydraulic Research*, *47*(1), 5–19. https://doi.org/10.3826/jhr.2009.2944-I

Shiono, K., Chan, T. L., Spooner, J., Rameshwaran, P., & Chandler, J. H. (2009b). The effect of floodplain roughness on flow structures, bedforms and sediment transport rates in meandering channels with overbank flows: Part II. *Journal of Hydraulic Research*, *47*(1), 20–28. https://doi.org/10.3826/jhr.2009.2944-II

Sholtes, J. S., & Doyle, M. W. (2011). Effect of Channel Restoration on Flood Wave Attenuation. *Journal of Hydraulic Engineering*, *137*(2), 196–208. https://doi.org/10.1061/(ASCE)HY.1943-7900.0000294

Stone, M. C., Byrne, C. F., & Morrison, R. R. (2017). Evaluating the impacts of hydrologic and geomorphic alterations on floodplain connectivity. *Ecohydrology*, *10*(5), e1833. https://doi.org/10.1002/eco.1833

Thoms, M. C. (2003). Floodplain–river ecosystems: lateral connections and the implications of human interference. *Geomorphology*, *56*(3), 335–349. https://doi.org/10.1016/S0169-555X(03)00160-0

# CHAPTER 2: EXPERIMENTAL OBSERVATIONS OF FLOODPLAIN VEGETATION, BEDFORMS, AND SEDIMENT TRANSPORT INTERACTIONS IN A MEANDERING CHANNEL*

*A version of this chapter has been published in the Journal of Geophysical Research: Earth Surface:

White, D. C., Morrison, R. R., & Nelson, P. A. (2023). Experimental Observations of Floodplain Vegetation, Bedforms, and Sediment Transport Interactions in a Meandering Channel. *Journal of Geophysical Research: Earth Surface*, *128*(9), e2023JF007136. https://doi.org/10.1029/2023JF007136

## 2.1 Introduction

Floodplains are landforms within river corridors that are hydrologically connected to the active channel and hyporheic zone via three-dimensional flow paths (Jud Harvey & Gooseff, 2015; National Research Council, 2002; von Schiller et al., 2017; Strange et al., 1999) where biological, physical, and chemical processes, such as the transient transport of nutrients, sediment, and wood, occur across different spatial and temporal scales (Brooks et al., 2022; Harvey, 2016; Sawyer & Cardenas, 2012; Tonina & Buffington, 2007; Ward & Packman, 2019; Wohl, 2017). These processes sustain ecological functions, improve habitat, and provide regulating, provisioning, and cultural services to nearby communities (Carpenter et al., 2006, 2009). These ecosystem services can improve as river managers address ecosystem degradation through biomic river and floodplain restoration, which accounts for the importance of biological drivers in functional river corridors (Johnson et al., 2020).

As water overflows from the channel to the floodplain, it interacts with hydraulically rough areas of vegetation and other land surface characteristics, resulting in the attenuation of flood waves (Sholtes & Doyle, 2011), deposition of sediment and wood (Lauer & Parker, 2008; Wohl, 2020), and cycling of nutrients (Olde Venterink et al., 2006). Floodplain vegetation can

significantly alter flow velocity, direction, and conveyance (Branß & Aberle, 2022; Serra-Llobet et al., 2022), and the effects of these interactions can be seen in the river channel, where changes in shear stresses can lead to erosion, sediment deposition, and adjustments in bedforms to accommodate altered hydraulic conditions. In this study, I define bedforms as large-scale bed topography which emerge principally as bar-pool features (Montgomery & Buffington, 1997).

Various studies have investigated the effect of varied floodplain vegetation conditions on geomorphic processes in rivers. In particular, studies have shown that vegetation mechanically stabilizes banks, thereby influencing channel planform (Braudrick et al., 2009; Ielpi et al., 2022; Tal & Paola, 2010). For instance, Török & Parker (2022) found that in channels with fine particles ($D_{50} < 2$ mm), increases in floodplain vegetation was positively correlated with channel width, but they found the reverse for coarse-bedded channels. Conversely, Wieting et al. (2022) found that channel width increased as invasive floodplain vegetation was removed in sand-bedded rivers. Bywater-Reyes et al., (2017) measured the geomorphic effect of in-channel and floodplain vegetation and concluded that riparian vegetation and bedform topography may co-evolve at a range of scales. However, to my knowledge, no flume or field studies have investigated the effects of floodplain vegetation on channel processes nor explicitly quantified bedform response as measured by topographic heterogeneity.

Topographic heterogeneity, or the spatially varied distribution of physical landscape features, is a characteristic commonly associated with functional riparian ecosystems and desirable geomorphic processes (Badgley et al., 2017; Williams et al., 2020; Wohl, 2016b, 2016a). Studies have identified correlations between topographic heterogeneity and habitat suitability (Bellmore & Baxter, 2014; Stoffers et al., 2022), increased biodiversity (Morán-Ordóñez et al., 2015), and attenuation of biogeochemical fluxes (Gooseff et al., 2007; Westbrook

et al., 2006). Because of this noted importance of topographic heterogeneity, many tools and metrics have been developed to quantify the distribution of physical elements, organization of patterns, or the variation of shapes of discretely classified patches (Dietrich et al., 2005; Iskin & Wohl, 2023; Nelson et al., 2014; Scott et al., 2022; Scown et al., 2015; Wohl, 2016a). These metrics have been used to inform design goals and measures of river restoration success (Hinshaw et al., 2022; Scott et al., 2022), and the physical processes that drive them have also been investigated. Specifically, within river channels, the interaction of sediment supply, particle size distribution, flow stage, discharge, wood load, live vegetation, and other biological elements produces spatially variable topographic characteristics as bedforms (Box et al., 2019; Christensen et al., 2022; Lightbody et al., 2019; White & Nelson, 2023; Wohl et al., 2022; Yang & Nepf, 2019). Although there are many studies investigating topographic patterns that emerge because of interactions of flow, sediment, and vegetation within the active channel, there are few that consider the hydrodynamic interactions between floodplain vegetation and flood-stage conditions.

To understand the nature of topographic response within the channel, I can consider previous experimental observations of flow structure in meandering compound channels with fixed beds at overbank depth. As in other similar flume studies, I define compound as consisting of two-stage flow, both within the channel and on the floodplain. A vertical shear layer forms at the channel-floodplain interface and a horizontal shear layer develops across the channel at floodplain height resulting in energy loss and producing secondary circular currents (Ervine et al., 1993; Sellin et al., 1993; Shiono & Muto, 1998). The strength of the resulting secondary current and momentum transfer is highly depth dependent (Knight & Demetriou, 1983; Modalavalasa et al., 2023; Myers, 1978; Sellin et al., 1993; Shiono & Muto, 1998). These

observations frame the need to investigate the following research question: what is the impact of floodplain vegetation density on sediment flux and bed morphology within the channel as a result of the altered flow field?

Few experiments consider both floodplain vegetation characteristics and channel morphology together. Wormleaton et al. (2005) performed a series of meandering, compound, mobile bed, flume experiments at the UK Flood Channel Facility (FCF) with varied configurations of floodplain roughness elements and observed a shift in bed morphology and secondary flow cell location at overbank flow. The FCF flume had a sinuosity ($k$) of 1.35. At Loughborough University, a series of experiments were performed in a meandering ($k = 1.38$), compound, mobile bed similarly comparing the effects of floodplain roughness elements on the flow field and bedforms (Shiono et al., 2009b, 2009a). In these experiments, Shiono et al. observed a decrease in sediment transport from bankfull to low overbank flow depth for both smooth and rough floodplains as well as distinct secondary flow cells in the crossover regions and meander bend apex. The secondary flow cells emerging at higher overbank flow depths and spatial distribution of bed shear stress produced mid-channel bars and ripple-like bedforms atypical of in-bank meandering channel flow. Missing in the meandering compound flume literature are experiments performed in low-sinuosity ($k < 1.3$) channels with bed material other than uniform sand. Because there are very few meandering compound flume experiments described in the literature, I classify those with "high" sinuosity as $k > 1.3$, although I acknowledge that in the geomorphology literature, high-sinuosity channels have been classified as $k > 1.5$ (Leopold & Wolman, 1957).

Previous experimental observations of flow structure in fixed-bed meandering compound channels and the observations made at the FCF and Loughborough University experiments

motivated me to investigate the following research questions: 1) What is the impact of floodplain vegetation density on sediment flux and bed morphology within the channel as a result of the altered flow field? 2) To what extent does the channel sinuosity and floodplain vegetation density influence channel sediment transport capacity? 3) And how do coarser-grained beds respond to increased flow depth and floodplain vegetation density as quantified by topographic complexity?

To investigate the research questions stated, I conducted seven flume experiments systematically varying floodplain vegetation density and flow depth to achieve the following objectives and test associated hypotheses:

Objective 1. Investigate transport capacity response in a sand-to-gravel-bedded channel for a low-sinuosity flume ($k < 1.3$) with varied floodplain vegetation densities and flow depths.

*Hypothesis 1*: In a low-sinuosity flume, transport capacity of sand and gravel will be greater at low relative depth compared to bankfull, unlike observations made in high-sinuosity channels, where sediment transport capacity decreases from bankfull depth to low ($D_r < 0.2$) overbank flow depths. This is due to reduced energy loss at the channel-floodplain interface in lower sinuosity channels.

Objective 2. Quantify bedform topographic response to varied floodplain vegetation density and flow depth using metrics of heterogeneity.

*Hypothesis 2*: For all overbank flow depths, topographic heterogeneity is positively related to floodplain vegetation density.

## 2.2 Methods

### *2.2.1 Experimental setup*

I conducted a series of flume experiments at the Colorado State University Engineering Research Center (ERC), Fort Collins, Colorado, USA. The meandering channel was 1-m wide and inset in a 15.4-m long, 4.9-m wide basin. The flume has a length scale ratio of 1:20, roughly approximating a small-to-medium-sized river. I formed the channel banks and floodplain surface out of twenty-eight 1.2-m wide, 2.4-m long expanded polysterene (EPS) foam blocks and secured them to the concrete floor using steel drop-in anchors, threaded rods, and large bolted washers. The channel centerline follows a sine-generated trace defined by $\phi = \omega \sin\left(\frac{s}{M}\right) 2\pi$, where $\phi$ is the departure angle at location *s* along the curve, $\omega$ is the maximum angle of departure (30°), and $M$ is the meander wavelength (7.85 m). The floodplain adjacent to the channel varies from 1.3 to 2.5 times channel width. General flume configuration parameters are listed in Table 2.1 and a flume layout is shown in Figure 2.1.

**Table 2.1.** Flume Parameters

| | |
|---|---|
| Sinuosity ($k$)/Crossing angle | 1.07/30° |
| Channel top width (m) | 1 |
| Initial channel bed and sediment feed $D_{16}$ (mm) | 1.9 |
| Initial channel bed and sediment feed $D_{50}$ (mm) | 3.3 |
| Initial channel bed and sediment feed $D_{84}$ (mm) | 5.1 |
| Valley slope (m/m) | 0.005 |
| Valley width (m) | 4.87 |
| Valley length (m) | 14.63 |
| Meander wavelength (m) | 7.85 |
| Cylindrical vegetation element diameter (cm) | 2.67 |

To simulate varied floodplain vegetation densities maintaining a 1:20 length scale ratio, I placed 2.67-cm diameter cylindrical elements spaced evenly throughout the floodplain. The cyclinders scale to trees with approximately 0.5-m diameter trunks, close in size to woody riparian vegetation such as middle-aged Cottonwoods (*Populus* spp.) that are common near alluvial rivers in many parts of North America. The emergent vegetation elements were polyvinyl chloride segments attached to the foam floodplain with iron fasteners. The vegetation elements could be quickly and easily attached to and removed from the floodplain foam (see Figure 2.1a). I tested three floodplain vegetation configurations: bare, low-density vegetation (3.0 stems/m$^2$), and high-density vegetation (12.1 stems/m$^2$), the scaled spacing of which approximates observations of similarly-sized trees in Western North America (Friedman & Lee, 2002).

I painted thirty-six ground control points on the floodplain and basin walls that were referenced to a local (*x, y, z*) coordinate system such that $x$ (m) was the downvalley distance in the basin with $x = 0$ at the upstream edge of the floodplain, $y$ (m) is the lateral distance across the basin with $y = 0$ at the basin midpoint, and $z$ (m) is the elevation with $z = 0$ at the underlying flat concrete floor. I used a motor-operated cart mounted on a track running the

length of the flume to position instrumentation for measuring the flow field, water surface elevation, and bed topography at desired *x*, *y*, and *z* coordinates.

A 40HP vertical turbine pump supplied water to a stilling basin upstream of the channel and floodplain. I tested flows ranging from 0.04 $m^3/s$ to 0.18 $m^3/s$ (1.4 cfs to 6.4 cfs), and I adjusted the flow rate to achieve a desired relative depth ($D_r$) over the floodplain surface, such that

$$D_r = \frac{h_{fp}}{h_{fp} + h_c} \tag{1}$$

where $h_{fp}$ is the depth of flow on the floodplain and $h_c$ is the depth of flow in the channel. I set the desired water surface elevation at the beginning of each experiment by opening an upstream butterfly valve and modulating a tailgate downstream of the meander bends. The water surface throughout the flume was parallel to the bed slope and any unsteady effects due to the tailgate were limited to the straight exit section. As water exited the flume, it drained into a sump from where it is was recirculated.

My eperiments include a mobile channel bed consisting of a sand and gravel sediment mixture ($D_{50} = 3.3$ mm) (Figure 2.1). At startup, I filled the channel with sediment and screeded it flat with an initial slope of 0.5 percent and a depth of 8 cm. Masonry blocks were placed upstream of a straight section of channel at the inlet and downstream of a straight outlet section to reduce scour and control flow depth at the up and downtream extents of the flume as sediment was filled to the height of the block. I filled a hopper with a sand and gravel sediment mixture which was fed at a continuous rate into the channel using an auger driven by a variable-speed motor. The rotational speed of the motor was programmed and controlled with an Arduino board. I developed a sediment feed rating curve related to auger rotational speed prior to the

experiments to achieve desired mass trasport rates for each run scenario. As sediment passed beyond the meander bends, it was captured in a tailbox, which I shoveled out to be dried and weighed to determine the bedload transport rate after each flume run.

I designed the channel depth and slope to achieve fully mobile bed material at bankfull flow with an excess dimensionless shear stress ratio, $\left(\frac{\tau_*}{\tau_{*c}}\right)$, of 2.0 for $D_{84}$-sized particles at bankfull depth. Dimensionless shear stress, $\tau_*$, is

$$\tau_* = \frac{\tau}{(G-1)\gamma D} \tag{2}$$

where $G = 2.65$, $\gamma = 9810 \frac{N}{m^3}$, $D = 5.1\ mm$, and reach-averaged shear stress is $\tau = \gamma h S$, where $h = 8\ cm$, $S = 0.005$. I assumed the dimensionless critical shear stress, $\tau_{*c}$, was 0.0386 after Parker (1990). I estimated the initial sediment feed rate for each run based on both the modified Meyer-Peter Mueller (Wong & Parker, 2006) and Wilcock & CroI (2003) sediment transport equations. As the bed evolved during different flow scenarios, I adjusted the feed rate to match bedload transport to facilitate the development of quasi-equilibrium conditions without large-scale slope adjustment. Sediment transport occurred only within the channel during the experiments and did not enter the floodplain.

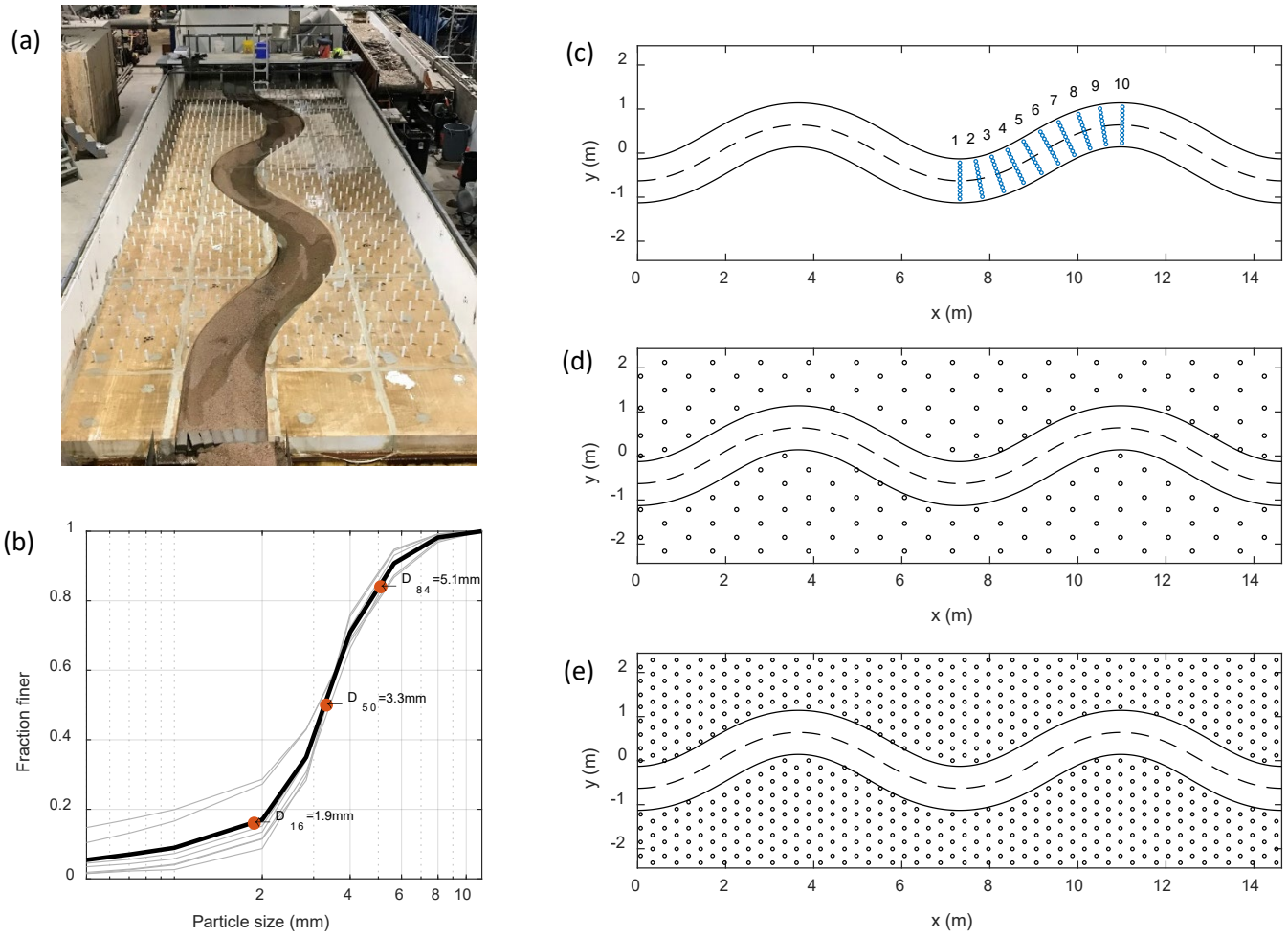


**Figure 2.1.** (a) Experimental flume set up. In this photo, floodplain vegetation was configured in the high density arangement. Flow direction is from top to bottom of photo. (b) Bed material particle size distribution of sediment fed into the channel. The dark line is the average of nine bulk samples (light-grey lines). (c) Laboratory flume channel configuration with bare floodplain. Blue points represent locations at which flow measurements were taken. The dashed line is the channel centerline. Cross station locations are numbered. (d) Floodplain vegetation configuration at low density (3.0 stems/m$^2$). (e) Floodplain vegetation configuration at high density (12.1 stems/m$^2$)

I conducted seven experimental runs to test bedform response to varied floodplain vegetation conditions and flow depths. The resulting quasi-equilbrium bedform conditions at bankfull flow were compared to those which occurred at two relative depths and three floodplain conditions. Descriptions of experimental parameters associated with all seven runs are listed in Table 2.

**Table 2.2**. Flume Run Scenarios

| Run | Discharge | Run Time | Sediment Supply | Floodplain Vegetation | Relative Depth |
|---|---|---|---|---|---|
| 1 | 0.04 $m^3/s$ | 33.7 hr | 5 kg/hr | NA | (bankfull) |
| 2 | 0.08 $m^3/s$ | 46.1 hr | 2.5 kg/hr | 0 | 0.1 |
| 3 | 0.08 $m^3/s$ | 27.3 hr | 2.5 kg/hr | Low - 3.0 cylinders/$m^2$ | 0.1 |
| 4 | 0.08 $m^3/s$ | 16.6 hr | 2.5 kg/hr | High – 12.1 cylinders/$m^2$ | 0.1 |
| 5 | 0.18 $m^3/s$ | 26.8 hr | 80 kg/hr | High – 12.1 cylinders/$m^2$ | 0.25 |
| 6 | 0.17 $m^3/s$ | 16.4 hr | 65 kg/hr | Low - 3.0 cylinders/$m^2$ | 0.25 |
| 7 | 0.16 $m^3/s$ | 11.6 hr | 60 kg/hr | 0 | 0.25 |

At the start of each flume run I slowly filled the channel with water to avoid altering bed conditions that developed during the previous run. Once the channel was near bankfull depth and flow overtopped the downstream tailgate, I opened the upstream butterfly valve to achieve the desired relative depth and began feeding sediment into the channel.

*2.2.2 Data collection*

I carried out each of the seven run scenarios described in Table 2.2 over multiple flume operation periods lasting from approximately 4 to 8 hours, measuring bed topography after each one to identify quasi-equilibrium conditions when the bed was neither agrading or degrading. Between flume operation periods, I slowly drained the channel to preserve bed topography, and dried and weighed the sediment captured in the tailbox. I surveyed bed topography between flume runs using structure-from-motion (SfM) photogrammetry, a widely used tool to measure geomorphic change (Leduc et al., 2019; Morgan et al., 2017; Westoby et al., 2012). Following each flume run, when water had completely drained from the channel, I took approximately 300 nadir photos pointed perpendicular to the local x-y plane using a 20 megapixel camera with a fixed zoom at a height of 2.5-m above of the floodplain surface. Each photo had approximately 80% front and side overlap. I imported the images into Agisoft Metashape ("Agisoft Metashape

Professional," 2022) for point cloud processing following the workflow recommendations by Over et al. (2021). I aligned the photos in Metashape with 'high' accuracy setting and optimized tie-points. I reduced error in the sparse clouds by removing points with high reconstruction uncertainty, projection accuracy, and reprojection error. Once tie points were optimized, I referenced the model to ground control points (GCPs) that I had surveyed into the local coordinate system using a Leica total station. I then generated a dense point cloud. I verified the accuracy of each point cloud by comparison with each known GCP. Average horizontal and vertical accuracy between point clouds and GCPs was better than 5 mm for all models.

I then converted the bed topography point clouds to a DEM using Kriging interpolation in Golden Software's Surfer program ("Surfer," 2022) with a defined 0.005-m grid to facilitate analysis and comparison between each surveyed bedform surface although the point spacing was at much higher resolution.

*2.2.3 Topography processing*

I processed the gridded SfM models by computing a downvalley detrended DEM by computing the average elevation at transects oriented perpendicular to the downvalley (y-axis) direction and differencing the original bed elevation values from the average transect value. Detrending the DEM eliminates the valley gradient and produces raster imagery with more easily recognizable local bedform features.

To measure and visualize changes in bedforms through deposition or erosion, I performed a differencing of DEMs comparing topography for each of the six overbank flow scenarios with the bankfull flow scenario.

*2.2.4 Geomorphic complexity metrics*

Systematic quantificaton of spatial geomorphic heterogeneity and complexity has been tested using various approaches (Scown et al., 2015; Wohl, 2016b). Geomorphic features are often clustered into patches, which have also been systematically classified by spatially distributed characteristics (Nelson et al., 2014; Scott et al., 2022). I tested multiple approaches for comparing reach-averaged and grid-cell metrics of heterogeneity. I performed a 2D (x, y) sliding neighborhood operation to compute statistical metrics of grid cells with windows ranging in size from 5-cm to 50-cm, larger than the resolution of the data, but small enough to capture visually observed bedform units. When regions outside the channel were included in the window, they were ignored. I computed the following statistical metrics:

Moving window mean, $\mu_w$, was calculated as

$$\mu_w = \frac{\sum_{i=1}^{n} z_i}{n} \tag{3}$$

where $z_i$ is the elevation of the $i$th cell, and $n$ is the number of cells within the boundaries of the moving window. The mean elevation describes general bedform topography throughout the reach.

Standard deviation, $\sigma_w$, which describes the variability of cell elevation about the mean, was calculated as

$$\sigma_w = \sqrt{\frac{\sum_{i=1}^{n}(z_i - \mu_w)^2}{n}}. \tag{4}$$

Topographic coefficient of variation, $CV_w$, which describes the variability of standard deviation compared to the mean, was calculated as

$$CV_w = \frac{\sigma_w}{\mu_w}. \quad (5)$$

High $CV_w$ values may be indicative of topographic low points with some variability in surrounding topographic relief.

Topographic skewness, $\tilde{\mu}_3$, which is used to quantify the presence of local high and low points that fall near the tails of the distribution of cell elevations within a moving window (Scown et al., 2015), was calculated as

$$\tilde{\mu}_3 = \sum_{i=1}^{n} \frac{(z_i - \mu_w)^3}{(n-1) \times {\sigma_w}^3}. \quad (6)$$

The bed developed spatially coherent, patch-like features prompting statistical analysis of patch characteristics to quantify spatial complexity, where complexity is indicated by a greater number of patches of a range of patch sizes. I classified five patch types for the detrended topography grids by dividing the 0.3-m elevation range (0 m to 0.3 m) evenly into five bins. I assigned each cell a classificatione from 1 to 5 with 1 being the lowest elevation range bin, (0 m to 0.06 m) and 5 being the highest elevaton range bin (0.24 m to 0.30 m). Generally, all cells within the pools were of patch type 1, and cells located on bar tops were of the patch type, 5. Metrics used to quanitify the overall patch characteristics following the approach described by Nelson et al. (2014) include:

Mean patch area, $\overline{A_p}$

$$\overline{A_p} = \frac{1}{n_p} \sum_{i=1}^{n_p} A_{ip} \quad (7)$$

where $n_p$ is the total number of observed patches, and $A_{ip}$ is the area of each contiguous patch. A low mean patch area suggests there are many smaller patches, and a large mean patch area suggest the presence of few large patches.

Standard deviation of patch areas, $\sigma_p$

$$\sigma_p = \sqrt{\frac{\sum_{i=1}^{n}(A_{ip} - \bar{A}_p)^2}{n}} \tag{8}$$

where $\bar{A}_p$ is the average patch area of the entire channel. Standard deviation of patch area describes the variability of patch sizes around the mean patch area and may suggest a higher frequency of patches with dissimilar patch sizes.

Patch coefficient of variation, $CV_p$

$$CV_p = \frac{\sigma_p}{\bar{A}_p} \tag{9}$$

which describes the variability in patch sizes in relation to the mean patch area.

Contagion, $C$

$$C = 1 + \sum_{i=1}^{k}\sum_{j=1}^{k}\frac{P_{ij}\ln(P_{ij})}{2\ln k} \tag{10}$$

where $P_{ij}$ is the probability a pixel of patch type $i$ has an adjacent pixel of patch type $j$, and $k$ is the number of patch type classifications. Contagion is a landscape index used to describe patch diversity and clumping (Li & Reynolds, 1993; Riitters et al., 1996). A high contagion value suggests that there are few large contiguous patches and a low contagion value suggests there are many variably distributed small patches.

## 2.3. Results

### *2.3.1 Sediment transport*

At bankfull flow, the channel reached quasi-equilibrium after about 30 hours of run time with sediment transport at the flume outlet stabilizing at around 2 kg/h (see Figure 2.3). As flows transitioned from bankfull to $D_r$ = 0.1 with no floodplain vegetation, sediment transport increased to approximately 25 kg/h. Following this sharp increase, it dropped to a quasi-equilbrium transport rate of approximately 5 kg/h (See Figure 2.3). After adding low-density floodplain vegetation at t = 80 h, the sediment transport rate increased to approximately 7 kg/h, and 15 kg/h after adding high-density floodplain vegetation at t = 107 h. I then increased flow depth to $D_r = 0.25$ with high floodplain vegetation density, and sediment transport increased sharply to 104 kg/h and relaxed to 70 kg/h as the bed adjusted. As floodplain vegetation was removed to simulate low-density conditions, transport rate dropped to 60 kg/h, and for a bare floodplain the transport rate fell further to 40 kg/h. In general, highest sediment transport was observed for the $D_r$ = 0.25 runs, and increased with vegetation density for both $D_r$ = 0.1, and $D_r$ = 0.25.

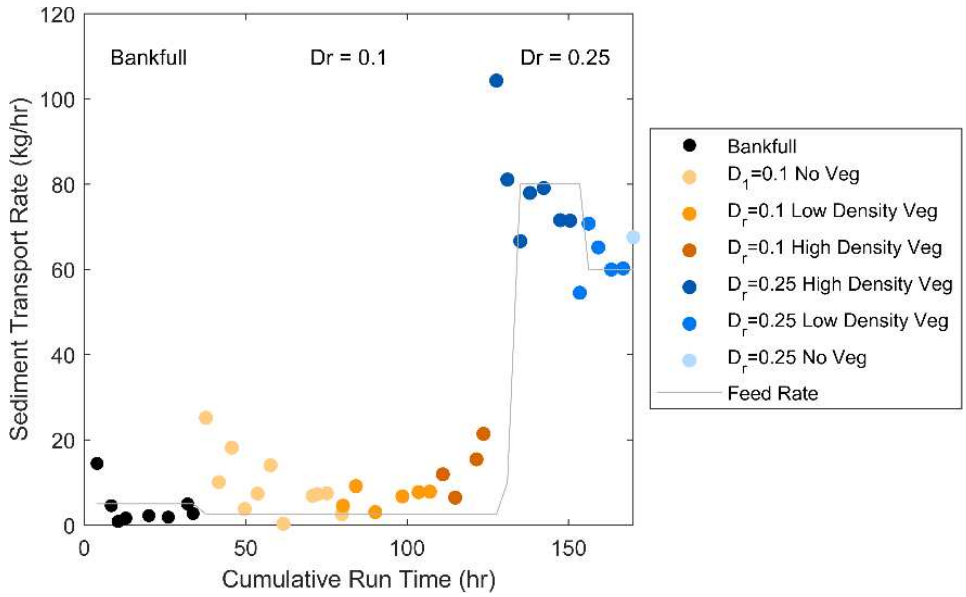


**Figure 2.2.** Measured sediment transport rate during all seven experimental runs. The colored points represent total sediment transport rate as measured by dry sediment accumulated in the tailbox over the duration of the flume run.

Sediment transport rate increased nonlinearly with depth for all floodplain vegetation conditions. I show this in Figure 2.3 where normalized sediment transport rate, or the ratio of total bedload transport for each flume run, $Q_b$, to total bankfull bedload transport $Q_{bbf}$, is plotted vs. relative depth (compare with Shiono et al., (2009b), Figure 2.6). Normalized sediment transport rate at $D_r$ = 0.1 and $D_r$ = 0.25 was highest for the densely vegetated floodplain and lowest for the non-vegetated floodplain.

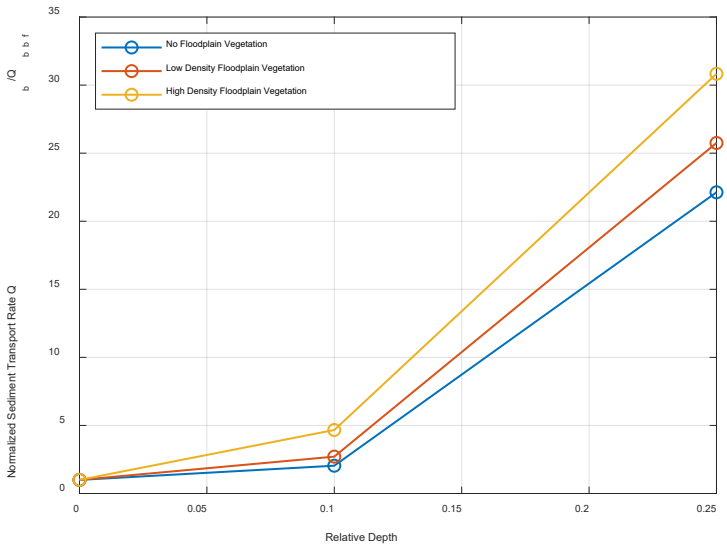


**Figure 2.3.** Normalized sediment transport rate vs. relative depth for each floodplain vegetation condition.

*2.3.2 Quasi-equilibrium bedform topography*

Quasi-equilbrium bedform topography for each of the seven run scenarios is presented in Figure 2.4. During the startup period, as the screeded flat channel developed bedforms, and in transition from one run to the next, the bed adjusted to new hydraulic conditions. This adjustment was reflected in fluctuations of the channel slope and shift in bedload transport. However, during each run, the slope eventually returned to quasi-equilbrium, after which I collected measurements. Classic bar-pool bedforms were observed throughout the experiment, although overbank flows produced more pronounced bedforms with greater relief than the bankfull condition. At bankfull flow, the bar lobe extends farther laterally into the channel than all overbank flow scenarios. Longitudinal bedform features developed downstream of the bar for $D_r = 0.1$, and $D_r = 0.25$, and were more pronounced for the scenarios with floodplain vegetation scenarios compared to the scenario with no vegetation.

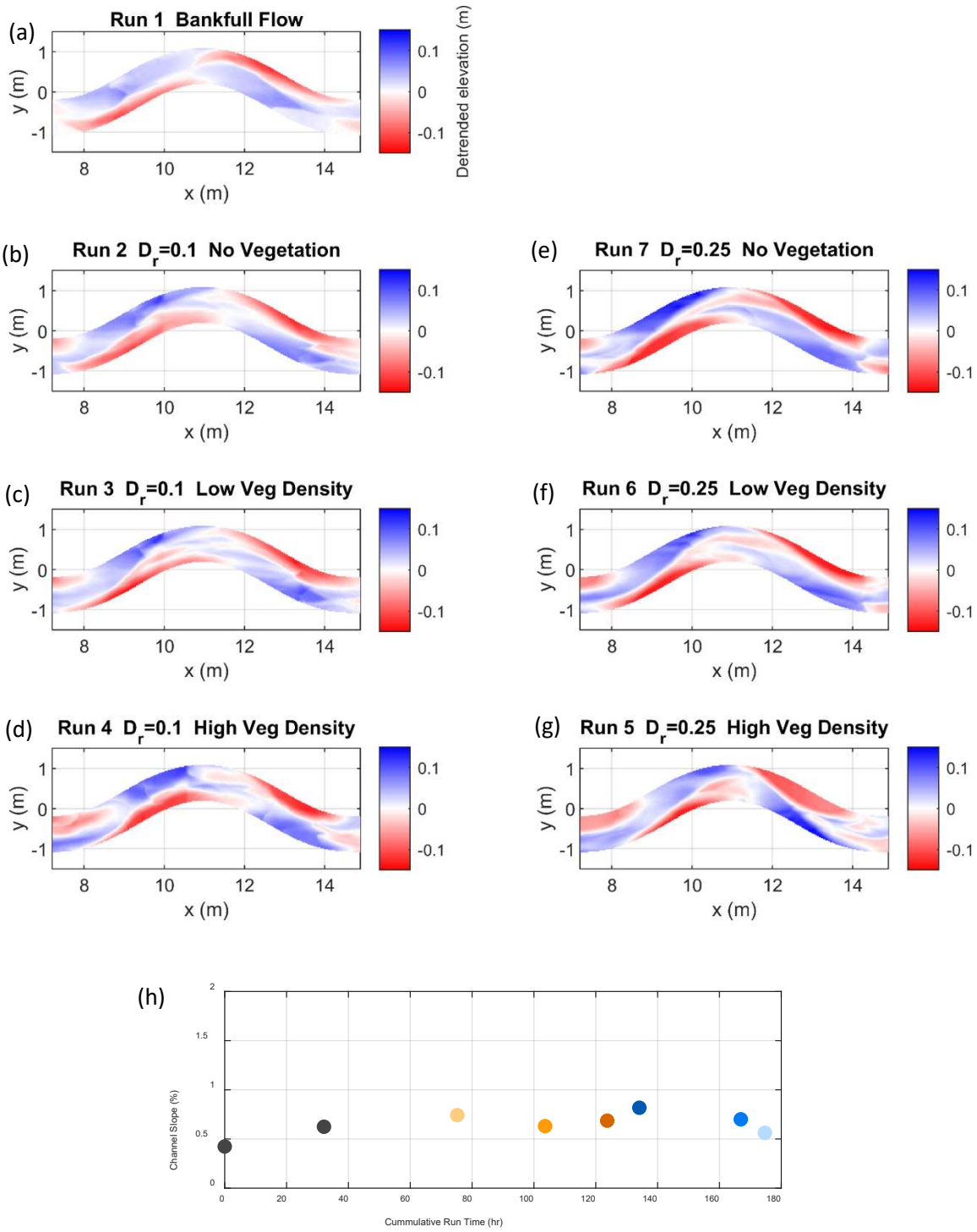


**Figure 2.4**. Downvalley detrended bed elevation at quasi-equilbrium conditions for each of the seven run scenarios. (h) Channel slope during each of the seven runs at quasi-equilbrium. Slope was determined by fitting a linear curve to the longitudinal profile for all runs.

Cross-section plots for each flume run are depicted in Figure 2.5. The bankfull profiles have much less topographic variation than overbank flow profiles in all 10 cross-sections, with shallower pools and lower bars. The longitudinal bedform features mentioned above can be seen as peaks and troughs in the cross-section plots for XS6 through XS10. The scenario with $D_r = 0.25$ and high-density vegetation produced the largest peak and trough features with relief as great as 0.7 cm, as seen in Figure 2.5j, XS9 (dark blue line). These peak and trough features were present in the cross-over region of the channel near the bend apex.

Bars and pools remained somewhat stable during experiments, persisting through all seven runs. As I raised flows from bankfull depth to $D_r = 0.1$, I observed that the pools generally became deeper and deposition of fine particles caused the bars to aggrade, but within the first ten hours of run time at overbank flow, the channel stabilized, and no significant net aggradation or net scour occurred. To measure changes in bar-pool morphology through the experiments I computed the difference in elevation of the bed 1 cm from the right and left banks (see Figure 2.6) and identified bedform tops as the local maxima and minima as done by others in studies of bed morphology (Martin & Jerolmack, 2013; Nelson & Morgan, 2018). I then computed wavelength (the distance between the local maxima and minima of right- and left-bank-differenced elevations), and amplitude (the height difference between local maxima or minima and proximal zero-crossing point elevation).

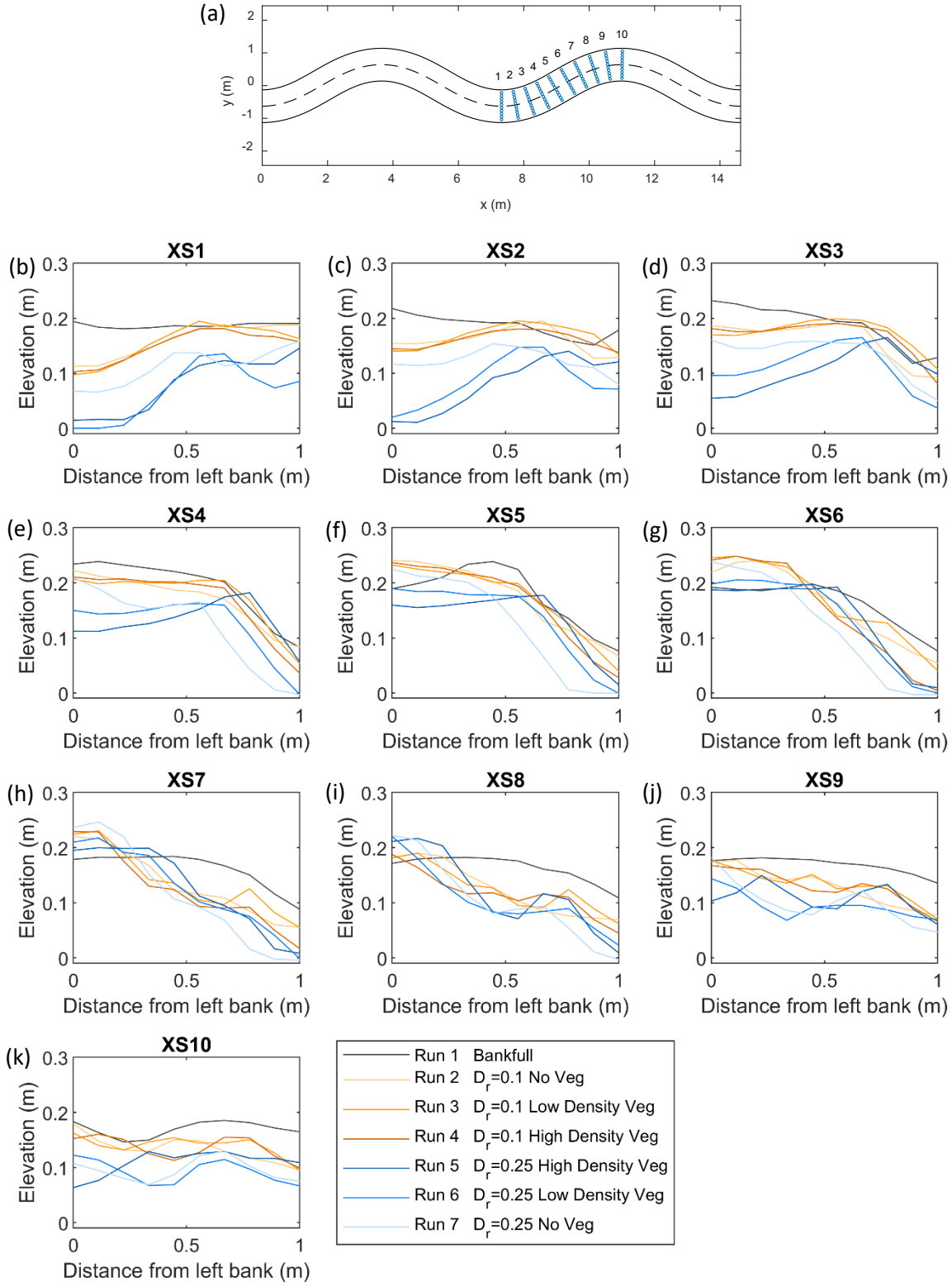


**Figure 2.5**. (a) Flume planform schematic with cross-section locations. (b-k) Ten cross-section plots of quasi-equilibrium topography for all seven runs.

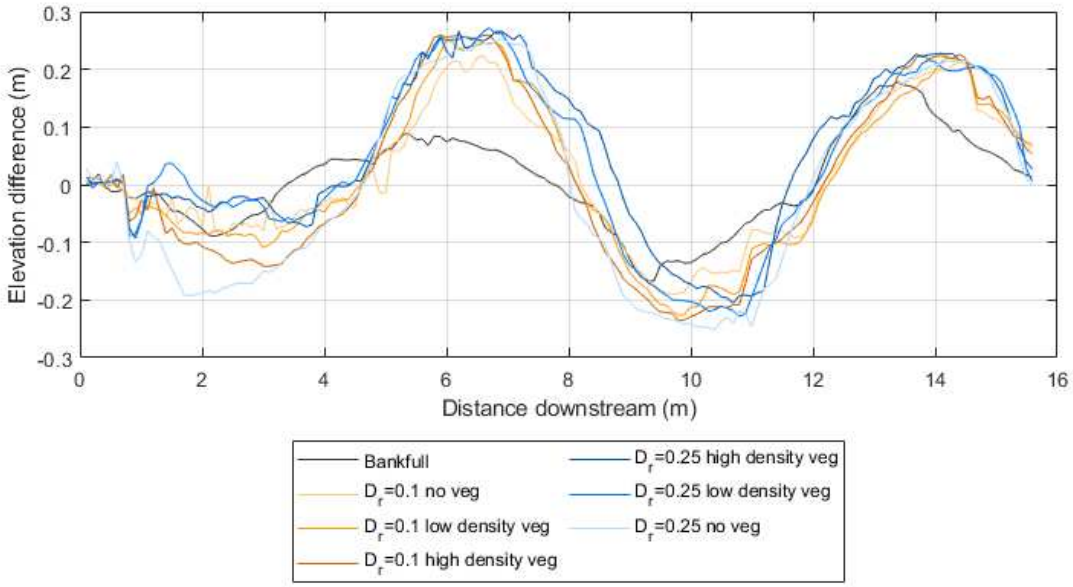


**Figure 2.6**. Elevation profile of bed height difference near left and right banks at quasi-equilibrium.

Slight adjustments of wavelength and amplitude occurred during all runs at overbank flows (See Figure 2.6 and Table 2.3) but were less than the adjustments observed during the transition from bankfull to $D_r = 0.1$. In the experimental transition from $D_r = 0.1$ to $D_r = 0.25$ at high vegetation density, the head of the pool began to migrate upstream and at times scoured down through the bed material to the concrete floor, though the pool was subsequently filled in with sediment. From approximately 140 to 150 hours of run time, the bed went through an adjustment phase as the head of the pools shifted upstream then back downstream. This adjustment in bar-pool wavelength may be a response to the flow conditions developed as the bed material was scoured out.

In the region of developed flow in the bend (y = 7 m to y = 15 m), the bar apex shifted 1 m downstream and the amplitude increased from 0.18 m to 0.21 m as flows increased from bankfull to overbank (See Figure 2.6). For the $D_r = 0.1$ scenarios, wavelength remained relatively constant at approximately 4 m for all floodplain vegetation conditions. Wavelength

was lower for high relative depth ($D_r = 0.25$) at aproximately 3.7 m. Bar amplitude at bankfull flow was 0.18 m and shifted to higher values for $D_r$= 0.1 runs. During $D_r$ = 0.1 runs, bar amplitude increased with floodplain vegetation density from 0.21 m to 0.25 m. During all $D_r$ = 0.25 runs, amplitude remained near 0.25 m. The bar wavelength and amplitude were likely constrained in the pool by the flume's concrete floor at z = 0. For a summary of results related to bar morphology, see Table 2.3.

**Table 2.3.** Summary of topographic heterogeneity metrics. For a definition of each metric, see Section 2.4.

| Run | $Q_b$ (kg/hr) | $D_r$ | Vegetation Density (units/m$^2$) | Bar Characteristics | | Reach-averaged Moving Window Statistics | | | Patch Statistics | | | |
|---|---|---|---|---|---|---|---|---|---|---|---|---|
| | | | | Bar Wavelength (m) | Bar Amplitude (m) | $\sigma_w$ | $CV_w$ | $\tilde{\mu}_3$ | $\overline{A_p}$ (m$^2$) | $\sigma_p$ (m$^2$) | $CV_p$ (m$^2$) | $C$ |
| 1 | 2 | 0 | NA | 4.25 | 0.18 | 0.0047 | 0.035 | -0.072 | 0.56 | 0.95 | 1.7 | 0.67 |
| 2 | 5 | 0.1 | 0 | 3.95 | 0.21 | 0.0056 | 0.049 | -0.017 | 0.49 | 0.83 | 1.71 | 0.656 |
| 3 | 7 | 0.1 | 3 | 4.13 | 0.24 | 0.0066 | 0.066 | -0.047 | 0.46 | 0.86 | 1.88 | 0.649 |
| 4 | 15 | 0.1 | 12 | 4.03 | 0.25 | 0.0072 | 0.153 | 0.042 | 0.38 | 0.73 | 1.89 | 0.631 |
| 5 | 70 | 0.25 | 12 | 3.6 | 0.24 | 0.0079 | 0.138 | 0.07 | 0.46 | 0.77 | 1.69 | 0.621 |
| 6 | 60 | 0.25 | 3 | 3.57 | 0.25 | 0.0076 | 0.111 | 0.03 | 0.52 | 0.85 | 1.62 | 0.642 |
| 7 | 40 | 0.25 | 0 | 3.95 | 0.25 | 0.0073 | 0.153 | 0.096 | 0.61 | 0.78 | 1.28 | 0.64 |

*2.3.3 Metrics of topographic heterogeneity*

I used both a qualitative and quantitative approach to classify geomorphic complexity associated with each of the flume run scenarios. As described in Section 2.4, a sliding window analysis was performed to compute topographic heterogeneity metrics including mean, standard deviation, coefficient of variation, and skewness. To account for the influence of scale in statistical analysis of a topographic surfaces, which was discussed by Scown et al. (2015), I tested various moving window sizes including 5 cm, 10 cm, 20 cm, and 50 cm. The window size should be greater than the dataset grid size and similar in size to the bedform features. I focus my analysis on the 10-cm moving window size because it captures the topographic fluctuations of bedform features at that scale which were easily visualized in the spatially mapped metrics.

Spatially mapped coefficients of variation were high in pools where the mean elevation was low and the adjacent cells on the lateral slope had variable elevation. This suggests that high coefficient of variation can be associated with topographic depressions (See Figure 2.7a). Spatially mapped distributions of the standard deviation of cells within a 10-cm moving window highlight regions of the bed that had both high and low variability about the mean cell elevation. Regions of the bed that exhibited high standard deviation values were most commonly associated with high local slope, such as at the laterally sloping region between the bar and pool, and near the bar tail (See Figure 2.7b). Spatially mapped skewness performed well to visually highlight topographic high and low points (See Figure 2.7c), which fall near the tails of the distribution of cell elevations within the moving window. Topographic heterogeneity is likely captured by regions of high standard deviation, high coefficient of variation, and both high and low skewness.

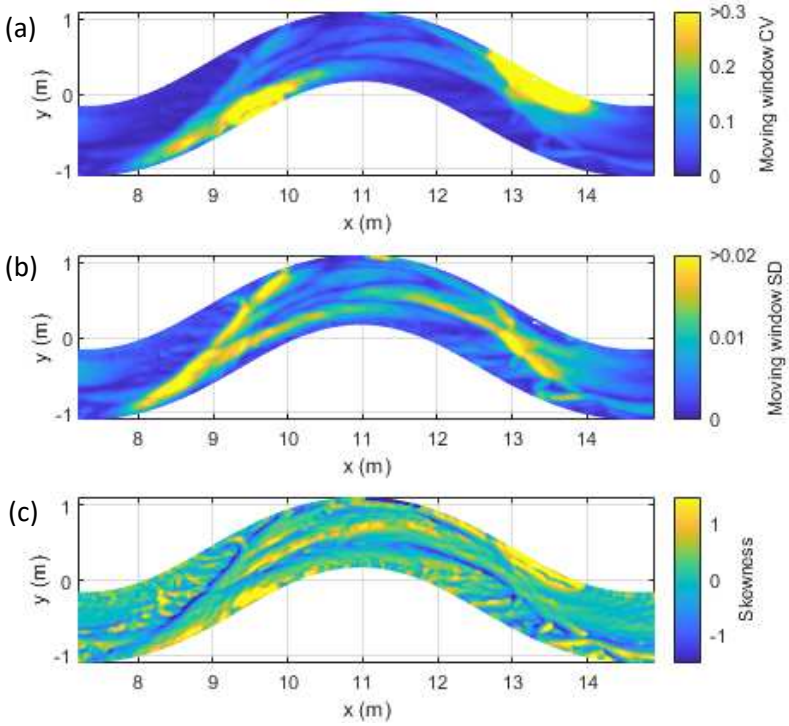


**Figure 2.7**. Spatially mapped surface metrics of the high vegetation density, $D_r$ = 0.1 scenario: (a) Coefficient of variation, (b) standard deviation, (c) skewness computed with a 10-cm moving window.

A summary of topographic heterogeneity metrics for the entire channel, including coefficient of variation, standard deviation, and skewness, are shown in Figure 2.8 and Table 2.3. The bedform topography at bankfull flow had low median coefficient of variation and standard deviation and a narrow distribution of both values. At $D_r$ = 0.1, median coefficient of variation and standard deviation increased with vegetation density, indicating an increase in topographic heterogeneity. The distribution of both coefficient of variation and standard deviation also became wider with increased floodplain vegetation density. During the $D_r$ = 0.25 runs, median coefficient of variation was highest with high floodplain vegetation density and also had the widest distribution of coefficient of variation values. Median standard deviation decreased slightly with floodplain vegetation density, but the high vegetation density run had the widest distribution of standard deviation values.

Although locally heterogenous patches of bedform topography as measured by skewness were visually observable, reach-wide median skewness values were relatively consistent for all flow depth and floodplain vegetation conditions. However, for both $D_r$ = 0.1 and $D_r$ = 0.25, the high vegetation density conditions produced the widest distribution of skewness values with higher and lower skewness values reported. The relatively unchanging median skewness may not necessarily reflect the lack of change in topographic heterogeneity, because the presence of patches of both low and high skewness values may balance one another over the entire reach, and thus a wider distribution of skewness values may be a better indicator of topographic heterogeneity.

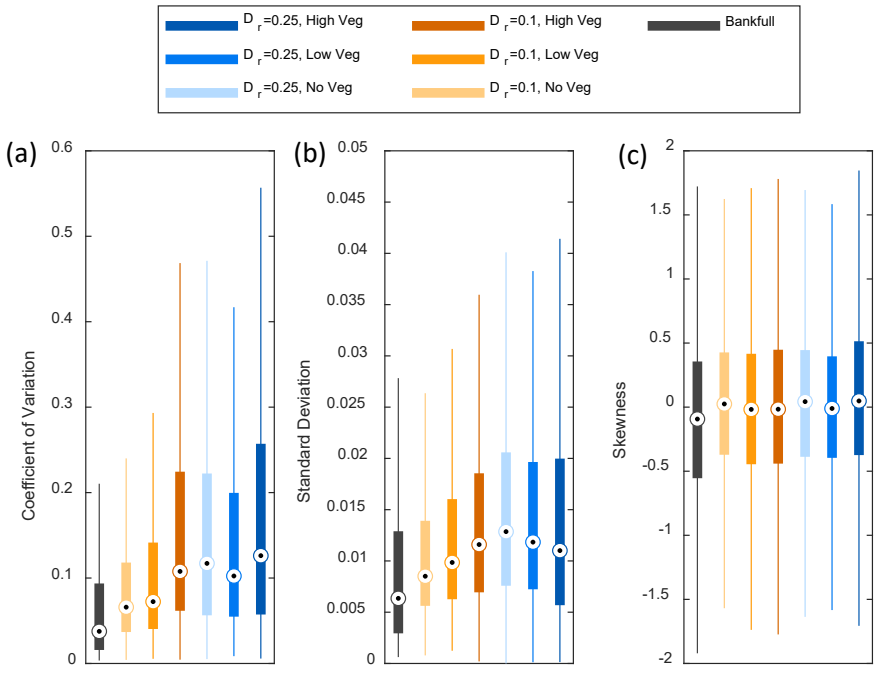


**Figure 2.8**. Moving window analysis of topographc heterogeneity metrics (a) coefficient of variation, (b) standard deviation, and (c) skewness for all runs computed with a 10-cm moving window. Outliers are not displayed

The topographic features that I observed associated with higher flow and vegetation density appeared patchy with localized regions of high and low elevation. To quantify the patchiness associated with the different flow depths and floodplain vegetation conditions, five elevation classes were established with equal height spacing ranging from the lowest to highest point in each detrended DEM. An example of these spatially classified patches is shown in Figure 2.9, and a summary of patch analysis results is presented in Figure 2.10 and Table 2.3. Also refer back to the detrended DEMs for all seven runs in Figure 2.4 where the patchy nature of the bed topography is visible.

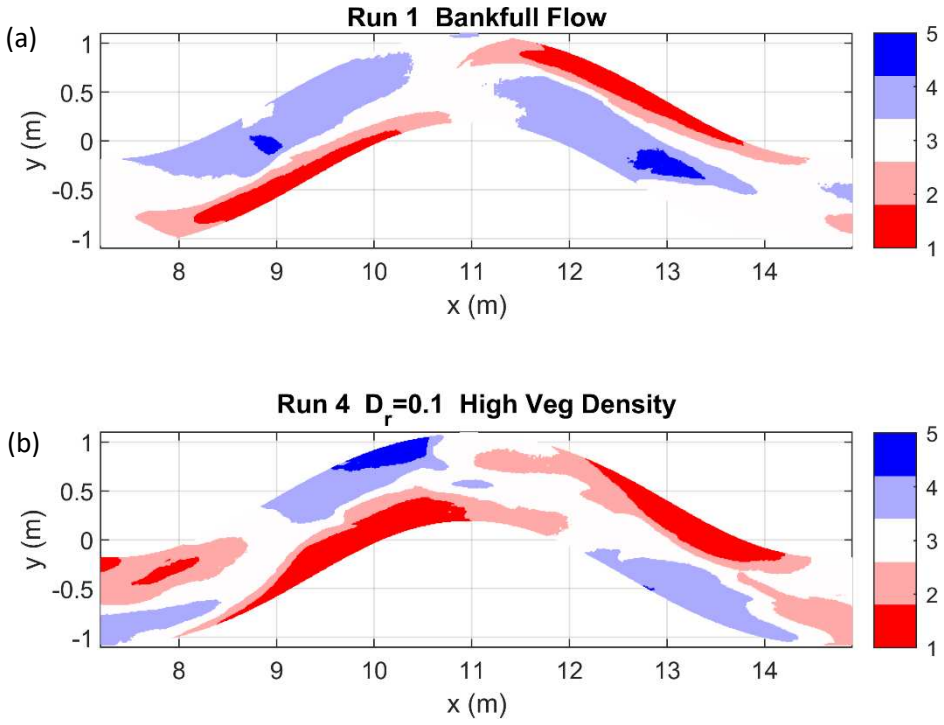


**Figure 2.9**. Visulization of patch classifications for (a) Run 1 and (b) Run 4. The grid cells are assigned to one of five equally sized elevation classes.

Contagion, a landscape patchiness index, was used to describe topographic patch diversity. I observed clear trends in contagion resulting from increased depth and floodplain vegetation density. A high contagion value suggests that there are few large patches, and a low cotagion value suggests there are many small patches. The computed contagion index (Figure 10a) for each quasi-equilbrium bed is generally in agreement with patch statistics shown in Figure 2.10b. In Figure 2.10a, the lowest contagion index corresponds to the high density floodplain vegetation scenario at $D_r$ = 0.25, suggesting that high flow depth and vegetation density produced highly heterogeneous bedform topography. Contagion had a negative relationship with depth for all three floodplain cover scenarios suggesting that deeper flow may produce more topographically heterogeneous bedforms. At both $D_r$ = 0.1 and $D_r$ = 0.25, high density floodplain vegetation produced low contagion values.

In addition to contagion, patch statistics describing topographic heterogeneity, including mean area, standard deviation, and coefficient of variation were computed and are presented in Figure 2.10 (b) and Table 2.3. The number of patches was highest (n = 19) for Run 4 ($D_r$ = 0.1, high vegetation density). The lowest mean patch area was also measured during Run 4, suggesting that many small patches were observed. At $D_r$ = 0.1, mean patch area decreased as more floodplain vegetation was added, and at $D_r$ = 0.25, mean patch area increased as vegetation was removed. The $D_r$ = 0.1 runs generally had more patches than the $D_r$ = 0.25 runs; however, there were more small-to-medium patches (approximately 0.25 $m^2$), which are approximately the size of the bedform features that were observable during the flume runs and in the detrended DEMs.

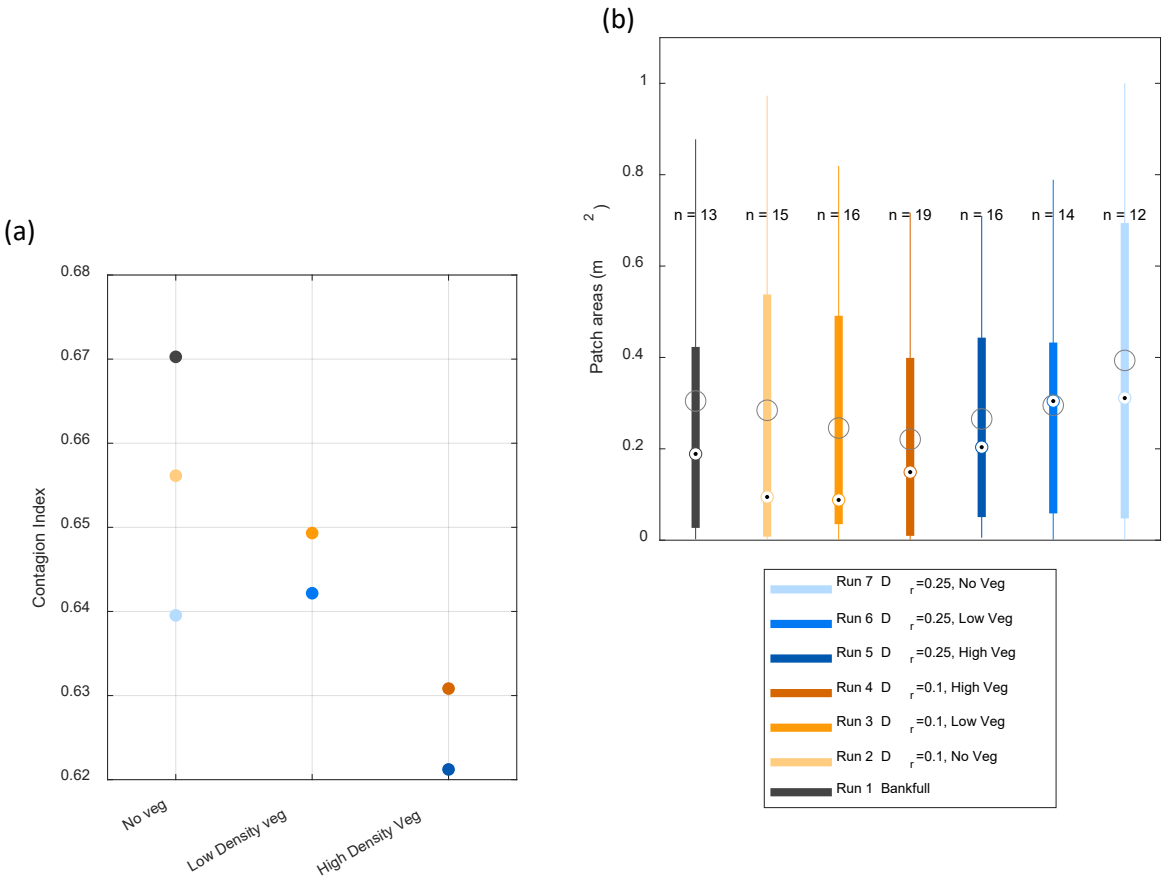


**Figure 2.10**. (a) Contagion Index. (b) Topographic patch statistics. Each box plot represents the distribution of patch area. The black dot represent the median patch area. The larger light-grey circles represent the mean patch area. Legend in (b) corresponds to both (a) and (b).

## 2.4. Discussion

### *2.4.1 Relative depth vs. vegetation density*

Although in this study I do not analyze the flow field in detail, results from studies such as Shiono et al. (2009a, 2009b) indicate that the addition of emergent floodplain roughness elements enhances the shear layer at the channel-floodplain interface due to slowed floodplain flows' interaction with main channel flows. I observed that the presence of vegetation slows floodplain flow velocity and steers flow toward the channel, thus increasing in-channel conveyance and enhancing 3D helical flow structures. This produced greater spatial variability

and ranges of bed shear stress corresponding to the presence of strengthened secondary currents. Regardless of the channel planform, it is likely that secondary flow features are enhanced in the cross-over region of the channel due to the difference in main channel velocity and slowed floodplain velocity re-entering the channel. The cross-over region is where I observed patchy bedform features (e.g., Figure 2.4). The enhanced secondary flow was likely also responsible for the increased bar-pool relief and increase in amplitude as shown in Figure 2.6a. Here it appears that the increased flow depth from bankfull to both $D_r = 0.1$ and $D_r = 0.25$ had a greater relative influence on half-meander-scale bar pool features than floodplain vegetation density.

I hypothesized that for all overbank flow depths, topographic heterogeneity increases with floodplain vegetation density (see Section 1, Hypothesis 2). For both the moving window and patch analysis, statistical metrics indicate that even at low flood stage ($D_r = 0.1$), topographic heterogeneity was greater than under bankfull conditions (e.g., Figure 2.10). At $D_r = 0.1$, high floodplain vegetation density produced metrics that indicated bedform heterogeneity was as high as those observed for all floodplain vegetation densities at $D_r = 0.25$. Reach-wide topographic standard deviation and coefficient of variation distributions indicated that at $D_r = 0.1$, increasing floodplain vegetation density created measurable increases to bedform complexity, but at $D_r = 0.25$, although increasing floodplain vegetation density increased bedform complexity, the change was not as dramatic. Similar patterns emerged using the patch-based analysis. I interpret this to suggest that there may be thresholds in bedform heterogeneity and that increasing depth any higher may not necessarily produce more complex bedforms. This threshold may arise due to a shift in shear stress distribution and a channel's tendency toward minimum energy expenditure and least action (e.g., Nanson & Huang, 2008, 2017).

The results of this study suggest that the increased turbulent energy resulting from channel-floodplain flow interaction and main channel conveyance is accommodated through the development of flow-resisting, energy-consuming roughness in the form of superimposed complex topography. Meandering channels commonly achieve equilibrium bankfull hydraulic conditions through the complex interaction of planform-induced 3D flow field and energy expenditure through form and surface hydraulic roughness (Buffington & Montgomery, 1999; Dietrich & Whiting, 1989; Lane, 1955; Powell, 2014; Sear, 1996). During floods, meandering planform geometry continues to drive reach-scale bar-pool morphology, however, with an altered flow field and turbulence characteristics (Wormleaton et al., 2004). Knight & Shiono (1990) showed that as flows exceed bankfull, turbulent flow structures at the channel-floodplain interface increase eddy viscosity and depth-averaged Reynolds stresses particularly at low relative depths. Highly complex bedforms with local patches of high relief are inherently more hydraulically rough (Buffington & Montgomery, 1999; Hassan & Reid, 1990). An increase in hydraulic roughness limits excessive erosion energy, maintaining channel equilibrium (Davies & Sutherland, 1980; Nanson & Huang, 2008; Wohl & Merritt, 2008) accounting for a channel's tendency toward an equilibrium state (Davies & Sutherland, 1983; Eaton et al., 2004). Flows likely approach a threshold when bedforms no longer become more complex with stage, and energy dissipation required to maintain channel stability may shift to the upper portion of the water column and in the floodplain, which is supported by the observations made by Knight & Shiono (1990) in which the highest Reynolds stresses occur in the upper portion of the water column at the channel-floodplain interface. In terms of total available reach-scale boundary shear stress at high flow depths, energy is likely dissipated through boundary shear in the floodplain.

In my experiments, general bar-pool morphology appeared to be primarily controlled by planform; however, amplitude and wavelength were apparently influenced by vegetation density and flow depth in ways comparable to other experiments in the literature. In a series of flume experiments, Calvani et al. (2023) observed an increase in bar amplitude with the addition of rigid emergent vegetation elements located within the channel. They also observed long depositional features associated with the emergent vegetation patches. Other flume experiments that did not include floodplain flows or vegetation have shown that at high flow rates, alternate bar morphology shifts to a plane bad and hydraulic roughness decreases (Ikeda, 1984; Palucis et al., 2018). The meandering planform in my experiments fixed the bar-pool morphology limiting bar wavelength, although I did see a slight shift as flow depth increased from $D_r = 0.1$ to $D_r = 0.25$ (See Figure 2.6). Similar to meandering channel flume experiments performed by (Termini, 2009), at all flow depths in my experiments, bar-pool unit morphology and associated wavelength were constrained by a scour zone that follows a line tangential to the crossing angle. This suggests that even in compound channels with vegetated floodplains, meandering planform controls bar morphology and bar wavelength approximately matches planform meander wavelength. Bar-pool morphology likely would show a different response had the banks been highly erodible, and the channel width may have been influenced by the presence and density of floodplain vegetation. For example, Wieting et al. (2023) found that channel width increased significantly with the removal of floodplain vegetation.

Although I did not investigate grain mobility as a function of the gravitational forces on reach- and patch-scale bedforms, topographic heterogeneity as measured by statistical metrics may also be limited by angle of repose, local slope, and grain-scale roughness. Thus, there may be a bedform topographic configuration where local relief of bedform patches may not be

capable of increasing beyond a threshold simply due to individual particle mobility regardless of turbulent flow structure.

The apparent diminishing returns of bedform topographic heterogeneity with increased flow depth has meaningful implications for scientists and river managers. These observations suggest that low overbank flows and densely vegetated floodplains are functionally important for driving in-channel complexity that sustains ecosystem processes.

*2.4.2 Sediment transport*

These results suggest that the relationship between flow depth and sediment transport in compound channels is partially driven by planform geometry. Experiments conducted in high sinuosity flumes ($k > 1.3$) with mobile sand beds showed that as stage increased from bankfull to low overbank flow, sediment transport decreased (Karamisheva et al., 2006; Lyness et al., 2001; Shiono et al., 2009a, 2009b; Wormleaton et al., 2004, 2005). This is different from observations made in straight compound channels, where sediment transport monotonically increases with stage, even at low overbank flows (Atabay et al., 2005; Tang & Knight, 2006). I tested my hypothesis that sediment transport would be higher at low overbank flows in a low sinuosity experiment ($k = 1.07$) regardless of floodplain vegetation. Because there are very few meandering compound flume experiments described in the literature, I classify those with "high" sinuosity as $k > 1.3$, for simple comparison although I acknowledge that in the geomorphology literature high sinuosity channels have been classified as $k > 1.5$ (Leopold & Wolman, 1957).

In contrast to Shiono et al. (2009a, 2009b), I observed that sediment transport was higher at low relative depth than at bankfull and increased with floodplain vegetation density. These observations are likely due to turbulent energy dissipation at the channel-floodplain interface

resulting from differences in flow angle and magnitude for floodplain and main channel flows. In my experiments, flow at the surface in the main channel was closely aligned with the channel centerline departing from the downvalley oriented floodplain flow by less than 30 degrees. Had the floodplain been narrower, floodplain walls may have had a small influence of flow orientation by deflecting flows toward the channel. However, as observed by Shiono et al. (2009a) in experiments that included floodplain sections that were less than one channel-width wide, I also did not observe significant influence of the flume walls on floodplain flow orientation. This is likely due in part to the shallow nature of flow, as the proportion of surface area interacting with flows is very small relative to the floodplain surface and vegetation frontal area. There was also relatively lower conveyance in the floodplain. In my low-sinuosity experiment, this low difference in downvalley flow and downstream flow in the cross-over region likely resulted in less energy loss than in high sinuosity experiments (Shiono et al., 2009a, 2009b). These observations prompt the need to further investigations on potential sinuosity thresholds at which sediment transport drops below bankfull for low relative depths.

### *2.4.3 Implications for natural channels and restoration*

Channel realignment is a common practice in river restoration. Engineers and geomorphologists often strive to design reaches with sediment transport capacity that matches upstream sediment supply to avoid excessive incision or aggradation. my reported observations of sediment transport capacity indicate that channel planform and the hydrodynamic effects of floodplain flows in rivers with varied floodplain vegetation conditions should be considered to achieve stable condtions.

Recent ecocentric management strategies recognize that healthy floodplains benefit both humans and riparian ecosystems and aim to optimize river health and function (Castro & Thorne,

2019; Johnson et al., 2020; Palmer et al., 2005). River restoration generally involves the use of technical tools such as hydraulic models to predict flow conditions for reconfigured channels that aim to increase habitat heterogeneity (Tamagnone et al., 2020) by incorporating hydrogeomorphic complexity, an emergent property of functional riparian ecosystems (Ward et al., 1999; Wohl, 2016a, 2016b). The basis of hydraulic river restoration design is often limited to bankfull flow, but overbank flow is occasionally simulated by applying an oversimplified single roughness coefficient across the computational surface ignoring biologic drivers of river form.

Approaches to river and floodplain restoration vary in their attempts to restore river corridor processes (Wohl et al., 2005). Most commonly, active channel planform and cross-section geometry are the focus of restoration design (Dufour & Piégay, 2009; Shields et al., 2003; Wharton, 1995), though Beechie et al. (2010) emphasize the importance of restoring the natural geomorphic and ecological processes that rivers support. Recently, Castro & Thorne (2019) and Johnson et al. (2020) point out that while some river restoration projects focus on geomorphic and hydrologic processes, biological restoration remains an afterthought despite its relative importance. Biological drivers of river form and function include keystone species like beaver (*Castor canadensis*), salmonids, arthropods, large wood, biogeochemical nutrient cycling, and vegetation, many of which occur in floodplains and have been the focus of recent restoration projects. I show that the effects of floodplain vegetation density and overbank flow are important drivers of in-channel processes such as sediment transport and topographic heterogeneity, a characteristic associated with habitat suitability, biodiversity, and flux attenuation (Wohl, 2016b).

The development of heterogeneous bedform features at high floodplain vegetation density and overbank flow depths has significant implications for natural channel evolution

processes. In this experiment, bedform topography is analyzed under a quasi-equilibrium state; however, natural channels experiencing unsteady flow may also develop elevated topographic patches during floods which emerge as stage recedes, producing mid-channel bars and potentially suitable conditions where early successional trees and woody shrubs may become established.

### *2.4.4 Study Limitations*

Floodplain vegetation was limited to a single diameter and spaced across the entire surface evenly in this experiment for simplicity although in natural channels, the understory and trees exhibit a range of diameters, density configurations, and leaf properties. The geomorphic response to these plant properties was not the primary focus of this study; however, others have explored this interaction (Diehl et al., 2017). Leaf density and associated metrics, such as leaf area index (LAI), would likely influence the flow field and resulting bed topography. Leafy vegetation would likely enhance the assumed steering effect that vegetation had and promote bed topographic complexity.

For each of the seven flume runs, I determined that quasi-equilibrium conditions had been reached by comparing bedform topography between operation periods and confirmed that no significant aggradation or degradation was occurring. The channel slope, shown in Figure 2.4h, also indicates that topographic quasi-equilibrium was achieved. I also compared the sediment transport and feed rates to assess quasi-equilibrium, however, for some periods of operation, the sediment feed rate was not in strict equilibrium with sediment being exported from the flume. I determined that the temporary storage and export of sediment that may have contributed to this slight feed-transport disequilibrium was negligible relative to overall bedform change and likely did not contribute to significant topographic changes. Any difference in

sediment feed or export may also influence the results and relationship of relative depth, floodplain vegetation density, and transport capacity; however, this potential difference in fact suggests that the monotonic increase in sediment transport with relative depth would be enhanced and supports the discussion and conclusion as such.

## 2.5 Conclusion

I performed experiments in a compound meandering channel to investigate the effects of floodplain vegetation density on bedform heterogeneity and sediment transport. The experiments were conducted in a low-sinuosity flume with a mobile sand and gravel bed. I tested the extent to which floodplain vegetation density increases topographic complexity within the channel by analyzing surface metrics using a moving-window (skewness, standard deviation, coefficient of variation) and patch-based (relative contagion index, patch areas, patch number) computations and found that increased vegetation density and flood depth produced greater geomorphic complexity. I observed an increase in sediment transport rate relative to bankfull conditions at low relative depths for all floodplain cover conditions, which contrast with findings of other studies that used higher sinuosity and finer bed material. I believe this is primarily due to differences in planform between my experiments and previous work, and lower energy loss at the channel-floodplain boundary in my lower sinuosity channel, but particle mobility may also influence these findings. These results show that biologic factors drive in-channel morphodynamic processes and should be considered in river restoration practice.

1

## 2.6 References


Agisoft Metashape Professional. (2022). (Version 1.8.1). Agisoft LLC. Retrieved from http://www.agisoft.com

Atabay, S., Knight, D. W., & Seckin, G. (2005). Effects of overbank flow on fluvial sediment transport rates. *Proceedings of the Institution of Civil Engineers - Water Management*, *158*(1), 25–34. https://doi.org/10.1680/wama.2005.158.1.25

Badgley, C., Smiley, T. M., Terry, R., Davis, E. B., DeSantis, L. R. G., Fox, D. L., et al. (2017). Biodiversity and Topographic Complexity: Modern and Geohistorical Perspectives. *Trends in Ecology & Evolution*, *32*(3), 211–226. https://doi.org/10.1016/j.tree.2016.12.010

Beechie, T. J., Sear, D. A., Olden, J. D., Pess, G. R., Buffington, J. M., Moir, H., et al. (2010). Process-based Principles for Restoring River Ecosystems. *BioScience*, *60*(3), 209–222. https://doi.org/10.1525/bio.2010.60.3.7

Bellmore, J. R., & Baxter, C. V. (2014). Effects of Geomorphic Process Domains on River Ecosystems: A Comparison of Floodplain and Confined Valley Segments. *River Research and Applications*, *30*(5), 617–630. https://doi.org/10.1002/rra.2672

Box, W., Västilä, K., & Järvelä, J. (2019). The Interplay between Flow Field, Suspended Sediment Concentration, and Net Deposition in a Channel with Flexible Bank Vegetation. *Water*, *11*(11), 2250. https://doi.org/10.3390/w11112250

Branß, T., & Aberle, J. (2022). Combined effect of a mobile bed and floodplain edge vegetation on compound channel conveyance. *Journal of Hydraulic Research*, *60*(5), 826–834.

Braudrick, C. A., Dietrich, W. E., Leverich, G. T., & Sklar, L. S. (2009). Experimental evidence for the conditions necessary to sustain meandering in coarse-bedded rivers. *Proceedings of the National Academy of Sciences*, *106*(40), 16936–16941.

Brooks, A. C., Covino, T., & Hall, E. K. (2022). Evaluating Spatial and Temporal Dynamics of River-Floodplain Surface Water Connectivity Using Hydrometric, Geochemical and Microbial Indicators. *Water Resources Research*, *58*(5), e2021WR030336.

Buffington, J. M., & Montgomery, D. R. (1999). Effects of hydraulic roughness on surface textures of gravel-bed rivers. *Water Resources Research*, *35*(11), 3507–3521. https://doi.org/10.1029/1999WR900138

Bywater-Reyes, S., Wilcox, A. C., & Diehl, R. M. (2017). Multiscale influence of woody riparian vegetation on fluvial topography quantified with ground-based and airborne lidar. *Journal of Geophysical Research: Earth Surface*, *122*(6), 1218–1235. https://doi.org/10.1002/2016JF004058

Calvani, G., Francalanci, S., & Solari, L. (2023). Insights Into the Dynamics of Vegetated Alternate Bars by Means of Flume Experiments. *Water Resources Research*, *59*(3), e2022WR032536. https://doi.org/10.1029/2022WR032536

Carpenter, S. R., DeFries, R., Dietz, T., Mooney, H. A., Polasky, S., Reid, W. V., & Scholes, R. J. (2006). *Millennium ecosystem assessment: research needs*. *Science* (Vol. 314, pp. 257–258). American Association for the Advancement of Science.

Carpenter, S. R., Mooney, H. A., Agard, J., Capistrano, D., DeFries, R. S., Díaz, S., et al. (2009). Science for managing ecosystem services: Beyond the Millennium Ecosystem Assessment. *Proceedings of the National Academy of Sciences*, *106*(5), 1305–1312.

Castro, J. M., & Thorne, C. R. (2019). The stream evolution triangle: Integrating geology, hydrology, and biology. *River Res. Appl.*, *12*, 201. https://doi.org/10.1002/rra.3421

Christensen, N. D., Czuba, J. A., Triantafillou, S., Copenheaver, C. A., Peterson, J. A., & Hession, W. C. (2022). Establishment and Persistence of Trees Growing in the Channel of an Intermittent Stream in a Temperate, Karst Environment. *Water Resources Research*, *58*(5), e2021WR031528. https://doi.org/10.1029/2021WR031528

Davies, T. R., & Sutherland, A. J. (1980). Resistance to flow past deformable boundaries. *Earth Surface Processes*, *5*(2), 175–179. https://doi.org/10.1002/esp.3760050207

Davies, Timothy RH, & Sutherland, A. J. (1983). Extremal hypotheses for river behavior. *Water Resources Research*, *19*(1), 141–148.

Diehl, R. M., Merritt, D. M., Wilcox, A. C., & Scott, M. L. (2017). Applying Functional Traits to Ecogeomorphic Processes in Riparian Ecosystems. *BioScience*, *67*(8), 729–743. https://doi.org/10.1093/biosci/bix080

Dietrich, W. E., & Whiting, P. (1989). Boundary shear stress and sediment transport in river meanders of sand and gravel. *Water Resources Monograph*, 1–50. https://doi.org/10.1029/wm012p0001

Dietrich, W. E., Nelson, P. A., Yager, E., Venditti, J. G., & Lamb, M. P. (2005). Sediment patches, sediment supply, and channel morphology. In *4th Conference on River, Coastal and Estuarine Morphodynamics 2005* (Vol. 1, pp. 79–90). A. A. Balkema, Rotterdam.

Dufour, S., & Piégay, H. (2009). From the myth of a lost paradise to targeted river restoration: forget natural references and focus on human benefits. *River Research and Applications*, *25*(5), 568–581. https://doi.org/10.1002/rra.1239

Eaton, B. C., Church, M., & Millar, R. G. (2004). Rational regime model of alluvial channel morphology and response. *Earth Surface Processes and Landforms*, *29*(4), 511–529.

Ervine D. A., Willetts B. B., Sellin R. H. J., & Lorena M. (1993). Factors Affecting Conveyance in Meandering Compound Flows. *Journal of Hydraulic Engineering*, *119*(12), 1383–1399. https://doi.org/10.1061/(ASCE)0733-9429(1993)119:12(1383)

Friedman, J. M., & Lee, V. J. (2002). Extreme Floods, Channel Change, and Riparian Forests Along Ephemeral Streams. *Ecological Monographs*, *72*(3), 409–425. https://doi.org/10.1890/0012-9615(2002)072[0409:EFCCAR]2.0.CO;2

Gooseff, M. N., Hall Jr., R. O., & Tank, J. L. (2007). Relating transient storage to channel complexity in streams of varying land use in Jackson Hole, Wyoming. *Water Resources Research*, *43*(1). https://doi.org/10.1029/2005WR004626

Harvey, Jud, & Gooseff, M. (2015). River corridor science: Hydrologic exchange and ecological consequences from bedforms to basins. *Water Resources Research*, *51*(9), 6893–6922. https://doi.org/10.1002/2015WR017617

Harvey, JW. (2016). Hydrologic exchange flows and their ecological consequences in river corridors. In *Stream ecosystems in a changing environment* (pp. 1–83). Elsevier.

Hassan, M. A., & Reid, I. (1990). The influence of microform bed roughness elements on flow and sediment transport in gravel bed rivers. *Earth Surface Processes and Landforms*, *15*(8), 739–750.

Hinshaw, S., Wohl, E., Burnett, J. D., & Wondzell, S. (2022). Development of a geomorphic monitoring strategy for stage 0 restoration in the South Fork McKenzie River, Oregon, USA. *Earth Surface Processes and Landforms*, *47*(8), 1937–1951.

Ielpi, A., Lapôtre, M. G. A., Gibling, M. R., & Boyce, C. K. (2022). The impact of vegetation on meandering rivers. *Nature Reviews Earth & Environment*, *3*(3), 165–178. https://doi.org/10.1038/s43017-021-00249-6

Ikeda, S. (1984). Prediction of alternate bar wavelength and height. *Journal of Hydraulic Engineering*, *110*(4), 371–386.

Iskin, E. P., & Wohl, E. (2023). Quantifying floodplain heterogeneity with field observation, remote sensing, and landscape ecology: Methods and metrics. *River Research and Applications*.

Johnson, M. F., Thorne, C. R., Castro, J. M., Kondolf, G. M., Mazzacano, C. S., Rood, S. B., & Westbrook, C. (2020). Biomic river restoration: A new focus for river management. *River Research and Applications*, *36*(1), 3–12. https://doi.org/10.1002/rra.3529

Karamisheva, R. D., Lyness, J. F., Myers, W. R. C., & O'Sullivan, J. (2006). Sediment discharge prediction in meandering compound channels. *Journal of Hydraulic Research*, *44*(5), 603–613. https://doi.org/10.1080/00221686.2006.9521710

Knight, D. W., & Shiono, K. (1990). Turbulence measurements in a shear layer region of a compound channel. *Journal of Hydraulic Research*, *28*(2), 175–196. https://doi.org/10.1080/00221689009499085

Knight, Donald W., & Demetriou, J. D. (1983). Flood Plain and Main Channel Flow Interaction. *Journal of Hydraulic Engineering*, *109*(8), 1073–1092. https://doi.org/10.1061/(ASCE)0733-9429(1983)109:8(1073)

Lane, E. W. (1955). Importance of fluvial morphology in hydraulic engineering. *Proceedings (American Society of Civil Engineers); v. 81, Paper No. 745*.

Lauer, J. W., & Parker, G. (2008). Modeling framework for sediment deposition, storage, and evacuation in the floodplain of a meandering river: Theory. *Water Resources Research*, *44*(4).

Leduc, P., Peirce, S., & Ashmore, P. (2019). Short communication: Challenges and applications of structure-from-motion photogrammetry in a physical model of a braided river. *Earth Surface Dynamics*, *7*(1), 97–106. https://doi.org/10.5194/esurf-7-97-2019

Li, H., & Reynolds, J. F. (1993). A new contagion index to quantify spatial patterns of landscapes. *Landscape Ecology*, *8*(3), 155–162.

Lightbody, A. F., Kui, L., Stella, J. C., Skorko, K. W., Bywater-Reyes, S., & Wilcox, A. C. (2019). Riparian Vegetation and Sediment Supply Regulate the Morphodynamic Response of an Experimental Stream to Floods. *Frontiers in Environmental Science*, *7*. https://doi.org/10.3389/fenvs.2019.00040

Lyness, J. F., Myers, W. R. C., Cassells, J. B. C., & O'Sullivan, J. J. (2001). The influence of planform on flow resistance in mobile bed compound channels. In *Proceedings of the Institution of Civil Engineers-Water and Maritime Engineering* (Vol. 148, pp. 5–14). Thomas Telford Ltd. Retrieved from https://sci-hub.se/https://doi.org/10.1680/wame.2001.148.1.5

Martin, R. L., & Jerolmack, D. J. (2013). Origin of hysteresis in bed form response to unsteady flows. *Water Resources Research*, *49*(3), 1314–1333.

Modalavalasa, S., Chembolu, V., Dutta, S., & Kulkarni, V. (2023). Laboratory investigation on flow structure and turbulent characteristics in low sinuous compound channels with vegetated floodplains. *Journal of Hydrology*, *618*, 129178. https://doi.org/10.1016/j.jhydrol.2023.129178

Montgomery, D. R., & Buffington, J. M. (1997). Channel-reach morphology in mountain drainage basins. *Geological Society of America Bulletin*, *109*(5), 596–611. https://doi.org/10.1130/0016-7606(1997)109<0596:crmimd>2.3.co;2

Morán-Ordóñez, A., Pavlova, A., Pinder, A. M., Sim, L., Sunnucks, P., Thompson, R. M., & Davis, J. (2015). Aquatic communities in arid landscapes: local conditions, dispersal traits and landscape configuration determine local biodiversity. *Diversity and Distributions*, *21*(10), 1230–1241. https://doi.org/10.1111/ddi.12342

Morgan, J. A., Brogan, D. J., & Nelson, P. A. (2017). Application of Structure-from-Motion photogrammetry in laboratory flumes. *Geomorphology*, *276*, 125–143. https://doi.org/10.1016/j.geomorph.2016.10.021

Myers, W. R. C. (1978). Momentum Transfer In A Compound Channel. *Journal of Hydraulic Research*, *16*(2), 139–150. https://doi.org/10.1080/00221687809499626

Nanson, G. C., & Huang, H. Q. (2008). Least action principle, equilibrium states, iterative adjustment and the stability of alluvial channels. *Earth Surface Processes and Landforms*, *33*(6), 923–942. https://doi.org/10.1002/esp.1584

Nanson, G. C., & Huang, H. Q. (2017). Self-adjustment in rivers: Evidence for least action as the primary control of alluvial-channel form and process. *Earth Surface Processes and Landforms*, *42*(4), 575–594.

National Research Council. (2002). *Riparian areas: functions and strategies for management*. National Academies Press.

Nelson, P. A., & Morgan, J. A. (2018). Flume experiments on flow and sediment supply controls on gravel bedform dynamics. *Geomorphology*, *323*, 98–105. https://doi.org/10.1016/j.geomorph.2018.09.011

Nelson, P. A., Bellugi, D., & Dietrich, W. E. (2014). Delineation of river bed-surface patches by clustering high-resolution spatial grain size data. *Geomorphology*, *205*, 102–119. https://doi.org/10.1016/j.geomorph.2012.06.008

Olde Venterink, H., Vermaat, J. E., Pronk, M., Wiegman, F., van der Lee, G. E. M., van den Hoorn, M. W., et al. (2006). Importance of sediment deposition and denitrification for nutrient retention in floodplain wetlands. *Applied Vegetation Science*, *9*(2), 163–174. https://doi.org/10.1111/j.1654-109X.2006.tb00665.x

Over, J.-S. R., Ritchie, A. C., Kranenburg, C. J., Brown, J. A., Buscombe, D. D., Noble, T., et al. (2021). *Processing coastal imagery with Agisoft Metashape Professional Edition, version 1.6—Structure from motion workflow documentation* (No. 2331–1258). US Geological Survey.

Palmer, M. a., Bernhardt, E. s., Allan, J. D., Lake, P. s., Alexander, G., Brooks, S., et al. (2005). Standards for ecologically successful river restoration. *Journal of Applied Ecology*, *42*(2), 208–217. https://doi.org/10.1111/j.1365-2664.2005.01004.x

Palucis, M. C., Ulizio, T. P., Fuller, B., & Lamb, M. P. (2018). Flow resistance, sediment transport, and bedform development in a steep gravel-bedded river flume. *Geomorphology*, *320*, 111–126. https://doi.org/10.1016/j.geomorph.2018.08.003

Parker, G. (1990). Surface-based bedload transport relation for gravel rivers. *Journal of Hydraulic Research*, *28*(4), 417–436. https://doi.org/10.1080/00221689009499058

Powell, D. M. (2014). Flow resistance in gravel-bed rivers: Progress in research. *Earth-Science Reviews*, *136*, 301–338. https://doi.org/10.1016/j.earscirev.2014.06.001

Riitters, K. H., O'Neill, R. V., Wickham, J. D., & Jones, K. B. (1996). A note on contagion indices for landscape analysis. *Landscape Ecology*, *11*(4), 197–202.

Sawyer, A. H., & Cardenas, M. B. (2012). Effect of experimental wood addition on hyporheic exchange and thermal dynamics in a losing meadow stream. *Water Resources Research*, *48*(10).

von Schiller, D., Acuña, V., Aristi, I., Arroita, M., Basaguren, A., Bellin, A., et al. (2017). River ecosystem processes: A synthesis of approaches, criteria of use and sensitivity to environmental stressors. *Science of The Total Environment*, *596–597*, 465–480. https://doi.org/10.1016/j.scitotenv.2017.04.081

Scott, D. N., Shahverdian, S., Flitcroft, R., & Wohl, E. (2022). Geomorphic heterogeneity as a framework for assessing river corridor processes and characteristics. *River Research and Applications*.

Scown, M. W., Thoms, M. C., & De Jager, N. R. (2015). Floodplain complexity and surface metrics: Influences of scale and geomorphology. *Geomorphology*, *245*, 102–116. https://doi.org/10.1016/j.geomorph.2015.05.024

Sear, D. A. (1996). Sediment Transport Processes in Pool–Riffle Sequences. *Earth Surface Processes and Landforms*, *21*(3), 241–262. https://doi.org/10.1002/(SICI)1096-9837(199603)21:3<241::AID-ESP623>3.0.CO;2-1

SELLIN, R. H. J., ERVINE, D. A., & WILLETTS, B. B. (1993). BEHAVIOUR OF MEANDERING TWO-STAGE CHANNELS. *Proceedings of the Institution of Civil Engineers - Water, Maritime and Energy*, *101*(2), 99–111. https://doi.org/10.1680/iwtme.1993.23591

Serra-Llobet, A., Jähnig, S. C., Geist, J., Kondolf, G. M., Damm, C., Scholz, M., et al. (2022). Restoring rivers and floodplains for habitat and flood risk reduction: experiences in

multi-benefit floodplain management from California and Germany. *Frontiers in Environmental Science*, *9*, 778568.

Shields, F. D., Copeland, R. R., Klingeman, P. C., Doyle, M. W., & Simon, A. (2003). Design for Stream Restoration. *Journal of Hydraulic Engineering*, *129*(8), 575–584. https://doi.org/10.1061/(ASCE)0733-9429(2003)129:8(575)

Shiono, K., & Muto, Y. (1998). Complex flow mechanisms in compound meandering channels with overbank flow. *Journal of Fluid Mechanics*, *376*, 221–261. https://doi.org/10.1017/S0022112098002869

Shiono, K., Chan, T. L., Spooner, J., Rameshwaran, P., & Chandler, J. H. (2009a). The effect of floodplain roughness on flow structures, bedforms and sediment transport rates in meandering channels with overbank flows: Part I. *Journal of Hydraulic Research*, *47*(1), 5–19. https://doi.org/10.3826/jhr.2009.2944-I

Shiono, K., Chan, T. L., Spooner, J., Rameshwaran, P., & Chandler, J. H. (2009b). The effect of floodplain roughness on flow structures, bedforms and sediment transport rates in meandering channels with overbank flows: Part II. *Journal of Hydraulic Research*, *47*(1), 20–28. https://doi.org/10.3826/jhr.2009.2944-II

Sholtes, J. S., & Doyle, M. W. (2011). Effect of Channel Restoration on Flood Wave Attenuation. *Journal of Hydraulic Engineering*, *137*(2), 196–208. https://doi.org/10.1061/(ASCE)HY.1943-7900.0000294

Stoffers, T., Buijse, A., Geerling, G., Jans, L., Schoor, M., Poos, J., et al. (2022). Freshwater fish biodiversity restoration in floodplain rivers requires connectivity and habitat heterogeneity at multiple spatial scales. *Science of The Total Environment*, *838*, 156509.

Strange, E. M., Fausch, K. D., & Covich, A. P. (1999). Sustaining Ecosystem Services in Human-Dominated Watersheds: Biohydrology and Ecosystem Processes in the South Platte River Basin, 17.

Surfer. (2022). Golden Software, LLC. Retrieved from www.goldensoftware.com

Tal, M., & Paola, C. (2010). Effects of vegetation on channel morphodynamics: results and insights from laboratory experiments. *Earth Surf. Processes Landforms*, *35*(9), 1014–1028. https://doi.org/10.1002/esp.1908

Tamagnone, P., Comino, E., & Rosso, M. (2020). Landscape Metrics Integrated in Hydraulic Modeling for River Restoration Planning. *Environmental Modeling & Assessment*, *25*(2), 173–185. https://doi.org/10.1007/s10666-020-09693-y

Tang, X., & Knight, D. W. (2006). Sediment Transport in River Models with Overbank Flows. *Journal of Hydraulic Engineering*, *132*(1), 77–86. https://doi.org/10.1061/(ASCE)0733-9429(2006)132:1(77)

Termini, D. (2009). Experimental Observations of Flow and Bed Processes in Large-Amplitude Meandering Flume. *Journal of Hydraulic Engineering*, *135*(7), 575–587. https://doi.org/10.1061/(ASCE)HY.1943-7900.0000046

Tonina, D., & Buffington, J. M. (2007). Hyporheic exchange in gravel bed rivers with pool-riffle morphology: Laboratory experiments and three-dimensional modeling. *Water Resources Research*, *43*(1).

Török, G. T., & Parker, G. (2022). The influence of riparian woody vegetation on bankfull alluvial river morphodynamics. *Scientific Reports*, *12*(1), 18141. https://doi.org/10.1038/s41598-022-22846-1

Ward, A. S., & Packman, A. I. (2019). Advancing our predictive understanding of river corridor exchange. *WIREs Water*, *6*(1), e1327. https://doi.org/10.1002/wat2.1327

Ward, J. v., Tockner, K., & Schiemer, F. (1999). Biodiversity of floodplain river ecosystems: ecotones and connectivity1. *Regulated Rivers: Research & Management*, *15*(1–3), 125–139. https://doi.org/10.1002/(SICI)1099-1646(199901/06)15:1/3<125::AID-RRR523>3.0.CO;2-E

Westbrook, C. J., Cooper, D. J., & Baker, B. W. (2006). Beaver dams and overbank floods influence groundwater–surface water interactions of a Rocky Mountain riparian area. *Water Resources Research*, *42*(6).

Westoby, M. J., Brasington, J., Glasser, N. F., Hambrey, M. J., & Reynolds, J. M. (2012). 'Structure-from-Motion' photogrammetry: A low-cost, effective tool for geoscience applications. *Geomorphology*, *179*, 300–314. https://doi.org/10.1016/j.geomorph.2012.08.021

Wharton, G. (1995). The channel-geometry method: Guidelines and applications. *Earth Surface Processes and Landforms*, *20*(7), 649–660. https://doi.org/10.1002/esp.3290200707

White, D. C., Morrison, R. M., & Nelson, P. A. (2023). Dataset associated with "Experimental observations of floodplain vegetation, bedforms, and sediment transport interactions in a meandering channel" [Data set]. HydroShare. Retrieved from https://www.hydroshare.org/resource/9922d4f4a0d5409da0860217dc1b55b0/

White, Daniel C, & Nelson, P. A. (2023). Flume investigation into mechanisms responsible for particle sorting in gravel-bed meandering channels. *Journal of Geophysical Research: Earth Surface*, e2022JF006821.

Wieting, C., Friedman, J. M., & Rathburn, S. (2023). River channel response to invasive plant treatment across the American Southwest. *Earth Surface Processes and Landforms*, *48*(3), 569–581. https://doi.org/10.1002/esp.5503

Wilcock, P. R., & Crowe, J. C. (2003). Surface-based Transport Model for Mixed-Size Sediment. *Journal of Hydraulic Engineering*, *129*(2), 120–128. https://doi.org/10.1061/(ASCE)0733-9429(2003)129:2(120)

Williams, R. D., Bangen, S., Gillies, E., Kramer, N., Moir, H., & Wheaton, J. (2020). Let the river erode! Enabling lateral migration increases geomorphic unit diversity. *Science of The Total Environment*, *715*, 136817. https://doi.org/10.1016/j.scitotenv.2020.136817

Wohl, E. (2016a). Messy rivers are healthy rivers: The role of physical complexity in sustaining ecosystem processes. In *River flow* (Vol. 2016, pp. 24–29).

Wohl, E. (2016b). Spatial heterogeneity as a component of river geomorphic complexity. *Progress in Physical Geography*, *40*(4), 598–615.

Wohl, E. (2017). Connectivity in rivers. *Progress in Physical Geography: Earth and Environment*, *41*(3), 345–362. https://doi.org/10.1177/0309133317714972

Wohl, E. (2020). Wood process domains and wood loads on floodplains. *Earth Surface Processes and Landforms*, *45*(1), 144–156.

Wohl, E., & Merritt, D. M. (2008). Reach-scale channel geometry of mountain streams. *Geomorphology*, *93*(3), 168–185. https://doi.org/10.1016/j.geomorph.2007.02.014

Wohl, E., Angermeier, P. L., Bledsoe, B., Kondolf, G. M., MacDonnell, L., Merritt, D. M., et al. (2005). River restoration. *Water Resources Research*, *41*(10). https://doi.org/10.1029/2005WR003985

Wohl, E., Marshall, A. E., Scamardo, J., White, D., & Morrison, R. R. (2022). Biogeomorphic influences on river corridor resilience to wildfire disturbances in a mountain stream of the Southern Rockies, USA. *Science of The Total Environment*, 153321. https://doi.org/10.1016/j.scitotenv.2022.153321

Wong, M., & Parker, G. (2006). Reanalysis and Correction of Bed-Load Relation of Meyer-Peter and Müller Using Their Own Database. *Journal of Hydraulic Engineering*, *132*(11), 1159–1168. https://doi.org/10.1061/(ASCE)0733-9429(2006)132:11(1159)

Wormleaton, P. R., Sellin, R. H. J., Bryant, T., Loveless, J. H., Hey, R. D., & Catmur, S. E. (2004). Flow structures in a two-stage channel with a mobile bed. *Journal of Hydraulic Research*, *42*(2), 145–162.

Wormleaton, P. R., Hey, R. D., Sellin, R. H., Bryant, T., Loveless, J., & Catmur, S. E. (2005). Behavior of Meandering Overbank Channels with Graded Sand Beds. *Journal of Hydraulic Engineering*, *131*(8), 665–681. https://doi.org/10.1061/(ASCE)0733-9429(2005)131:8(665)

Yang, J. Q., & Nepf, H. M. (2019). Impact of vegetation on bed load transport rate and bedform characteristics. *Water Resources Research*, *55*(7), 6109–6124.

# CHAPTER 3: FLOODPLAIN VEGETATION DENSITY INFLUENCES MEANDERING CHANNEL FLOW PATTERNS

## 3.1 Introduction

Floodplain vegetation can influence numerous hydraulic, geomorphic, and biogeochemical processes in rivers. For instance, vegetation mechanically stabilizes banks (Zhu et al., 2022), increases reach-averaged hydraulic roughness during floods (Hickin, 1984; Millar, 2000) thus reducing flow velocities and increasing residence time (Box et al., 2021), and creates complex flow patterns within and around vegetation patches (Nepf, 1999). These hydraulic effects promote biogeochemical processes and carbon storage (Lininger et al., 2019; Steiger & Gurnell, 2003; Sutfin et al., 2016). They also promote riparian seedling recruitment and natural vegetation succession (Benjankar et al., 2012; Geerling et al., 2008) and enhance important terrestrial and aquatic habitat (Beschta, 1997; Fuller et al., 2022; Theurer et al., 1985).

Furthermore, floodplain vegetation can influence channel morphology (Beechie et al., 2006; Camporeale et al., 2013; Ielpi et al., 2022; Kondolf & Curry, 1986; Lightbody et al., 2019) as evidenced by field observations and numerical studies investigating the relationship between vegetation density and channel width (Liébault & Piégay, 2002; Török & Parker, 2022), meander migration rates (Perucca et al., 2007), and channel response to vegetation patches (Bywater-Reyes et al., 2017, 2022). These well documented examples of the influence of vegetation on reach-scale river-corridor processes and ecological function highlight its importance at large scales and prompt study of the interaction of vegetation and flow from a fluid mechanics and hydraulic engineering perspective.

The physical characteristics of vegetation such as stem density, diameter, rigidity, and leaf area are important to consider in the context of floods and hydraulic resistance. Various physical modeling studies have been conducted with varied vegetation shapes, rigidities, and strengths such as single rigid cylinders, flexible elements, or foliated live plants in flow experiments (Aberle & Järvelä, 2013; Järvelä, 2002, 2004; Le Bouteiller & Venditti, 2015; Nepf, 1999, 2012). Regardless of the specific vegetation characteristics used in experiments, studies show that form drag dramatically reduces mean flow within the vegetation canopy, or among the vegetative elements, and alters turbulent structures near each element (Aberle & Järvelä, 2013; Järvelä, 2005; Nepf, 1999, 2012; Tanino & Nepf, 2008; E. M. Yager & Schmeeckle, 2013). Various approaches have been taken to relate this resistance to plant properties, many of which incorporate frontal area as a function of stem density or leaf-area-index (Box et al., 2022; Bywater-Reyes et al., 2018). These studies and others have elucidated flow patterns through vegetation, however, the complex flow structure caused by vegetation is difficult to characterize as it interacts with three-dimensional (3-D) flow fields that develop in meandering compound channels.

The influence of vegetation on the 3-D compound channel flow field, both on the floodplain and within the channel is difficult to study and numerical or physical modeling studies are few; however, various studies have been conducted with bare floodplains, the results of which shape our understanding of flow through meandering compound channels. At the UK Flood Channel Facility (FCF), work by Ervine et al. (1993) and Sellin et al. (1993) described the three-dimensional nature of flows in meandering compound channels with fixed trapezoidal cross sections. They showed that floodplain flow re-entering the channel causes strong helical flow at the inner bank, and that conveyance is a function of floodplain roughness and channel

planform. Patra & Kar (2000) performed laboratory experiments of meandering compound channels showing that the proportion of total shear stress experienced by the floodplain is dependent on channel and valley geometry. Findings from these and other studies have shaped our understanding that sinuosity, flow depth, and channel geometry strongly influence the flow field in meandering compound channels.

Experimental studies have more closely approximated natural rivers by physically modeling flow through mobile-bed meandering compound flumes with roughened floodplains. Many show that both floodplain roughness characteristics and the proportion of flow in the floodplain can drive changes in channel bed morphology. Ishigaki et al. (2000) performed flume experiments investigating bedform response to overbank flow in meandering channels with a sand bed. As depth increased past bankfull, classic bar-pool morphology and associated secondary currents characteristic of meandering channels shifted toward more irregular patchy topography and at high relative depths developed wavy bedforms which were associated with multiple secondary current cells. In Chan (2003) and Shiono et al., (2009a, 2009b) a series of flume experiments are described in which the flow structure and topography of a mobile sand bed were observed. They describe multiple secondary flow cells spanning the width of the channel which were associated with wavy bedforms and more prevalent at high overbank flow depths. Wormleaton et al. (2004, 2005) modeled the effect of floodplain roughness on three-dimensional velocity field within the channel and associated bedforms. They showed that floodplain roughness results in decreased interaction of in-channel and overbank flows and that classic meandering channel secondary currents are enhanced. These studies in sand-bedded meandering compound flumes describe the flow field that results from increased floodplain roughness, but don't clearly identify the influence of floodplain vegetation density on secondary

flow field within the channel, on the flow field at the surface, and the resulting channel-floodplain exchange in a channel with a bed material coarser than sand.

An ecologically important aspect of flood hydrology is the exchange of energy as water, nutrients, and sediment pass from channel to floodplain. Czuba et al. (2019) developed a 2D hydraulic model of flow through a low-gradient river and investigated exchange flux at the channel-floodplain interface. They developed a conceptual framework to predict floodplain flow dynamics but did not account for varied floodplain vegetation conditions during floods or 3D flow characteristics that may contribute to channel-floodplain exchange. Stone et al. (2017) developed 2D hydraulic models to investigate the influence of hydrologic alterations on channel-floodplain mass exchange fluxes and found floodplain topographic variability to heavily influence channel-floodplain connectivity. Despite these informative studies, there remains a knowledge gap regarding the influence of floodplain vegetation on the 3D flow field in meandering compound channels and exchange flow at the channel-floodplain interface. This knowledge gap leads me to present the objectives of this current study which I carried out through a series of experimental flume runs in a meandering compound channel with varied floodplain vegetation density:

- Objective 1. Investigate the influence of floodplain vegetation density on the three-dimensional flow field within the channel and:
    - (a) Describe the influence of flow depth and vegetation density on secondary currents within the channel. Studies have described the reversal and weakening of secondary flow currents in meandering compound channels with sand beds. However, none have made observations in meandering compound channels with bed material coarser than sand or with varied floodplain vegetation density. Here I

present detailed measurements of the flow field within the channel and analyze the nature of secondary flow within the channel.

  - (b) Investigate the influence of the in-channel 3D flow field on shear stress calculations by comparing a method where shear stress is computed using 3D velocity measurements in the logarithmic region of flow near the bed and using local depth-averaged velocity measurements.

- Objective 2. Describe the influence of flow depth and vegetation density on the flow field at the surface. To my knowledge, there are no previous flume studies that systematically varied floodplain vegetation density in meandering compound flume experiments. Here I use large scale particle image velocimetry, LSPIV, to characterize the surface flow field across the floodplain and over the channel in scenarios including a bare floodplain, low-density vegetation, and high-density vegetation at two flow depths.

  I use these observations to analyze the influence of floodplain vegetation density on channel-floodplain exchange flow and identify examples in the flow field near the surface and within the channel. These observations and analysis provide new insights on channel-floodplain exchange in the context of hydrologic connectivity, river restoration, and river-corridor management strategies.

## 3.2 Methods

### *3.2.1 Experimental setup*

I performed flume experiments at the Colorado State University Engineering Research Center (ERC), Fort Collins, Colorado, USA (see Chapter 2 for detailed description of experimental setup). I constructed a 1-m wide meandering channel using expanded polystyrene foam blocks inset in a 15.4-m long, 4.9-m wide basin (Figure 3.1). The channel had a crossing angle of 30 degrees and the centerline followed a sine-generated trace defined by $\phi = \omega \sin\left(\frac{s}{M}\right) 2\pi$, where $\phi$ is the departure angle at location $s$ along the curve, $\omega$ is the maximum angle of departure $(30°)$, and $M$ is the meander wavelength (7.85 m). The channel banks were offset from the centerline to maintain constant width throughout the flume. The channel banks were fixed, and the bed was composed of a mobile sand and gravel mixture ($D_{50}$=3.3 mm) which was screeded flat to an initial slope of 0.005. General experimental parameters are listed in Table 3.1.

**Table 3.1.** Flume Parameters

| | |
|---|---|
| Sinuosity $(k)$/Crossing angle | 1.07/30° |
| Channel top width (m) | 1 |
| Initial channel bed and sediment feed $D_{16}$ (mm) | 1.9 |
| Initial channel bed and sediment feed $D_{50}$ (mm) | 3.3 |
| Initial channel bed and sediment feed $D_{84}$ (mm) | 5.1 |
| Valley slope (m/m) | 0.005 |
| Valley width (m) | 4.87 |
| Valley length (m) | 14.63 |
| Meander wavelength (m) | 7.85 |
| Cylindrical vegetation element diameter (cm) | 2.67 |

Seven flume runs were conducted over the course of the experiment at three relative depths ($D_r$), such that $D_r = \frac{h_{fp}}{h_{fp}+h_c}$ where $h_{fp}$ is the depth of flow on the floodplain and $h_c$ is the depth of flow in the channel. I also tested three floodplain vegetation conditions. For a description of the experimental parameters associated with each of the seven runs, see Table 2 At both overbank flow depths, three floodplain cover conditions were simulated including bare, low-density vegetation (3.0 stems/m$^2$), and high-density vegetation (12.1 stems/m$^2$) (Figure 3.1). Vegetation was simulated as rigid emergent cylindrical elements 2.67-cm in diameter spaced evenly across the floodplain. The geometric properties of the channel, floodplain, and vegetation scale at 1:20, which is approximating the size of a small-to medium sized river with middle-aged Cottonwood trees (*Populus* spp.) at spacings observed in Western North America (Friedman & Lee, 2002).

**Table 3.2**. Flume Run Scenarios

| Run | Discharge | Run Time | Sediment Supply | Floodplain Vegetation | Relative Depth |
|---|---|---|---|---|---|
| 1 | 0.04 m$^3$/s | 33.7 hr | 5 kg/hr | NA | (bankfull) |
| 2 | 0.08 m$^3$/s | 46.1 hr | 2.5 kg/hr | 0 | 0.1 |
| 3 | 0.08 m$^3$/s | 27.3 hr | 2.5 kg/hr | Low – 3.0 cylinders/m$^2$ | 0.1 |
| 4 | 0.08 m$^3$/s | 16.6 hr | 2.5 kg/hr | High – 12.1 cylinders/m$^2$ | 0.1 |
| 5 | 0.18 m$^3$/s | 26.8 hr | 80 kg/hr | High – 12.1 cylinders/m$^2$ | 0.25 |
| 6 | 0.17 m$^3$/s | 16.4 hr | 65 kg/hr | Low – 3.0 cylinders/m$^2$ | 0.25 |
| 7 | 0.16 m$^3$/s | 11.6 hr | 60 kg/hr | 0 | 0.25 |

During each of the experiments, sediment from the same bulk supply as that used to fill the channel during startup was fed into the channel at a rate matching observed sediment transport as measured by dried mass accumulated in the tailbox following each run over total run time. Flow and sediment feed rate were held constant to achieve quasi-equilbrium conditions

during which the bed was neither aggrading nor degrading and channel slope remained constant. Quasi-equilbrium conditions were determined by comparison of bed elevation change through time. Once quasi-equilibrium conditions were reached, I collected measurements of the flow field, bed topography, and sediment transport.

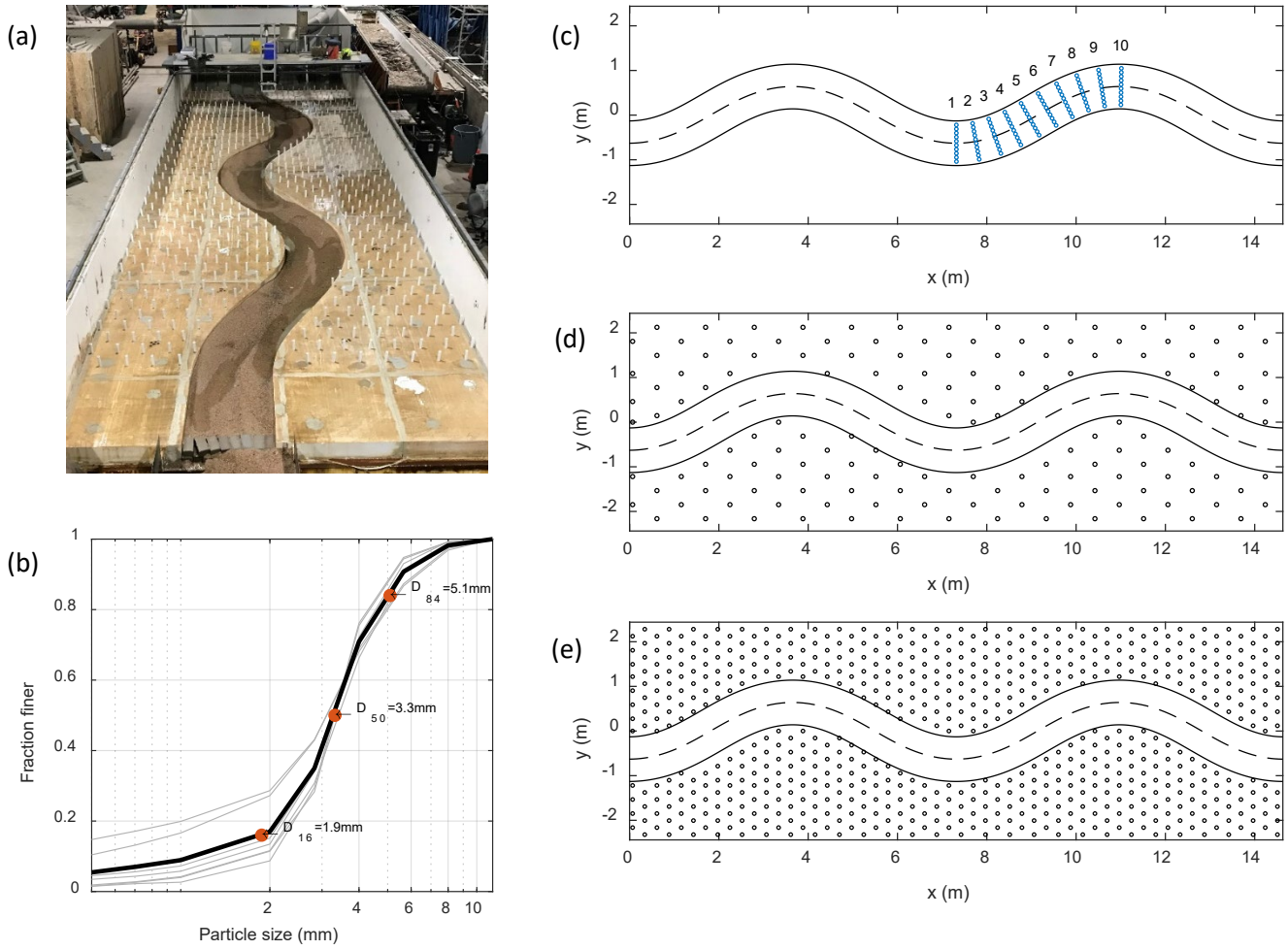


**Figure 3.1.** (a) Experimental flume configuration. Flow direction is from top to bottom of photo. (b) Bed material particle size distribution of sediment fed into the channel. (c) Laboratory flume channel configuration. Blue points represent locations at which I collected flow velocity measurements. Cross-section locations are numbered. (d) Low density (3.0 stems/m$^2$). (e) High density (12.1 stems/m$^2$)

### *3.2.2 In-channel velocity measurements*

I used the Nortek Vectrino Profiler, a profiling acoustic Doppler velocimeter (P-ADV), to measure the flow field within the channel. The profiler was mounted to an equipment cart which traveled the length of the flume and could be adjusted to take velocity measurements anywhere within the basin and referenced to a local coordinate system (See Figure 3.1). The P-ADV measures three-dimensional velocity at 200 Hz for 30 seconds in 30 1-mm-high increments spanning a 3-cm vertical window where flow depth is greater than 4.5 cm. In areas where flow depth was greater than the measurement control volume height, multiple stacked 3-cm velocity profiles were captured with the P-ADV, measuring as much of the water column as possible. The P-ADV is also capable of measuring the depth from the sensor to the bed and was used to verify the structure from motion bed topography measurements (See Chapter 2). P-ADV measurements were taken at 10 evenly spaced locations (0.91-m apart) through the water column for all 10 cross sections.

I despiked the profiler data using the method outlined by Goring & Nikora (2002) and modified by Mori et al. (2007). Because the flow depths were often less than 4.5 cm or near the channel banks, I processed the profiling ADV data by filtering the data to remove samples associated with low signal-to-noise-ratio (SNR), low correlation, or other uncharacteristic spikes was necessary using the Multi-Instrument Turbulence Toolbox (MacVicar, 2023). I performed a first-pass filter by removing measurements with beam correlation values lower than 60%, or SNR values less than 15 dB following a similar procedure outlined by MacVicar et al. (2014).

### *3.2.3 Shear stress calculations*

I compared two methods to calculate average bed shear stress. First, I used a single-velocity calculation method described by Wilcock (1996) and Dietrich & Whiting, (1989). In shallow flows where a full velocity profile could not be measured, a single velocity measurement in the logarithmic region can be used to estimate shear stress, $\tau$, with the law of the wall

$$u(z) = \frac{u_*}{\kappa} \ln\left(\frac{z}{z_0}\right) \tag{1}$$

where $u$(z) is the velocity magnitude at a height $z$ above the bed, $u_*$ is the shear velocity, $\kappa$ is the von-Karmann constant, taken here to be 0.4, and $z_0$ is the roughness height, estimated here to be $\frac{3D_{84}}{30}$, where $D_{84}$ is the grain size for which 84% of the bed material is finer after Dietrich & Whiting, (1989) and Wilcock, (1996). I computed the shear velocity for all points at height $z$ within the region where a logarithmic velocity profile is likely to occur such that $3D_{84} < z < \frac{h}{5}$. I then solved Equation 1 for $u_*$, and calculated shear stress, $\tau$ as:

$$\tau = \rho u_*^2. \tag{2}$$

where $\rho$ is the density of water (1000 kg/m$^3$). I then took an average of these computed shear stress values within the logarithmic region.

The second method I used to estimate shear stress used a single depth-averaged velocity measurement, $U$, and calculated shear stress as $\tau = \rho C_f U^2$ where $\rho$ is the density of water and $C_f$, is a roughness coefficient calculated using the Manning-Strickler approximation given by

$$C_f = \left[\alpha_r \left(\frac{H}{h_0}\right)^{\frac{1}{6}}\right]^{-2} \tag{3}$$

where $H$ is local depth, $\alpha_r = 8.1$ (Parker, 1991), and $h_0 = 2.95D_{84}$ (Whiting & Dietrich, 1990).

*3.2.4 Surface velocity measurements*

Due to the shallow flow conditions on the floodplain, I made surface velocity measurements using large scale particle image velocimetry (LSPIV), a technique that uses tracer displacement from image sequencing which is being used with increasing frequency in laboratory flumes and natural rivers (Fakhri et al., 2020; Legleiter & Kinzel III, 2021; Legleiter & Kinzel, 2020; Strelnikova et al., 2020). I applied LSPIV computations using the Fudaa-LSPIV software (Le Coz et al., 2014). I used color images sequenced from 30 fps video, captured at 3840- by 2160-pixel resolution (4K) with a fixed zoom, at approximately 3-m above the floodplain surface. I used small circular paper tracers that were 6-mm in diameter. During each LSPIV data collection period, I scattered the tracers at the upstream end of the flume and pointed the camera at a slightly upstream oblique angle (~15 degrees from nadir) to capture the half-meander of interest centered within the frame. Following the tracer tests, I orthorectified the images and referenced them to the local coordinate system using eight surveyed control points on the left and right walls of the flume near the water surface. The orthorectification process produced distortion error of less than 1 cm for each sequenced image. I then applied a rectangular grid with 0.2-m spacing where LSPIV computations would be performed. At each grid point, surface velocity was computed through time-series correlation comparison of pixels within a region that would capture displacement of particles between sequential photo frames. The displacement of tracers or similar pixel clusters divided by photo frame rate is their velocity.

Once results were computed for each image pair, I applied a correlation filter of 0.6, minimum velocity filter of 0.02 m/s, and maximum velocity filter of 1.5 m/s to correct for erroneous data and remove computed velocity vectors when no tracers were present in the

reference region following procedures described by Fakhri et al. (2020). In reference grid cells where a reflective glare was present or vegetation elements were located, Fudaa-LSPIV was unable to successfully compute surface velocities, so I also removed those data from my analyses. Finally, I time-averaged the velocity vectors across each of the 899 image pairs to visualize the surface flow field.

*3.2.5 Channel-floodplain exchange flow*

I followed a similar procedure as Czuba et al. (2019) to investigate channel-floodplain exchange flux with slightly modified notation suited to my experimental procedure. To measure channel-floodplain exchange fluxes I analyzed the LSPIV surface velocity measurements and estimated depth-averaged velocity and unit discharge across the channel-floodplain interface. Because the profiling ADV could only measure velocities at least 3-cm below the surface, I was unable to measure the complete velocity profile of shallow flows over the floodplain. A reasonable approximation of depth-averaged velocity for shallow flow can be determined using the coefficient, $\alpha$, where $\alpha = \boldsymbol{v}/\boldsymbol{U}$, $\boldsymbol{v}$ is the surface velocity vector, and $\boldsymbol{U}$ is the depth-averaged velocity vector. Here I take $\alpha$ to be 0.85 after Johnson & Cowen (2017) and Rantz (1982). I then performed a nearest neighbor search at coordinate pairs 3-cm outside of the channel-floodplain interface along the left and right banks to locate the most proximal LSPIV-derived depth-averaged velocity vector. I used 3 cm onto the floodplain, perpendicular to the channel centerline, to exclude velocity vectors located within the channel during the nearest neighbor search. Each point along the left and right banks was spaced at 0.4-m increments in the downstream direction. I then computed the bank unit discharge, $\boldsymbol{q}_s^B$, at each point at downstream distance, $s$, with superscripts $L$ or $R$ indicating the left or right bank, respectively. The equation for bank unit discharge was

$$\boldsymbol{q}_s^B = \boldsymbol{U}_s^B h_s^B \tag{4}$$

where $h$ is the depth of flow over the floodplain at each point. I then computed the unit exchange flow, $\widehat{\boldsymbol{q}}_s^B$ at location $(s, B)$ as the dot product of the bank unit discharge and the unit normal vector at distance $s$, and bank $B$, as

$$\widehat{\boldsymbol{q}}_s^B = \boldsymbol{q}_s^B \cdot \widehat{\boldsymbol{n}}_s^B \tag{5}$$

where $\widehat{\boldsymbol{n}}$ is the unit normal vector perpendicular to the channel centerline and oriented away from the channel such that positive unit exchange flux at the right bank would indicate flow exiting the channel, and negative unit exchange flow at the left bank would indicate flow entering the channel. This unit exchange flow can be interpreted in terms of local momentum flux patterns along the channel-floodplain interface since the unit exchange vector scales with momentum.

To investigate reach mass balance through channel-floodplain exchange flows and the influence of floodplain vegetation I then integrated the unit exchange flow over the half meander of interest, such that

$$\overline{\hat{q}^B} = \frac{1}{M/2} \int_0^{M/2} \hat{q}^B(s)\, ds \tag{6}$$

where $\overline{\hat{q}^B}$ is the half-meander-averaged unit exchange flow at the left or right bank, $M$ is the meander wavelength, $\hat{q}^B(s)$ is the unit exchange flow at downstream distance $s$. We discretized

this integral such that $ds \cong \Delta s$, where $\Delta s$ is the incremental downstream distance (0.4-m). The discretized equation can be written as

$$\overline{\hat{q}^B} = \frac{1}{M/2}\sum_{i=1}^{n} \hat{q}_i^B \Delta s \tag{7}$$

where $\overline{\hat{q}^B}$ is the reach half-meander-averaged unit exchange flow, $\frac{M}{2}$ is the streamwise length of a half meander, $n$ is the number of locations where unit exchange flow is computed through the half meander, and with index $i$.

To further investigate channel-floodplain exchange and surface-in channel flow interaction, I quantified the influence of the shear layer shown to develop at bankfull height where surface flows exchange energy with in-channel flows. Liu et al. (2016), Naghavi et al. (2022), and Shiono et al., (2009a) made observations that the horizontal shear layer is influenced by floodplain roughness and this occurs as water flows from the floodplain over the channel at a different velocity and angle compared to in-channel flows.

### 3.3 Results

At $D_r$ = 0.1, the discharge, as reported by the digital output of the in-line flow meter upstream of the flume, was the same for all three floodplain roughness scenarios (Runs, 2, 3, and 4), (See Figure 3a). At $D_r$ = 0.25, discharge was highest for the unvegetated run (Run 7) and lowest for the dense vegetation run (Run 5).

Measured sediment transport rates increased with discharge for all relative depths (Figure 2b, see discussion in Chapter 2). At bankfull depth, sediment transport reached equilibrium at 2 kg/hr. During the $D_r = 0.1$ runs, sediment transport was 5, 7, and 15 kg/hr for the bare, low-density, and high-density vegetation conditions. During the $D_r = 0.25$ runs, sediment transport was 40, 60, and 70 kg/hr for the bare, low-density, and high-density vegetation conditions. A detailed description of sediment transport measurements and bed adjustment over the course of the experiments is given in Chapter 2.

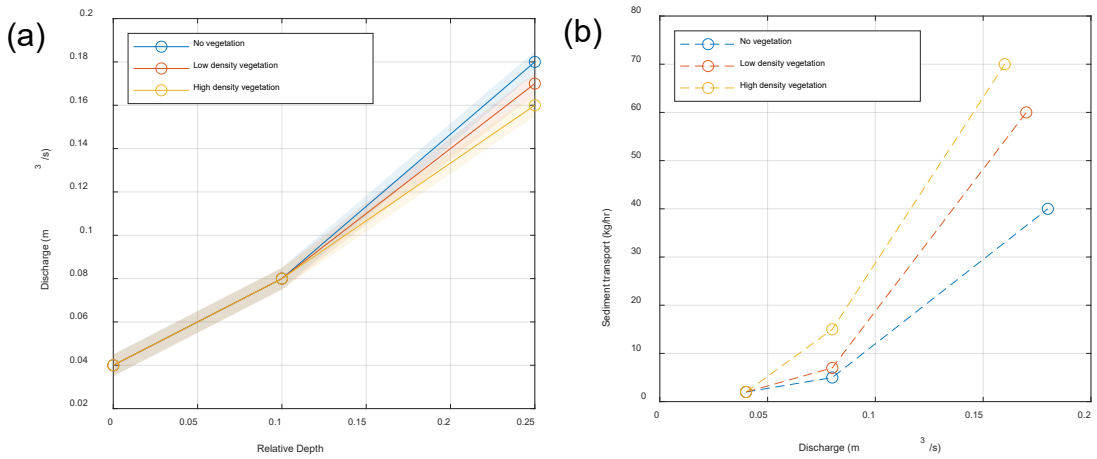


**Figure 3.2.** (a) Relative depth vs discharge. Shaded regions represent the range of flow measurement fluctuations reported in digital readout of flow gage. (b) Equilibrium sediment transport rate trend for all runs.

*3.3.1 In-channel flow field*

*3.3.1.1 Run 1*

At bankfull flow, Run 1, I observed classic meandering channel flow. The high velocity core shifted from left bank to right bank through the bend and helical flow developed with cross-stream flow oriented to the right at cross section 1 and cross-stream flow oriented to the left at cross section 10 (Figure 3.3 and Supplementary Figure A4). The secondary flow field was coherent following patterns described in the literature (Dietrich et al., 1979).

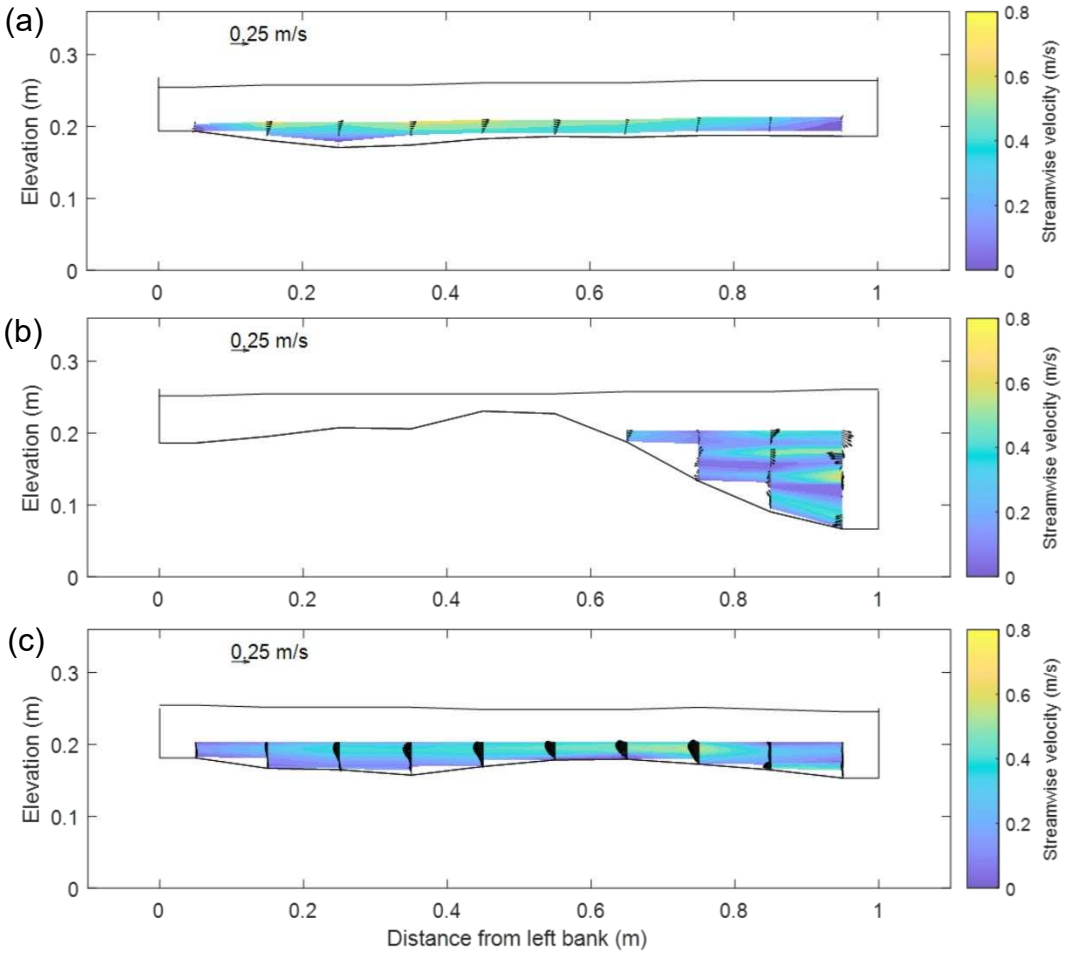


**Figure 3.3.** Flow field during Run 1, bankfull flow. (a) Cross section 1. (b) Cross section 5. (c) Cross section 10.

*3.3.1.2 Run 2*

As I increased flow to $D_r = 0.1$, with a bare floodplain (Run 2), the secondary flow structure became less coherent and the high velocity core became concentrated to a smaller area (See Figure 3.4a and 3.4c). Small secondary circular flow structures were dispersed through the velocity profile suggesting that shearing flows at bankfull height induced small helical cells, but weakened the larger secondary flow cell that often extends through the water column at the pool at bankfull depth. See Suplemental Figure A2 for flow field at all 10 cross sections during Run 2.

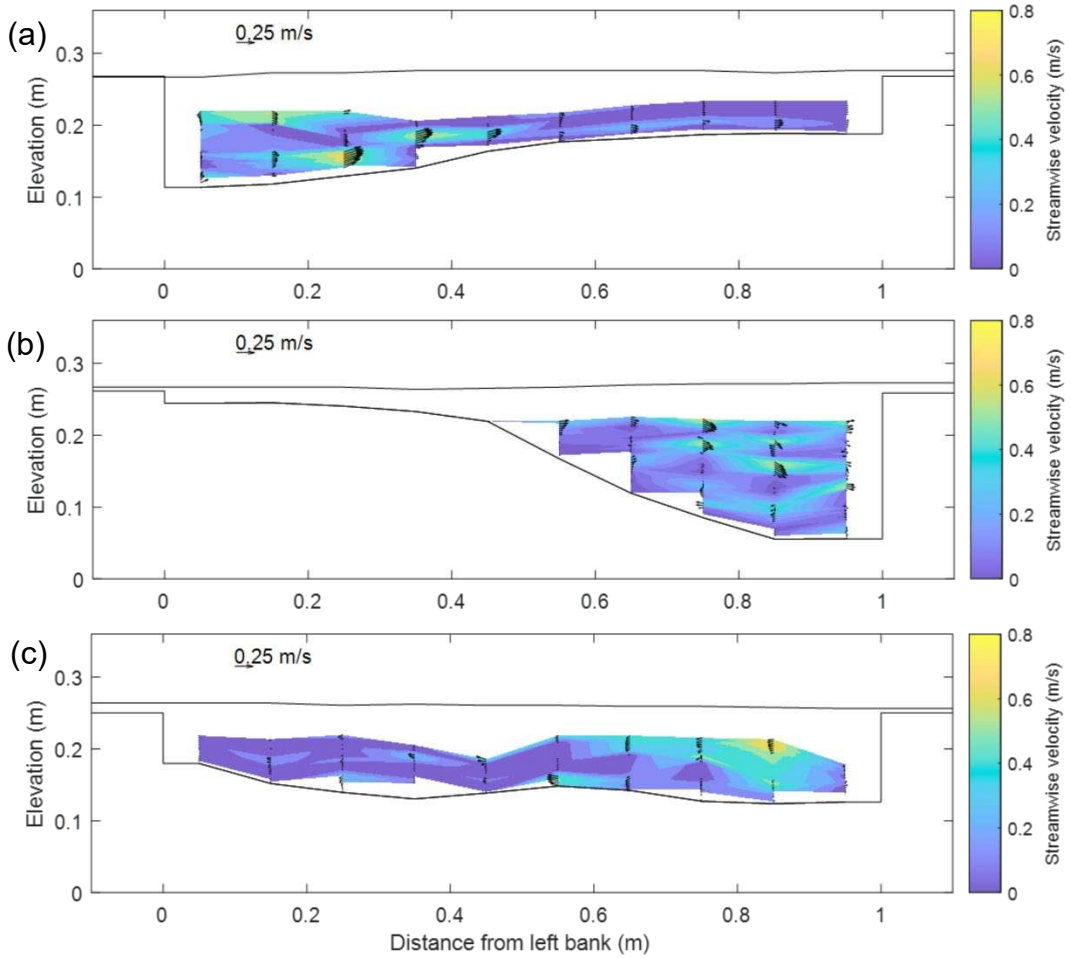


**Figure 3.4.** Run 2, $D_r = 0.1$, bare floodplain. (a) Cross section 1. (b) Cross section 5. (c) Cross section 10.

*3.3.1.3 Run 3*

During Run 3, as emergent stems were placed on the floodplain at low density and $D_r = 0.1$, the secondary flow structures became slightly more apparent and high velocity cores slightly more concentrated (See Figure 3.5). I observed two cores of high streamwise velocity from cross-section 6 through 10, one near the channel centerline, and one near the thalweg at the right bank through the pool (See Figure 3.5 and Supplemental Figure A3).

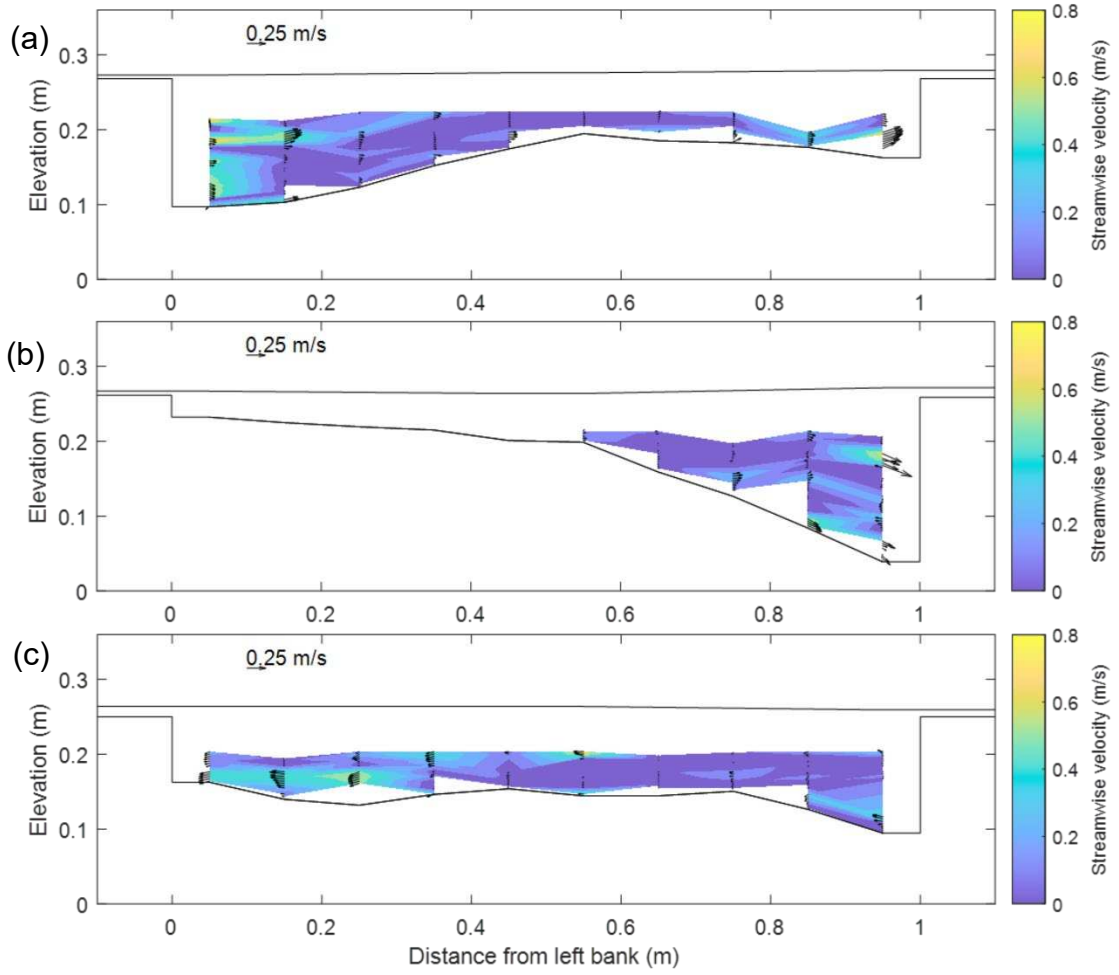


**Figure 3.5**. Run 3. $D_r = 0.1$, low-density vegetation. (a) Cross section 1. (b) Cross section 5. (c) Cross section 10.

*3.3.1.4 Run 4*

At high floodplain vegetation density (Run 4, $D_r = 0.1$), from cross-sections 1 through 3, helical flow enhanced the formation of a pool with an adjacent steep transverse bar slope (Figure 3.6). Farther downstream, a layer of low streamwise velocity appeared spanning roughly the width of the channel and persisted through the bend (See Supplemental Figure A4). Lateral and vertical velocity measurements were also low in this low velocity layer. Near bed velocities through the pool followed a pattern similar to those during the bankfull run strongly oriented away from the right bank toward the bar (Figure 3.6c and 3.6d).

*3.3.1.5 Run 5*

During Run 5 ($D_r = 0.25$, high vegetation density) the secondary flow field is coherent through all 10 cross sections following a distinctly helical pattern (Figure 3.7). The high velocity streamwise core follows a pattern similar to that characteristic of bankfull flow run shifting from right to left bank through the bend with a secondary circular flow cell visible in the pool (Figure 3.7c). The flow field is much more organized suggesting that the helical flow pattern retains strength and that the low velocity flow coming off the floodplain has less influence than at low vegetation density and bare floodplain conditions (See Figure 3.7).

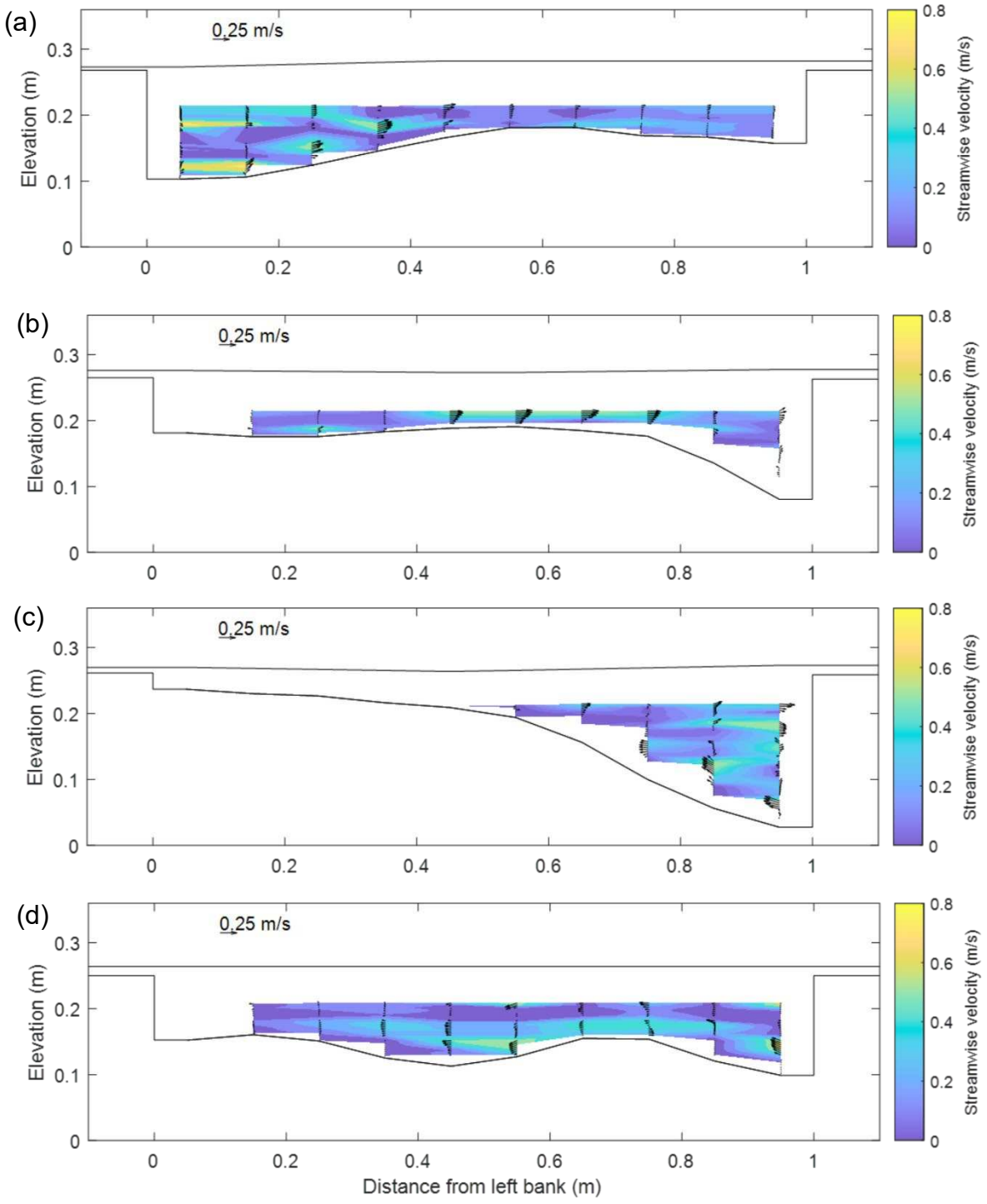


**Figure 3.6**. Run 4, $D_r = 0.1$, high-density vegetation. (a) Cross section 1. (b) Cross section 3. (c) Cross section 5. (d) Cross section 10.

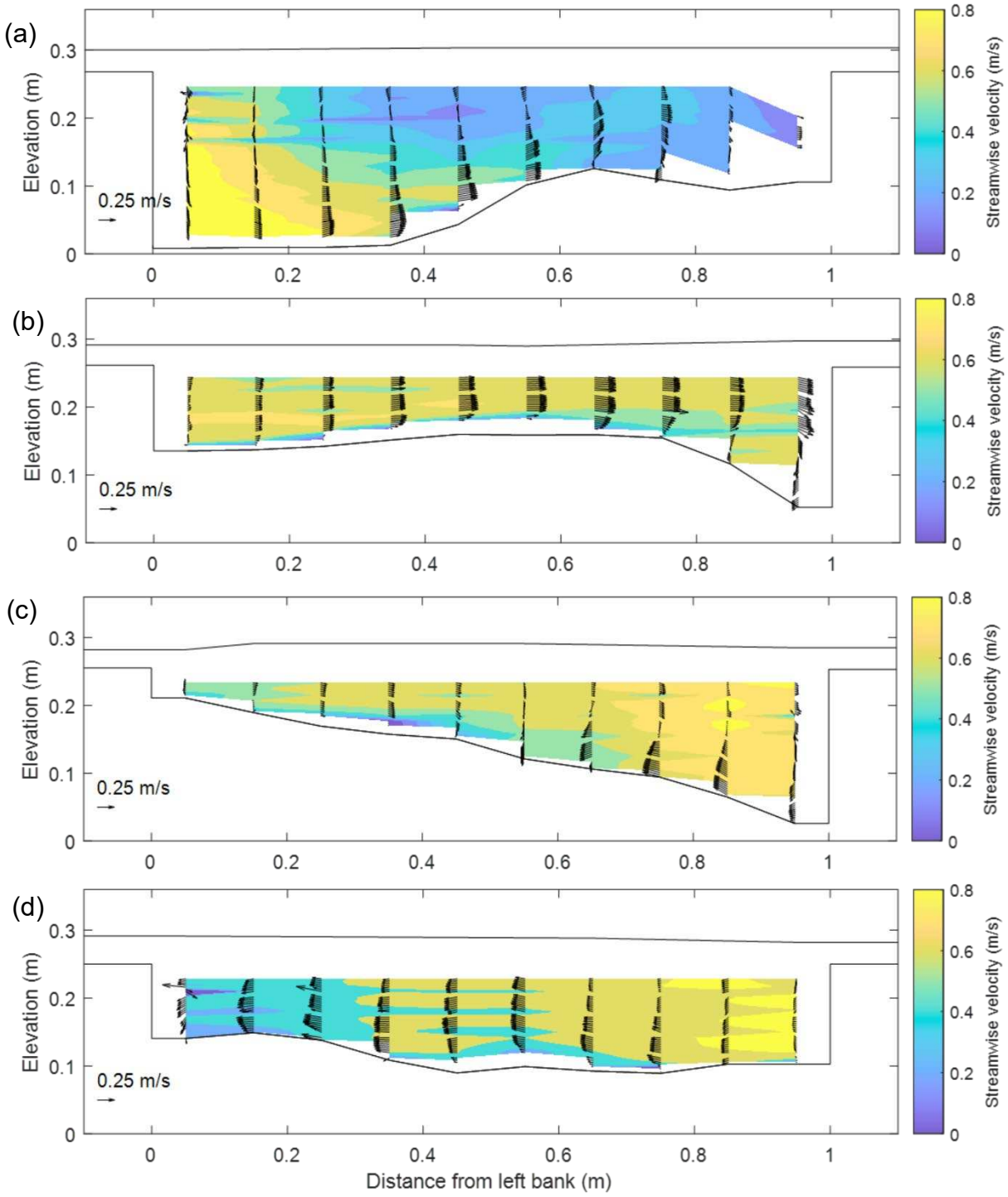


**Figure 3.7**. Run 5, $D_r = 0.25$, high-density vegetation. (a) Cross section 1. (b) Cross section 5. (c) Cross section 8. (d) Cross section 10.

*3.3.1.6 Run 6*

During Run 6 ($D_r = 0.25$, low-density vegetation), a visible horizontal shear layer extends into the channel resulting in low velocities in cross sections 3 and 5 (Figure 3.8 and S6). In the crossover region, floodplain flow reentering the channel appeared to enhance the clockwise-oriented secondary flow cell (Figure 3.8c). Similar to the $D_r = 0.1$ run with low-density vegetation, two distinct high streamwise velocity cores and multiple large secondary flow cells were present at cross sections 7 and 8 (See Figures A4 and A6). By cross sections 9 and 10, the surface velocity flowing off the floodplain over the channel transfers energy to the in-channel flow field dissipating the secondary flow cell which loses its coherent structure becoming quite irregular at cross section 10 (Figure 3.8d and A6).

*3.3.1.7 Run 7*

During Run 7 ($D_r = 0.25$, bare floodplain), a layer of low velocity is present across the width of the channel from cross section 2 through 5 (See Figure 3.9b and A7). As floodplain flows enter the channel near the left bank, a circular flow cell develops extending from cross sections 1 to 3 (See Figure A7). At cross section 3, high cross-channel velocity is present near bankfull height, likely result of the high surface velocities entering the channel from the floodplain. A circular current spanning the depth of the channel develops through the pool at the right bank but becomes less coherent through cross-sections 9 and 10 (See Figure 3.9d and S9). In cross-sections where the secondary current is present, high velocity cross-stream surface flows align with the classic meandering helical flow pattern, but near the bend apex (XS 9 & 10), the surface flow coming off the floodplain shears across the surface diffusing the flow pattern and produces a much more irregular distribution of streamwise, lateral, and vertical velocity components by cross section 10 (see Figure 3.9d).

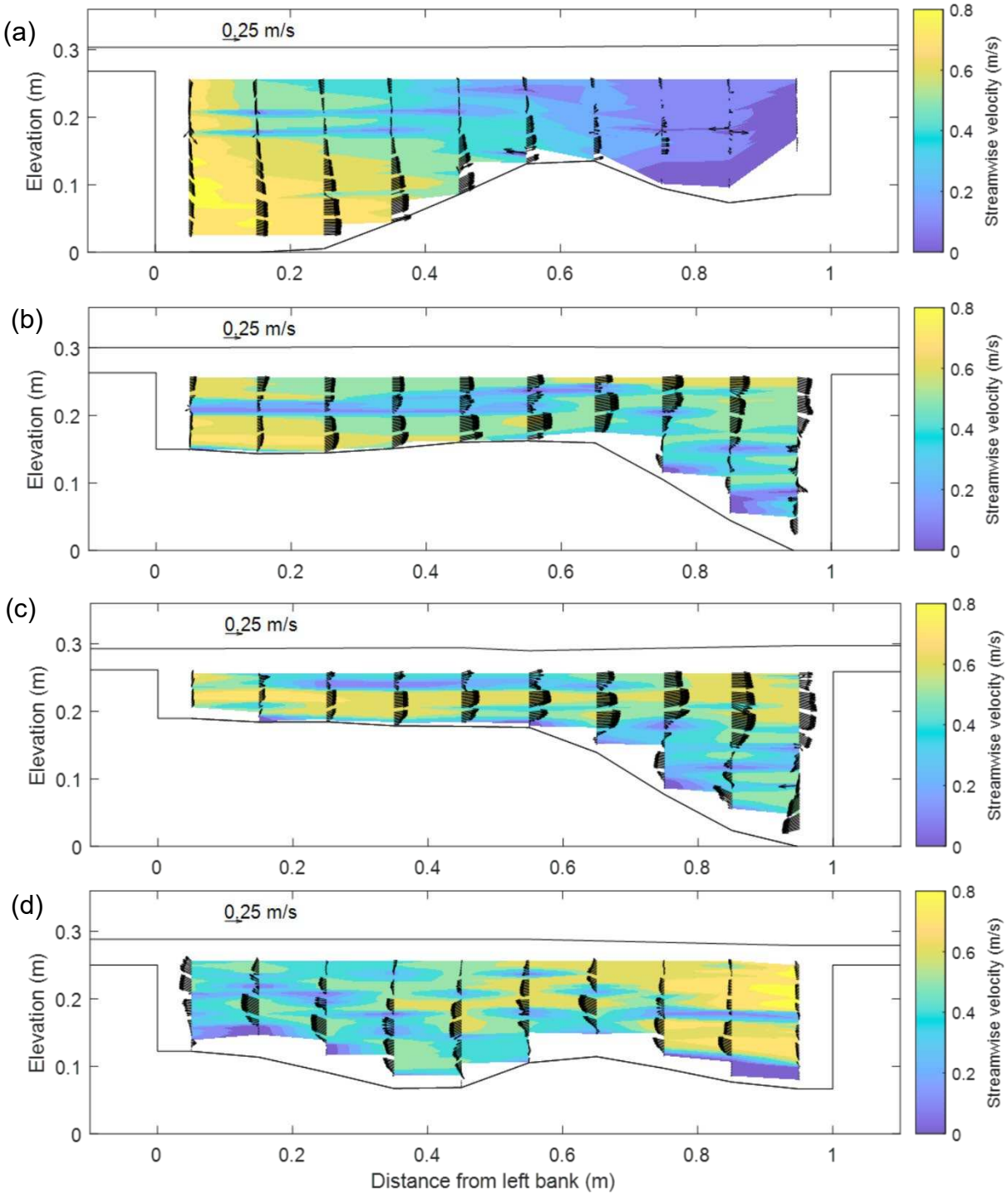


**Figure 3.8**. Run 6, $D_r = 0.25$, low-density vegetation. (a) Cross section 1. (b) Cross section 4. (c) Cross section 5. (d) Cross section 10.

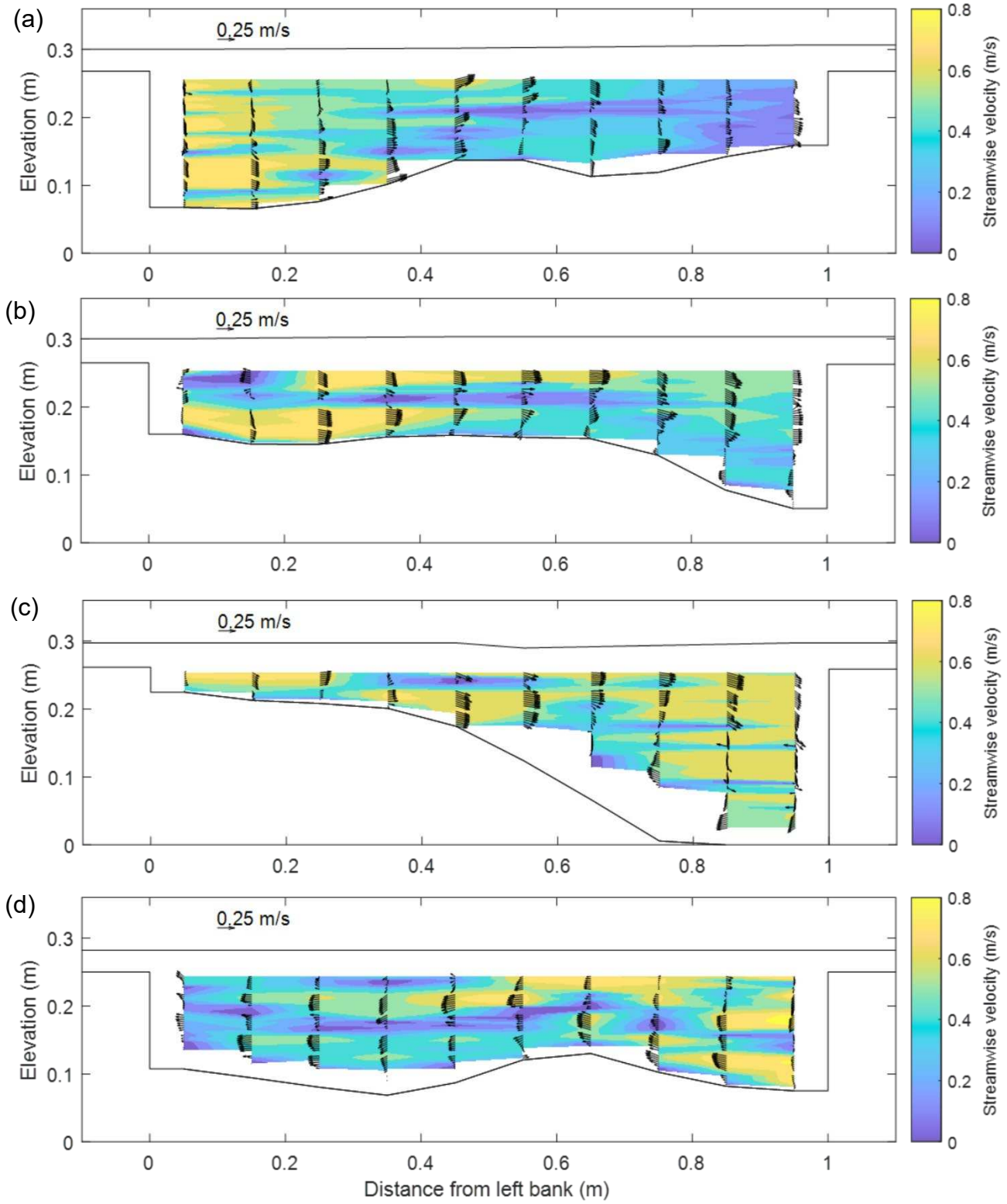


**Figure 3.9**. Run 7, $D_r = 0.25$, bare floodplain. (a) Cross section 1. (b) Cross section 3. (c) Cross section 5. (d) Cross section 10.

*3.3.2 Shear stress*

I applied two methods to estimate shear stress within the channel and investigate the influence of the highly three-dimensional flow field in meandering compound channels on shear stress estimates. I used the Manning-Strickler approximation with local depth-averaged velocities and an average of computed shear stress values within the logarithmic velocity region near the bed using the law of the wall. In general, the Manning-Strickler approximation for shear stress using depth-averaged velocities estimated lower boundary shear stress than using the law of the wall, although the spatial distribution of regions of high shear stress was similar for calculation methods using both depth-averaged and near-bed velocity measurements (See Figure 3.10). For the $D_r = 0.1$ runs, the region of high shear stress followed the thalweg shifting from the pool at the left bank to the pool at the right bank. However, for the $D_r = 0.25$ runs, a region of high shear stress developed near the left bank in the crossover region where water flows off the floodplain into the channel.

For all three floodplain cover scenarios, this zone of high shear stress in the crossover region exceeded shear stress within the pools. During Run 7, with a bare floodplain and high floodplain velocities, the shear stress near the left bank was near zero, however, for low- and high-density vegetation (Run 6 and 5), shear stress near the left bank increased. This may be due to turbulent flow structures which result from a strong vertical shear layer where low velocity flow through vegetated floodplains encounters high-velocity surface flows within the channel.

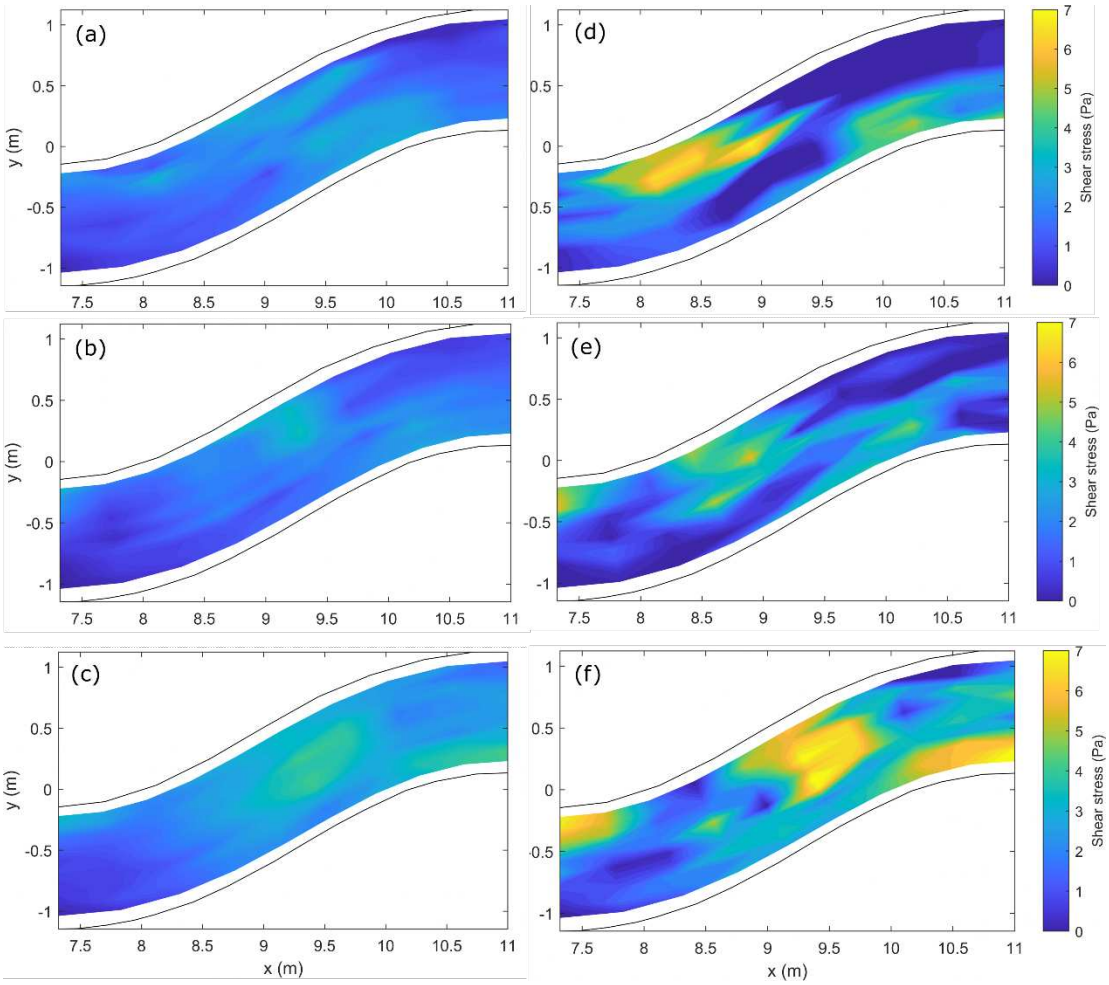


**Figure 3.10.** Shear stress distribution estimates for $D_r$ = 0.25 runs calculated with the Manning-Strickler approximation (a-c) and law of the wall (d-f) to measure the influence of 3D flow structure. (a) Bare floodplain. (b) Low density vegetation (c) High density vegetation. (d) Bare floodplain. I Low density vegetation. (f) Figh density vegetation.

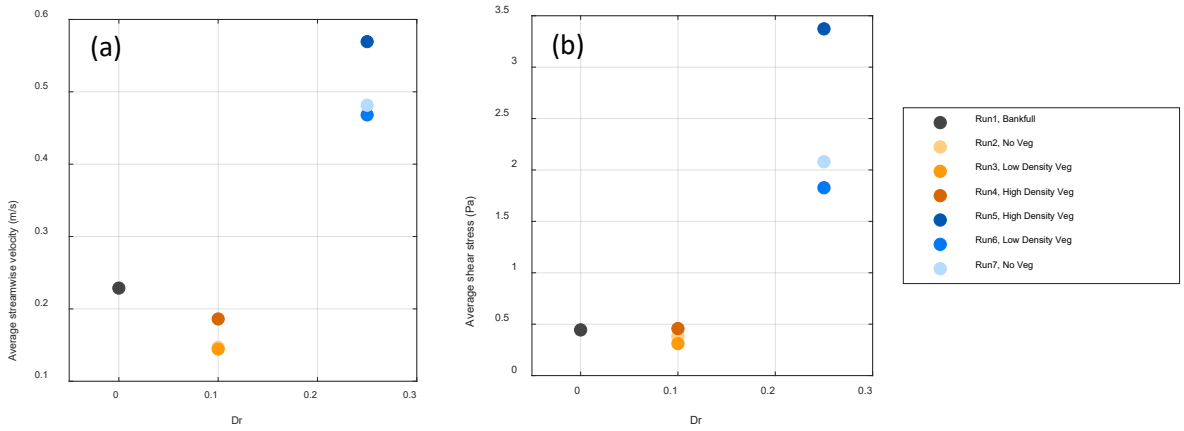


**Figure 3.11.** Reach-averaged (a) in-channel streamwise velocity and (b) shear stress with averages of single point estimates near the bed.

*3.3.3 Surface flow field*

As described in Section 2.3, I measured surface velocity both in the channel and on the floodplain through the half meander of interest using LSPIV. During all three runs at $D_r = 0.1$ (Figure 3.12a-c), the highest velocities across the surface occurred within the channel.

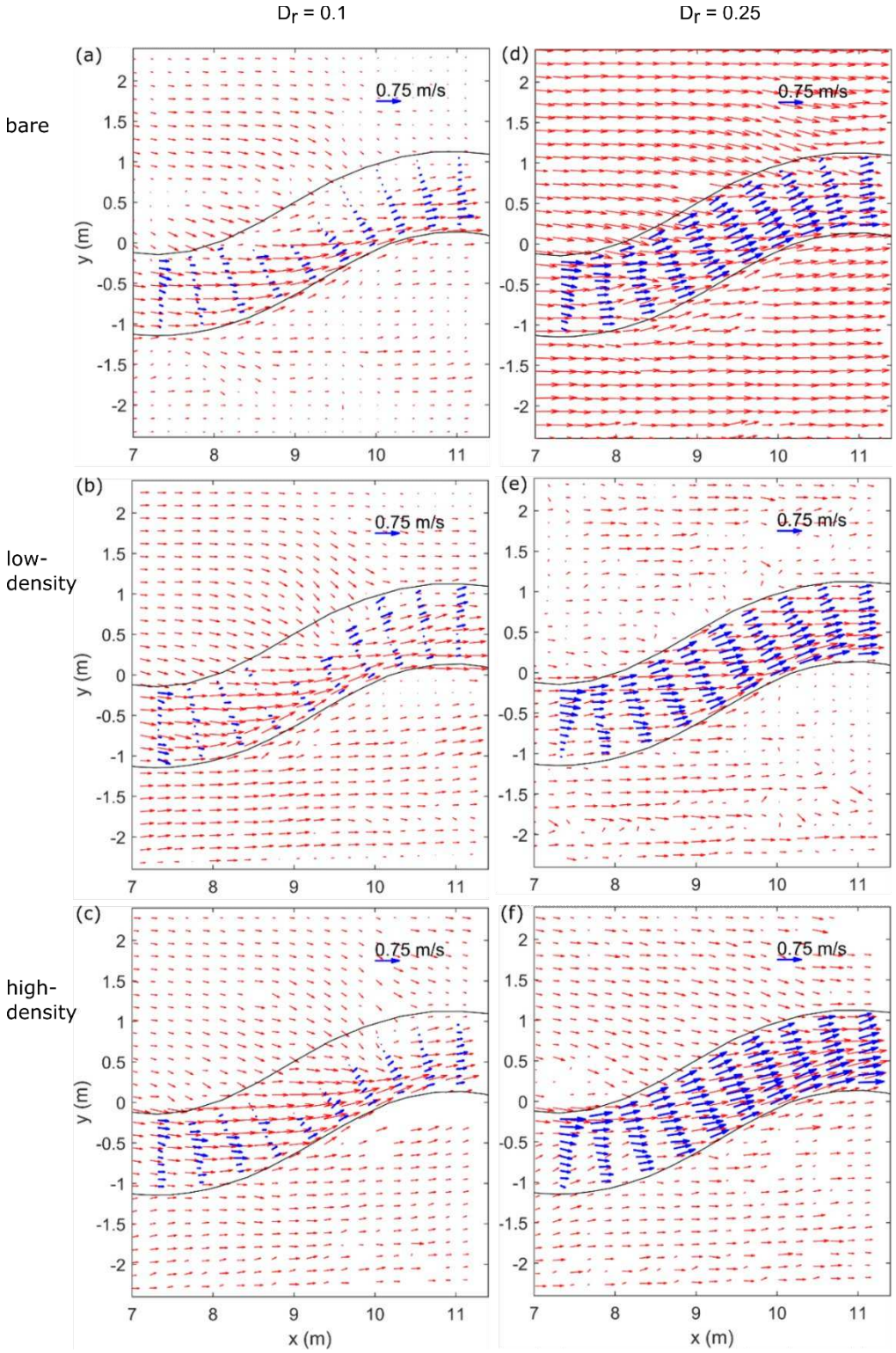


**Figure 3.12.** Surface velocity (red vectors) and depth-averaged in channel velocity (blue vectors) for $D_r = 0.1$ (a-c) and $D_r = 0.25$ (d-f). (a) Run 2. (b) Run 3. (c) Run 4. (d) Run 7. I Run 6. (f) Run 5.

Average surface velocities over the floodplain were lower than in-channel velocities for Runs 2, 3, and 4 regardless of floodplain cover. With a bare floodplain (Run 2) the average surface velocity measured within the channel was 0.37 m/s. With low density vegetation (Run 3) the average surface velocity measured within the channel increased to 0.43 m/s, and at high vegetation density (Run 4) the average velocity within the channel was 0.43 m/s. The higher velocities measured within the channel suggest that conveyance was higher within the channel with vegetated floodplains. It should be noted that although there appear to be patches of low surface velocity in the floodplain in Figure 3.12a and 3.12f, surface velocity was generally uniform across the floodplain but poorly estimated using LSPIV because of camera orientation and glare on the water surface when images were captured.

During Run 7, (bare floodplain, $D_r = 0.25$) surface velocities were high both in the channel and over the floodplain. Floodplain and in-channel surface velocities were very similar at 0.63 and 0.61 m/s during Run 7. The average surface velocity across the densely vegetated floodplain (Run 5) was 0.23 m/s, significantly lower than average surface velocity within the channel of 0.47 m/s. A similar difference in surface velocities over the floodplain and in the channel was seen for the low-density vegetation case (Run 6) at 0.19 m/s versus 0.45 m/s.

Increasing floodplain vegetation density at both $D_r = 0.1$ and $D_r = 0.25$ produced a steering effect of flows within the channel that I observed visually and quantified by measuring the difference of flow angle at the surface and below bankfull height (Figure 3.13). This steering effect was not as clear at $D_r$ = 0.1, but with dense vegetation, the surface flow closely follows the orientation of in-channel flow and the angle difference is close to zero through the cross over region (s = 8.5 to s = 11).

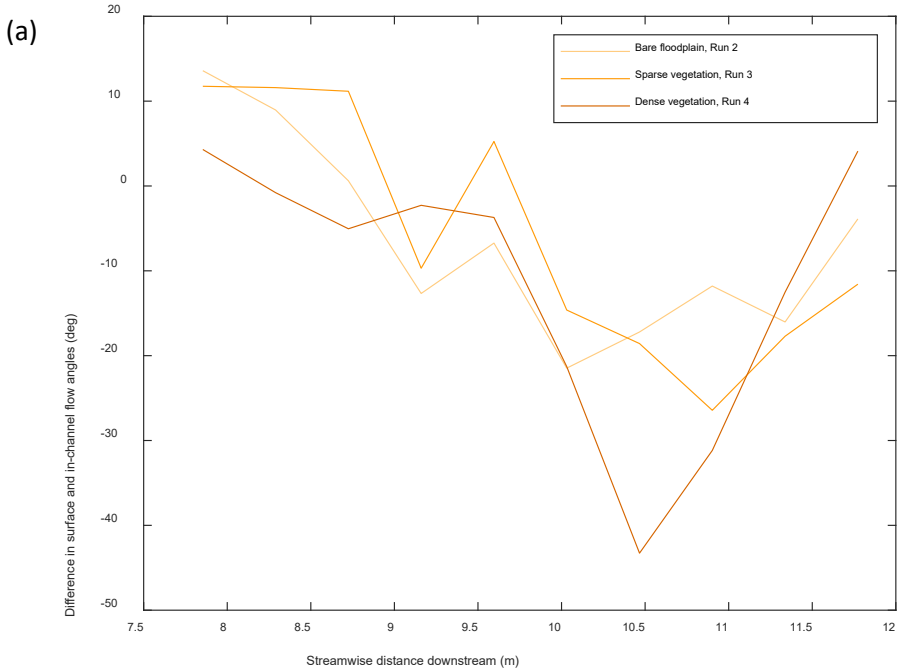


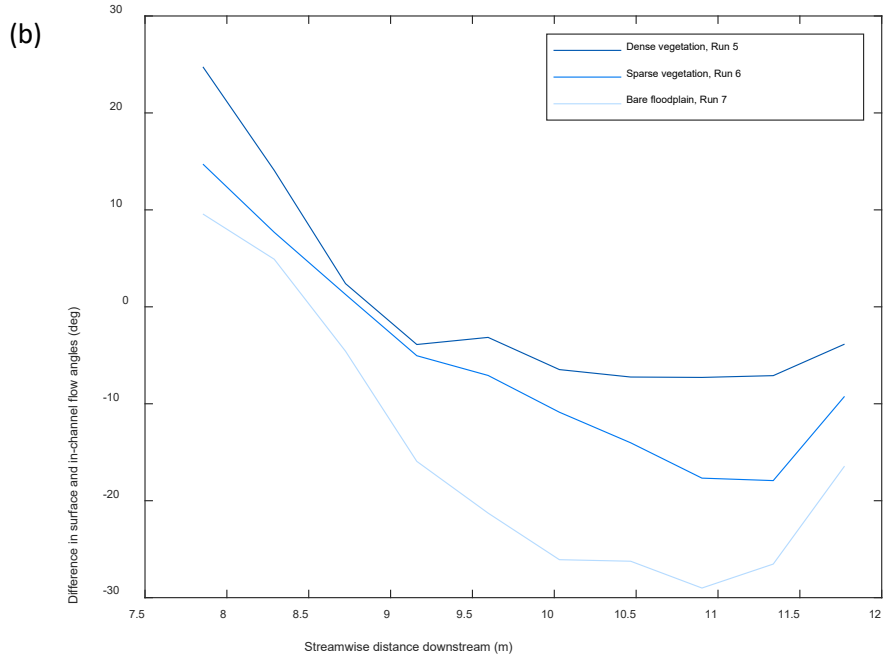


**Figure 3.13.** Flow angle difference between surface and in-channel through half meander of vs streamwise distance, or distance along the channel centerline. (a) $Dr = 0.1$ (b) $Dr = 0.25$.

*3.3.4 Channel-floodplain exchange flow*

I measured the hydrodynamic interaction of in-channel and floodplain flows by computing unit exchange flow across the left and right banks. A graphical representation of this exchange flow computation and results is depicted in Figure 3.14. Generally, flux across the left bank was greater than at the right bank in this experiment due to the meander direction. I observed that at low relative depth, $D_r$ = 0.1, the unit exchange flow across the left and right banks was similar for all floodplain vegetation conditions, all within $0.0005$ m$^2$/s (See Figure 3.14). In Figure 3.14, positive unit exchange flow represents flux out of the channel, thus negative values were measured for the right bank as flow exits the channel onto the floodplain.

At $D_r$ = 0.25, unit exchange flow increased in magnitude for all vegetation conditions and was significantly greater for the bare floodplain scenario (Run 7), reflecting the high velocities and exchange flows entering and exiting the channel throughout the bend. With high density vegetation (Run 5), unit exchange flow across the left bank was $4.3 \times 10^{-3}$ m$^2$/s greater in magnitude than the low density vegetation at $2.5 \times 10^{-3}$ m$^2$/s, however, this was reversed at the right bank with low density vegetation having a slightly higher value, $1.6 \times 10^{-3}$ m$^2$/s, than the high density vegetation run at $1.5 \times 10^{-3}$ m$^2$/s.

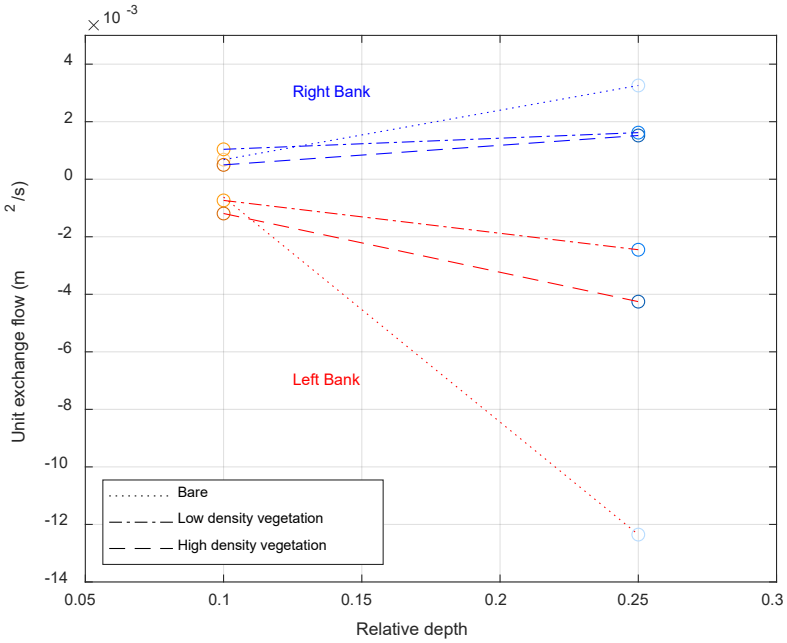


**Figure 3.14.** Channel-floodplain exchange flow. Negative values indicate flux into the channel. Positive values indicate flux out of the channel. The circles' color scheme matches Figures 3.8 and 3.9. Orange circles represent the $D_r = 0.1$ runs, and the blue circles represent the $D_r = 0.25$ runs. Exchange flow at the left bank is larger likely due to small fluctuations in the floodplain surface.

## 3.4 Discussion

### *3.4.1 In-channel flow field*

I discuss three primary mechanisms which are responsible for large-scale 3D flow structures observed in the channel, each of which are highly dependent on relative flow depth and vegetation density: the vertical shallow mixing layer at bankfull height along the channel-floodplain interface (red faces in Figure 3.15, labeled (1)), the horizontal shallow mixing layer at bankfull height over the channel (yellow faces in Figure 3.15, labeled (2)), and helical flow structure induced by channel meanders and bar-pool topography (blue lines in Figure 3.15, labeled (3)).

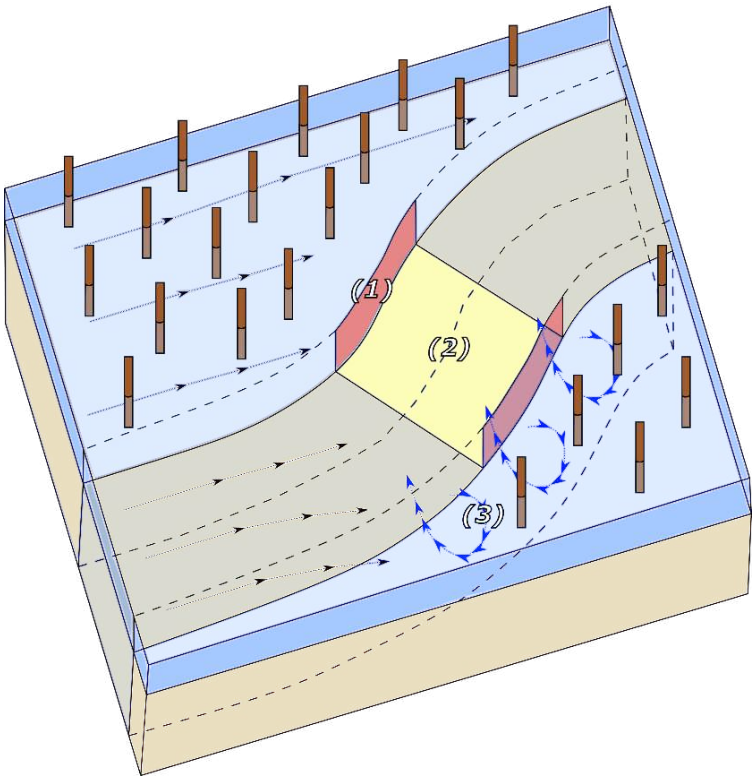


**Figure 3.15.** Schematic displaying regions of interest with respect to interactions of channel and floodplain flow influenced heavily by floodplain vegetation. (1) Vertical shallow mixing layer at channel-floodplain interface. (2) Horizontal mixing layer at bankfull height. (3) Helical flow within the channel through the meander bend.

At $D_r$ = 0.1, the helical flow field characteristic of meandering channels was dampened with secondary circular velocities less coherent, as a result of interactions with flows entering and exiting the channel (See Figures A2, A3, A4). This was apparent for the bare, low density, and high-density floodplain vegetation scenarios (Run 2, 3, and 4).

During the high-vegetation-density case at high relative depth, the helical flow structure remains intact through the bend enhanced by the steering of flows by the dense vegetation. By flow steering, I suggest that flows within the channel remain in the channel, with greater relative in-channel conveyance. The width of the mixing layer induced by the vertical shear interface where the channel meets the floodplain (See Figure 3.15, Element 1) is likely influenced by Reynolds stresses due to the sharp velocity gradient at the channel-floodplain interface similar to observations made by Dupuis et al., (2017b, 2017a) in a straight compound channel with vegetated floodplains. The relative influence of the vertical shear layer on in-channel flow structure likely increases with vegetation density which is supported by the increasingly sharp gradient in floodplain-vs-channel surface flow magnitude and orientation with vegetation density (i.e. Figure 3.12f). This vertical shear layer is likely weak during the unvegetated scenario (see Figure 3.12d) because, because floodplain and in-channel surface velocity vectors share similar orientation. However, it appears that this vertical shear layer does not dampen the helical flow that was most coherent with high-density vegetation, and its influence on general flow patterns may be small relative to the horizontal shear layer at bankfull height.

Mixing layer turbulent diffusion at bankfull height (Figure 3.15, Element 2) appears to be responsible for the decreased coherence of secondary flow structure for unvegetated floodplains. This diffusion largely occurs along the cross over region (XS 3-7) for runs 2-7. As the channel

centerline becomes aligned with the downvalley direction, lateral and vertical velocities decrease, and the flow field becomes largely composed of small, weak turbulent flow structures until the bulk of flow approaches the outside bank and centrifugal acceleration drives flow down and inward where larger time-averaged coherent structures are once again visible. The strength and width of the shallow mixing layer at bankfull height is largely dependent on relative depth, and depth of flow within the channel due to turbulence generated near the bed. I suspect that for low sinuosity channels such as this experimental setup, as $D_r$ exceeds 0.25, the strong turbulent diffusion due to the mixing layer at bankfull height will likely overpower meandering helical flow currents and bar-pool relief will decline.

*3.4.2 Shear stress*

In Chapter 2, I discuss the difference in sediment rating curve in these experimental observations compared with observations made by others in meandering compound flume experiments (Karamisheva et al., 2006; Lyness et al., 2001; Shiono et al., 2009a; Wormleaton et al., 2004) and suggest that planform strongly influences sediment transport capacity. In this chapter, I analyze the flow field to further investigate the monotonic increase in sediment transport above bankfull flow. Of particular interest are the observations of the flow field and calculated boundary shear stress during Runs 2, 3, and 4. Spatially distributed shear stress averaged over the half meander was similar at $D_r = 0.1$ for all floodplain scenarios compared to the bankfull depth run, average shear stress during Run 4, high vegetation density, was greater than the average shear stress at bankfull, Run 1, and average shear stress during Run 2 and 3, was slightly lower.

These observations support the hypothesis made in Chapter 2 that in a low sinuosity flume at overbank depths, transport capacity of sand and gravel will be greater than at bankfull flow.

Although it is apparent that at $D_r = 0.1$ the coherent three-dimensional flow structure is altered due to surface flows interacting with the in-channel helical flow field, for low sinuosity channels, that energy loss is minimized as the surface flow field is more closely aligned with the channel centerline than in high sinuosity channels. At $D_r = 0.25$, sediment transport was much higher than bankfull for all three floodplain cover conditions. I recommend further investigation into the character of the horizontal shear layer which develops at bankfull height in meandering compound channels with vegetated floodplains with varied sinuosity and suggest that there may be a threshold sinuosity where at low $D_r$ transport capacity shifts from less than bankfull to greater than bankfull.

### *3.4.3 Surface flow field*

At $D_r = 0.1$, flow velocity across the floodplain was low for each vegetation configuration. Drag force exerted by vegetation has been shown to scale with the square of the approach velocity and frontal area (Albayrak et al., 2014; Diehl et al., 2017; Nepf, 1999; Vargas-Luna et al., 2015, 2016; Vogel, 1989), both low at low relative depths. Because of this, channel-floodplain exchange flow was low for all vegetation configurations at low relative depth. However, as flow depth increased, the difference in surface velocities was much more strongly driven by floodplain vegetation density as the drag force exerted by vegetation was significantly greater for high the high-density vegetation scenario. Channel floodplain exchange flux was highest for the bare floodplain scenario and surface flows remained oriented in the downvalley direction even over the channel. The high-vegetation-density scenario attenuated channel-floodplain exchange flow as energy was dissipated by flow passing through the floodplain.

### *3.4.4 Floodplain exchange flow and relevance to natural channels*

Although for decades it has been generally understood that channel-floodplain connectivity and complex hydrodynamic conditions present during floods support critical riparian processes, recent studies have emphasized the lack of research quantifying the physical effect of biological elements such as large woody vegetation on in-channel flow field and thus bed altering shear stress. Some research has studied and predicted the response in vegetation succession to varied flow regimes (i.e. Benjankar et al., 2011), others have developed analytical models to predict channel response to increased hydraulic roughness and mechanical stabilization of floodplain vegetation (i.e., Crosato & Saleh, 2011); however, I am not aware of any studies investigating the three-dimensional hydrodynamic mechanisms responsible for channel-altering stresses and flux attenuation in response to varied floodplain vegetation density and directly linking those mechanisms to riverscape sustaining hydrologic processes. I show that high density floodplain vegetation may enhance or promote conditions that maintain riparian habitat and attenuate floodplain fluxes.

At the reach scale, floodplain vegetation attenuates channel-floodplain fluxes by decreasing floodplain flow velocity. Within the active channel, the bed can morphodynamically respond to high conveyance and shear stress due to flow steering through the development of complex bedform topography such as bar-pool relief and increased hydraulic roughness. An unvegetated floodplain exposed to high stresses and high velocities has low hydraulic roughness poorly attenuating flood waves. This may increase risk of damage to downstream communities.

Floodplain vegetation plays an important role in enhancing aquatic habitat. The hydrodynamic interaction of floodplain vegetation and floods also enhances aquatic habitat as secondary currents likely contribute to cleaning gravels of fine particles and organic material exposing gravel beds suitable in riffles and pools for spawning salmonids (Tonina & Buffington,

2007), enhancing habitat for macroinvertebrates (Garcia et al., 2012). High vegetation density essentially has the capability to magnify the work done by low overbank flows required to maintain aquatic habitat. Although I did not specifically quantify lateral shear stress at the left and right banks, the enhanced secondary currents, and high velocity core exert strong channel altering forces necessary to cause channel migration promoting diversity in geomorphic features within a channel, a feature generally acknowledged as beneficial to riparian organisms (Poff et al., 1997; Resh et al., 1988; Sparks et al., 1990). A natural hydrologic regime, with regularly recurring floods maintains and sustains important habitat in pool-riffle habitat maintenance (Duffin et al., 2023).

### 3.5 Conclusion

The presence of dense floodplain vegetation alters meandering compound channel flow by attenuating channel-floodplain exchange flow, retarding floodplain flow velocity, and steering flow within the channel such that the three-dimensional helical flow field becomes enhanced during floods at high relative depth. The size and persistence of coherent turbulent flow structures within the channel are enhanced or diminished as a result of a strong horizontal shear layer at bankfull height and a vertical shear layer at the channel-floodplain interface. These hydrodynamic characteristics may be beneficial to humans living near rivers as the destructive energy of flood waves is attenuated and to aquatic organisms as in-stream hydraulic and geomorphic conditions maintain critical in-stream habitat. I come to this conclusion through analysis of observations made in a meandering compound flume experiment where flow depth and rigid-emergent floodplain vegetation density were varied over the course of seven experimental runs. In comparing these observations with other meandering compound flume experiments I suggest that planform or meander sinuosity may also produce hydrodynamic and

geomorphic feedbacks as floodplain vegetation density is varied and recommend further investigation into the influence of planform and vegetation density on meandering compound channel hydrodynamics.

These results also show that meandering compound channel flow is highly three-dimensional. The presence and strength of secondary currents within the channel is significantly influenced by floodplain vegetation density. Further work to incorporate the knowledge gained through this analysis by developing relationships that can be applied to 2D hydraulic models would be beneficial in river engineering analysis and design. For river and land use managers hoping to incorporate the influence of biological drivers (such as rigid vegetation) in river planning, additional tools, and studies such as this may provide support to approach challenges.

### 3.6 References

Aberle, J., & Järvelä, J. (2013). Flow resistance of emergent rigid and flexible floodplain vegetation. *Journal of Hydraulic Research*, *51*(1), 33–45. https://doi.org/10.1080/00221686.2012.754795

Albayrak, I., Nikora, V., Miler, O., & O'Hare, M. T. (2014). Flow–plant interactions at leaf, stem and shoot scales: drag, turbulence, and biomechanics. *Aquatic Sciences*, *76*(2), 269–294. https://doi.org/10.1007/s00027-013-0335-2

Beechie, T. J., Liermann, M., Pollock, M. M., Baker, S., & Davies, J. (2006). Channel pattern and river-floodplain dynamics in forested mountain river systems. *Geomorphology*, *78*(1), 124–141. https://doi.org/10.1016/j.geomorph.2006.01.030

Benjankar, R., Egger, G., Jorde, K., Goodwin, P., & Glenn, N. F. (2011). Dynamic floodplain vegetation model development for the Kootenai River, USA. *Journal of Environmental Management*, *92*(12), 3058–3070. https://doi.org/10.1016/j.jenvman.2011.07.017

Benjankar, R., Jorde, K., Yager, E. M., Egger, G., Goodwin, P., & Glenn, N. F. (2012). The impact of river modification and dam operation on floodplain vegetation succession trends in the Kootenai River, USA. *Ecological Engineering*, *46*, 88–97.

Beschta, R. L. (1997). Riparian shade and stream temperature; an alternative perspective. *Rangelands Archives*, *19*(2), 25–28.

Box, W., Järvelä, J., & Västilä, K. (2021). Flow resistance of floodplain vegetation mixtures for modelling river flows. *Journal of Hydrology*, *601*, 126593. https://doi.org/10.1016/j.jhydrol.2021.126593

Box, W., Järvelä, J., & Västilä, K. (2022). New formulas addressing flow resistance of floodplain vegetation from emergent to submerged conditions. *International Journal of River Basin Management*, 1–17.

Bywater-Reyes, S., Wilcox, A. C., & Diehl, R. M. (2017). Multiscale influence of woody riparian vegetation on fluvial topography quantified with ground-based and airborne lidar. *Journal of Geophysical Research: Earth Surface*, *122*(6), 1218–1235. https://doi.org/10.1002/2016JF004058

Bywater-Reyes, S., Diehl, R. M., & Wilcox, A. C. (2018). The influence of a vegetated bar on channel-bend flow dynamics. *Earth Surface Dynamics*, *6*(2), 487–503. https://doi.org/10.5194/esurf-6-487-2018

Bywater-Reyes, S., Diehl, R. M., Wilcox, A. C., Stella, J. C., & Kui, L. (2022). A Green New Balance: Interactions among riparian vegetation plant traits and morphodynamics in alluvial rivers. *Earth Surface Processes and Landforms*, *47*(10), 2410–2436. https://doi.org/10.1002/esp.5385

Camporeale, C., Perucca, E., Ridolfi, L., & Gurnell, A. (2013). Modeling the interactions between river morphodynamics and riparian vegetation. *Reviews of Geophysics*, *51*(3), 379–414.

Chan, T. L. (2003, January 1). *A study of sediment transport in two-stage meandering channel* (thesis). Loughborough University. Retrieved from /articles/thesis/A_study_of_sediment_transport_in_two-stage_meandering_channel/9454535/1

Crosato, A., & Saleh, M. S. (2011). Numerical study on the effects of floodplain vegetation on river planform style. *Earth Surface Processes and Landforms*, *36*(6), 711–720. https://doi.org/10.1002/esp.2088

Czuba, J. A., David, S. R., Edmonds, D. A., & Ward, A. S. (2019). Dynamics of Surface-Water Connectivity in a Low-Gradient Meandering River Floodplain. *Water Resources Research*, *55*(3), 1849–1870. https://doi.org/10.1029/2018WR023527

Diehl, R. M., Merritt, D. M., Wilcox, A. C., & Scott, M. L. (2017). Applying Functional Traits to Ecogeomorphic Processes in Riparian Ecosystems. *BioScience*, *67*(8), 729–743. https://doi.org/10.1093/biosci/bix080

Dietrich, W. E., & Whiting, P. (1989). Boundary shear stress and sediment transport in river meanders of sand and gravel. *Water Resources Monograph*, 1–50. https://doi.org/10.1029/wm012p0001

Dietrich, W. E., Smith, J. D., & Dunne, T. (1979). Flow and Sediment Transport in a Sand Bedded Meander. *J. Geol.*, *87*(3), 305–315. https://doi.org/10.1086/628419

Duffin, J., Yager, E., Buffington, J. M., Benjankar, R., Borden, C., & Tonina, D. (2023). Impact of flow regulation on stream morphology and habitat quality distribution. *Science of The Total Environment*, 163016. https://doi.org/10.1016/j.scitotenv.2023.163016

Dupuis, V., Proust, S., Berni, C., & Paquier, A. (2017a). Compound channel flow with a longitudinal transition in hydraulic roughness over the floodplains. *Environmental Fluid Mechanics*, *17*(5), 903–928. https://doi.org/10.1007/s10652-017-9525-0

Dupuis, V., Proust, S., Berni, C., & Paquier, A. (2017b). Mixing layer development in compound channel flows with submerged and emergent rigid vegetation over the floodplains. *Experiments in Fluids*, *58*(4), 30. https://doi.org/10.1007/s00348-017-2319-9

Ervine D. A., Willetts B. B., Sellin R. H. J., & Lorena M. (1993). Factors Affecting Conveyance in Meandering Compound Flows. *Journal of Hydraulic Engineering*, *119*(12), 1383–1399. https://doi.org/10.1061/(ASCE)0733-9429(1993)119:12(1383)

Fakhri, A., Ettema, R., Aliyari, F., & Nowroozpour, A. (2020). Large-Scale Particle Image Velocimetry for Estimating Vena-Contracta Width for Flow in Contracted Open Channels. *Water*, *13*(1), 31.

Friedman, J. M., & Lee, V. J. (2002). Extreme Floods, Channel Change, and Riparian Forests Along Ephemeral Streams. *Ecological Monographs*, *72*(3), 409–425. https://doi.org/10.1890/0012-9615(2002)072[0409:EFCCAR]2.0.CO;2

Fuller, M. R., Leinenbach, P., Detenbeck, N. E., Labiosa, R., & Isaak, D. J. (2022). Riparian vegetation shade restoration and loss effects on recent and future stream temperatures. *Restoration Ecology*, *30*(7), e13626.

Garcia, X.-F., Schnauder, I., & Pusch, M. (2012). Complex hydromorphology of meanders can support benthic invertebrate diversity in rivers. *Hydrobiologia*, *685*, 49–68.

Geerling, G., Kater, E., Van den Brink, C., Baptist, M., Ragas, A., & Smits, A. (2008). Nature rehabilitation by floodplain excavation: The hydraulic effect of 16 years of sedimentation and vegetation succession along the Waal River, NL. *Geomorphology*, *99*(1–4), 317–328.

Hickin, E. J. (1984). Vegetation and River Channel Dynamics. *The Canadian Geographer / Le Géographe Canadien*, *28*(2), 111–126. https://doi.org/10.1111/j.1541-0064.1984.tb00779.x

Ielpi, A., Lapôtre, M. G. A., Gibling, M. R., & Boyce, C. K. (2022). The impact of vegetation on meandering rivers. *Nature Reviews Earth & Environment*, *3*(3), 165–178. https://doi.org/10.1038/s43017-021-00249-6

Ishigaki, T., Shiono, K., Rameshwaran, P., Scott, C. F., & Muto, Y. (2000). Impact of Secondary Flow on Bed Form and Sediment Transport in a Meandering Channel for Overbank Flow. *PROCEEDINGS OF HYDRAULIC ENGINEERING*, *44*, 849–854. https://doi.org/10.2208/prohe.44.849

Järvelä, J. (2002). Flow resistance of flexible and stiff vegetation: a flume study with natural plants. *Journal of Hydrology*, *269*(1), 44–54. https://doi.org/10.1016/S0022-1694(02)00193-2

Järvelä, J. (2004). Determination of flow resistance caused by non-submerged woody vegetation. *International Journal of River Basin Management*, *2*(1), 61–70. https://doi.org/10.1080/15715124.2004.9635222

Järvelä, J. (2005). Effect of submerged flexible vegetation on flow structure and resistance. *Journal of Hydrology*, *307*(1–4), 233–241.

Johnson, E., & Cowen, E. (2017). Remote determination of the velocity index and mean streamwise velocity profiles. *Water Resources Research*, *53*(9), 7521–7535.

Karamisheva, R. D., Lyness, J. F., Myers, W. R. C., & O'Sullivan, J. (2006). Sediment discharge prediction in meandering compound channels. *Journal of Hydraulic Research*, *44*(5), 603–613. https://doi.org/10.1080/00221686.2006.9521710

Kondolf, G. M., & Curry, R. R. (1986). Channel erosion along the Carmel river, Monterey county, California. *Earth Surface Processes and Landforms*, *11*(3), 307–319. https://doi.org/10.1002/esp.3290110308

Le Bouteiller, C., & Venditti, J. G. (2015). Sediment transport and shear stress partitioning in a vegetated flow. *Water Resources Research*, *51*(4), 2901–2922. https://doi.org/10.1002/2014WR015825

Le Coz, J., Jodeau, M., Hauet, A., Marchand, B., & Le Boursicaud, R. (2014). Image-based velocity and discharge measurements in field and laboratory river engineering studies using the free FUDAA-LSPIV software (Vol. 3, pp. 2014–05). Presented at the Proceedings of the international conference on fluvial hydraulics, River Flow.

Legleiter, C. J., & Kinzel III, P. J. (2021). Surface flow velocities from space: Particle image velocimetry of satellite video of a large, sediment-laden river. *Frontiers in Water*, *3*, 652213.

Legleiter, C. J., & Kinzel, P. J. (2020). Inferring surface flow velocities in sediment-laden Alaskan rivers from optical image sequences acquired from a helicopter. *Remote Sensing*, *12*(8), 1282.

Legleiter, C. J., & Kinzel, P. J. (n.d.). The Toolbox for River Velocimetry using Images from Aircraft (TRiVIA). *River Research and Applications*, *n/a*(n/a). https://doi.org/10.1002/rra.4147

Liébault, F., & Piégay, H. (2002). Causes of 20th century channel narrowing in mountain and piedmont rivers of southeastern France. *Earth Surface Processes and Landforms*, *27*(4), 425–444. https://doi.org/10.1002/esp.328

Lightbody, A. F., Kui, L., Stella, J. C., Skorko, K. W., Bywater-Reyes, S., & Wilcox, A. C. (2019). Riparian Vegetation and Sediment Supply Regulate the Morphodynamic Response of an Experimental Stream to Floods. *Frontiers in Environmental Science*, *7*. https://doi.org/10.3389/fenvs.2019.00040

Lininger, K. B., Wohl, E., Rose, J. R., & Leisz, S. J. (2019). Significant Floodplain Soil Organic Carbon Storage Along a Large High-Latitude River and its Tributaries. *Geophysical Research Letters*, *46*(4), 2121–2129. https://doi.org/10.1029/2018GL080996

Liu, C., Shan, Y., Liu, X., Yang, K., & Liao, H. (2016). The effect of floodplain grass on the flow characteristics of meandering compound channels. *Journal of Hydrology*, *542*, 1–17. https://doi.org/10.1016/j.jhydrol.2016.07.037

Lyness, J. F., Myers, W. R. C., Cassells, J. B. C., & O'Sullivan, J. J. (2001). The influence of planform on flow resistance in mobile bed compound channels. In *Proceedings of the Institution of Civil Engineers-Water and Maritime Engineering* (Vol. 148, pp. 5–14). Thomas Telford Ltd. Retrieved from https://sci-hub.se/https://doi.org/10.1680/wame.2001.148.1.5

MacVicar, B. (2023). MITT. GitHub. Retrieved from https://github.com/macvicab/MITT

MacVicar, B., Dilling, S., & Lacey, J. (2014). Multi-instrument turbulence toolbox (MITT): Open-source MATLAB algorithms for the analysis of high-frequency flow velocity time series datasets. *Computers & Geosciences*, *73*, 88–98.

Millar, R. G. (2000). Influence of bank vegetation on alluvial channel patterns. *Water Resources Research*, *36*(4), 1109–1118. https://doi.org/10.1029/1999WR900346

Naghavi, M., Mohammadi, M., & Mahtabi, G. (2022). An experimental evaluation of the blocks in floodplain on hydraulic characteristics of flow in a meandering compound channel. *Journal of Hydrology*, *612*, 127976. https://doi.org/10.1016/j.jhydrol.2022.127976

Nepf, H. M. (1999). Drag, turbulence, and diffusion in flow through emergent vegetation. *Water Resources Research*, *35*(2), 479–489.

Nepf, H. M. (2012). Flow and transport in regions with aquatic vegetation. *Annual Review of Fluid Mechanics*, *44*, 123–142.

Parker, G. (1991). Selective Sorting and Abrasion of River Gravel. II: Applications. *Journal of Hydraulic Engineering*, *117*(2), 150–171. https://doi.org/10.1061/(ASCE)0733-9429(1991)117:2(150)

Patra, K. C., & Kar, S. K. (2000). Flow Interaction of Meandering River with Floodplains. *Journal of Hydraulic Engineering*, *126*(8), 593–604. https://doi.org/10.1061/(ASCE)0733-9429(2000)126:8(593)

Perucca, E., Camporeale, C., & Ridolfi, L. (2007). Significance of the riparian vegetation dynamics on meandering river morphodynamics: MEANDERING RIVERS AND RIPARIAN VEGETATION. *Water Resour. Res.*, *43*(3), 55. https://doi.org/10.1029/2006WR005234

Poff, N. L., Allan, J. D., Bain, M. B., Karr, J. R., Prestegaard, K. L., Richter, B. D., et al. (1997). The Natural Flow Regime. *BioScience*, *47*(11), 769–784. https://doi.org/10.2307/1313099

Rantz, S. E. (1982). *Measurement and computation of streamflow* (Report No. 2175) (Vol. 1 & 2). https://doi.org/10.3133/wsp2175

Resh, V. H., Brown, A. V., Covich, A. P., Gurtz, M. E., Li, H. W., Minshall, G. W., et al. (1988). The role of disturbance in stream ecology. *Journal of the North American Benthological Society*, *7*(4), 433–455.

Sellin, R., Ervine, D., & Willetts, B. (1993). Behaviour of meandering two-stage channels. *Proceedings of the Institution of Civil Engineers-Water Maritime and Energy*, *101*(2), 99–111.

Shiono, K., Chan, T. L., Spooner, J., Rameshwaran, P., & Chandler, J. H. (2009a). The effect of floodplain roughness on flow structures, bedforms and sediment transport rates in

meandering channels with overbank flows: Part I. *Journal of Hydraulic Research*, *47*(1), 5–19. https://doi.org/10.3826/jhr.2009.2944-I

Shiono, K., Chan, T. L., Spooner, J., Rameshwaran, P., & Chandler, J. H. (2009b). The effect of floodplain roughness on flow structures, bedforms and sediment transport rates in meandering channels with overbank flows: Part II. *Journal of Hydraulic Research*, *47*(1), 20–28. https://doi.org/10.3826/jhr.2009.2944-II

Sparks, R. E., Bayley, P. B., Kohler, S. L., & Osborne, L. L. (1990). Disturbance and recovery of large floodplain rivers. *Environmental Management*, *14*, 699–709.

Steiger, J., & Gurnell, A. M. (2003). Spatial hydrogeomorphological influences on sediment and nutrient deposition in riparian zones: observations from the Garonne River, France. *Geomorphology*, *49*(1), 1–23. https://doi.org/10.1016/S0169-555X(02)00144-7

Stone, M. C., Byrne, C. F., & Morrison, R. R. (2017). Evaluating the impacts of hydrologic and geomorphic alterations on floodplain connectivity. *Ecohydrology*, *10*(5), e1833. https://doi.org/10.1002/eco.1833

Strelnikova, D., Paulus, G., Käfer, S., Anders, K.-H., Mayr, P., Mader, H., et al. (2020). Drone-based optical measurements of heterogeneous surface velocity fields around fish passages at hydropower dams. *Remote Sensing*, *12*(3), 384.

Sutfin, N. A., Wohl, E. E., & Dwire, K. A. (2016). Banking carbon: a review of organic carbon storage and physical factors influencing retention in floodplains and riparian ecosystems. *Earth Surface Processes and Landforms*, *41*(1), 38–60. https://doi.org/10.1002/esp.3857

Tanino, Y., & Nepf, H. M. (2008). Laboratory Investigation of Mean Drag in a Random Array of Rigid, Emergent Cylinders. *Journal of Hydraulic Engineering*, *134*(1), 34–41. https://doi.org/10.1061/(ASCE)0733-9429(2008)134:1(34)

Theurer, F. D., Lines, I., & Nelson, T. (1985). INTERACTION BETWEEN RIPARIAN VEGETATION, WATER TEMPERATURE, AND SALMONID HABITAT IN THE TUCANNON RIVER 1. *JAWRA Journal of the American Water Resources Association*, *21*(1), 53–64.

Tonina, D., & Buffington, J. M. (2007). Hyporheic exchange in gravel bed rivers with pool-riffle morphology: Laboratory experiments and three-dimensional modeling. *Water Resources Research*, *43*(1).

Török, G. T., & Parker, G. (2022). The influence of riparian woody vegetation on bankfull alluvial river morphodynamics. *Scientific Reports*, *12*(1), 18141. https://doi.org/10.1038/s41598-022-22846-1

Vargas-Luna, A., Crosato, A., & Uijttewaal, W. S. J. (2015). Effects of vegetation on flow and sediment transport: comparative analyses and validation of predicting models. *Earth Surface Processes and Landforms*, *40*(2), 157–176. https://doi.org/10.1002/esp.3633

Vargas-Luna, A., Crosato, A., Calvani, G., & Uijttewaal, W. S. J. (2016). Representing plants as rigid cylinders in experiments and models. *Advances in Water Resources*, *93*, 205–222. https://doi.org/10.1016/j.advwatres.2015.10.004

Vogel, S. (1989). Drag and reconfiguration of broad leaves in high winds. *Journal of Experimental Botany*, *40*(8), 941–948.

Whiting, P. J., & Dietrich, W. E. (1990). Boundary Shear Stress and Roughness Over Mobile Alluvial Beds. *Journal of Hydraulic Engineering*, *116*(12), 1495–1511. https://doi.org/10.1061/(ASCE)0733-9429(1990)116:12(1495)

Wilcock, P. R. (1996). Estimating Local Bed Shear Stress from Velocity Observations. *Water Resources Research*, *32*(11), 3361–3366. https://doi.org/10.1029/96WR02277

Wormleaton, P. R., Sellin, R. H. J., Bryant, T., Loveless, J. H., Hey, R. D., & Catmur, S. E. (2004). Flow structures in a two-stage channel with a mobile bed. *Journal of Hydraulic Research*, *42*(2), 145–162.

Wormleaton, P. R., Hey, R. D., Sellin, R. H., Bryant, T., Loveless, J., & Catmur, S. E. (2005). Behavior of Meandering Overbank Channels with Graded Sand Beds. *Journal of Hydraulic Engineering*, *131*(8), 665–681. https://doi.org/10.1061/(ASCE)0733-9429(2005)131:8(665)

Yager, E. M., & Schmeeckle, M. W. (2013). The influence of vegetation on turbulence and bed load transport. *Journal of Geophysical Research: Earth Surface*, *118*(3), 1585–1601. https://doi.org/10.1002/jgrf.20085

Yager, Elowyn M., Venditti, J. G., Smith, H. J., & Schmeeckle, M. W. (2018). The trouble with shear stress. *Geomorphology*, *323*, 41–50. https://doi.org/10.1016/j.geomorph.2018.09.008

Zhu, L., Chen, D., Hassan, M. A., & Venditti, J. G. (2022). The Influence of Riparian Vegetation on the Sinuosity and Lateral Stability of Meandering Channels. *Geophysical Research Letters*, *49*(2), e2021GL096346. https://doi.org/10.1029/2021GL096346

# CHAPTER 4: MODELING THE INFLUENCE OF RIGID VEGETATION ON CHANNEL-FLOODPLAIN CONNECTIVITY

## 4.1 Introduction

Many river channels have historically been modified for flow regulation, transportation, and conveyance (Elosegi & Sabater, 2013; McCluney et al., 2014; Wohl, 2019). This has been achieved through channel modifications such as altered cross-section and planform geometry and by constructing flood mitigation infrastructure such as levees and dams (Boulange et al., 2021; K. J. Gregory, 2006; R. L. Knox et al., 2022; Kondolf, 1997; Nilsson et al., 2005) resulting in hydraulically disconnected channel-floodplain systems (R. Knox et al., 2021; Thoms, 2003; Wohl, 2017). Many studies have shown that floods that occasionally interact with the floodplain provide important ecosystem services (Poff et al., 1997) including nutrient cycling (Baldwin & Mitchell, 2000; Olde Venterink et al., 2006), habitat provisioning (Benke, 2001; Junk et al., 1989), and aquifer recharge (Helton et al., 2014; McCallum et al., 2014). Floodplains also serve to attenuate flood pulses as water spreads out and is slowed during high flows (Lininger & Latrubesse, 2016; Sholtes & Doyle, 2011).

Vegetation and other land cover types influence the ecosystem services provided by floodplains and alter channel geomorphology. Vegetation provides important riparian habitat for birds and other animals (Nilsson & Dynesius, 1994), improves water quality (Dosskey et al., 2010), stabilizes banks (S. Gregory et al., 2019; Henriques et al., 2022; Ielpi & Lapôtre, 2020), and slows flow as it exits the channel during floods attenuating flood wave propagation (Anderson et al., 2006). This biophysical flood mitigation may ease the increased pressure on constructed flood mitigation infrastructure. These benefits and the recognized importance of

floodplains encourages managers to view riparian zones holistically as river corridors (Harvey & Gooseff, 2015), incorporating the influence of biological, geomorphic, and hydrologic dynamics across the active channel, floodplain, and hyporheic zone. An expanded view of river corridor processes requires the expansion of tools and resources to analyze and predict overbank hydrodynamics.

Increasing availability of remotely sensed data such airborne LiDAR, drone, and satellite imagery make hydrodynamic modeling and analysis of biogeomorphic river corridor characteristics feasible, yet there remains a marked lack of widely used tools to quickly and accurately classify vegetation characteristics that influence hydraulic roughness parameters. In scientific disciplines such as agriculture and forestry, researchers have developed analytical methods that may be suitable for river scientists, particularly for classifying large rigid trees characteristic of floodplains. These large trees strongly influence the exchange of water and nutrients between the channel and floodplain, but the extent to which floodplain vegetation controls the exchange of flow is poorly understood.

Floodplain flow is inherently complex due to the varied nature of land cover types such as vegetation which exert spatially varied drag forces that are a function of physical vegetation characteristics and flow depth. Flow through vegetation has been characterized as submerged and emergent with two distinct vegetation categories, flexible and rigid. The flow resistance exerted by cylindrical vegetation elements has been described quantitatively as

$$F = \frac{1}{2}\rho C_D A_C U^2 \quad (1)$$

where $\rho$ is fluid density, $C_D$ is a drag coefficient, $A_C$ is the characteristic plant area, and $U$ = approach velocity. $A_C$ is often defined as the frontal projected area, and the $C_D$ depends on the

Reynolds number, but in the case of cylindrical rigid stems, a value of 1 is commonly used for $C_D$ (Baptist et al., 2007; Nehal et al., 2012) and this value is used in the modeling scenarios in this study.

Many studies have been performed to improve our ability to quantify vegetation characteristics, and estimate drag exerted on the flow field through numerical and laboratory simulations (Aberle & Järvelä, 2013; Box et al., 2022; Nepf, 1999). Luhar & Nepf (2013) performed physical modeling experiments to quantify hydraulic roughness due to vegetation and developed the following equation to estimate Manning's roughness coefficient as a function of frontal area, drag coefficient and flow depth

$$n = K_n \left[\frac{C_D a h}{2g}\right]^{1/2} h^{1/6} \tag{2}$$

where $n$ is Manning's roughness coefficient, $K_n$ is a Manning's constant to adjust for units (1.0 for SI and 1.49 for US units), $a$ is projected frontal area, and $h$ is flow depth. Baptist et al. (2007) proposed an approach for rigid vegetation based on Chezy coefficient as a function of stem density, stem diameter, flow depth, and an estimate of roughness due to the bed.

Recently, due to the increased availability of remotely sensed data, many studies have proposed methods to quantify vegetation characteristics, particularly in the forestry science literature. These studies can provide effective tools to estimate vegetation characteristics useful for parameterizing hydraulic roughness coefficients such as Manning's coefficient. For example, Zhu et al. (2018) classified vegetation characteristics such as wood or leaf using trained classification models and terrestrial LiDAR (TLS) survey data. Isibue & Pingel, (2020) estimated diameter at breast height (DBH) of single trees using both structure from motion (SfM) photogrammetry and aerial LiDAR. Windrim & Bryson, (2020) used deep learning to detect,

segment, and model fit individual tree stems. Hershey et al. (2022) developed a voxel-based approach to detect individual tree stems using airborne LiDAR in dense mature forests.

In Chapter 3 of this dissertation, I analyzed the 3D flow field in a meandering compound channel and the influence of rigid floodplain vegetation. The results showed that (1) in-channel secondary currents are strengthened with floodplain vegetation density, (2) a depth-averaged approach to estimate shear stress predicts lower values than an approach that incorporates the 3D nature of flow near the bed, and that (3) channel-floodplain exchange is significantly attenuated with high-density floodplain vegetation vs. low-density vegetation or a bare floodplain. Given the fact that flow through rigid vegetation is highly three-dimensional and being compelled by the disparity in shear stress estimates using two approaches, I conducted the following numerical experiments to see if a 2D model produces similar flow dynamics to the results presented in Chapter 3.

Through these hydraulic modeling experiments, I aim to improve our understanding of the influence of floodplain vegetation on channel-floodplain flow dynamics, demonstrate the utility of remote-sensing tools to quickly characterize floodplain vegetation characteristics to be used in hydrodynamic modeling, and assess 2D hydraulic model output in the context of physical modeling studies. To my knowledge, there are no studies that have conducted 2D hydraulic modeling studies compared with controlled physical modeling experiments regarding the influence of floodplain vegetation on flow dynamics and channel-floodplain connectivity. I outline the specific objectives below:

- Objective 1: Asses the suitability of TreeLS, a LiDAR point cloud processing tool, for detection and classification of trees on the floodplain of the Butokamabetsu River, the

site of ongoing research investigating the role of channel-floodplain connectivity in ecosystem dynamics (Uno et al., 2022). I use TreeLS to develop a raster map of stem density and average stem diameter to compute Manning's roughness coefficient to be used in Objective 2.

- Objective 2: Investigate the influence of floodplain vegetation density on channel-floodplain exchange flow using a 2D hydraulic models. I test four floodplain roughness scenarios that are developed using a range of vegetation densities comparable to the physical modeling study presented in Chapters 2 and 3.

- Objective 3: Assess the effectiveness of empirically derived equations for predicting flow resistance due to varied vegetation density in a natural channel.

To achieve Objective 1, I processed LiDAR point cloud data using the TreeLS R package. The TreeLS package functions detect, segment, and apply a cylindrical best-fit function to estimate tree height and diameter at breast height. I then computed stem density and developed raster maps of tree characteristics. I then applied an empirical formula to estimate Manning's coefficient due to the rigid emergent vegetation. To achieve Objective 2, I simulated four channel and floodplain roughness scenarios with varying floodplain vegetation densities and computed channel-floodplain exchange flow at the left and right banks.

## 4.2 Site description

The Butokamabetsu River is located in the Hokkaido University Uryu Experimental Forest in Northern Japan (See Figure 4.1). The main channel is approximately 10-m wide and there are many side channels that become inundated at flows with an approximately 1-year return interval. Many of these side channels may be hydrologically connected to the main channel via hyporheic exchange at all flows but become connected via surface flow at various stages of the annual hydrograph during flood resulting in unique aquatic organism communities that are isolated in small pool habitats during parts of the year. A gradient of hydrological connectivity to the river exists among waterbodies on the floodplain (Uno et al., 2022). Investigating the flows at which these side channels and pools become connected via surface flow provides insight into ecosystem dynamics and biodiversity associated with channel-floodplain connectivity.

Floodplain vegetation through the river corridor is composed of large deciduous trees such as alder (*Alnus japonica*) and Japanese white birch (*Betula platyphylla*). A shrubby broad-leaf bamboo (*Sasa senanensis*) is also common. Peak flows typically occur in the autumn with heavy rains and during spring time following winter snowmelt (See Figure 4.2d). A flow gauge is located on the Butokamabetsu River near the study site upstream of Lake Shumarinai, which covers approximately 23.7 $km^2$ and is impounded by the Ury Dam, forming the only reservoir in Hokkaido. The Butokamabetsu River is the location of intensive long term forest monitoring with a gauging record that extends back to 1987. A 1.5-year return interval flow has a discharge of 19.9 $m^3/s$. The maximum recorded flow in the period of record is 107.6 $m^3/s$.

The study site has been separated into three reaches for analysis (See Table 1, and Figure 4.1). These three reaches have been monitored as part of an ongoing ecohydrological research project. Reach 1 is the lowermost reach at an elevation of 294-m at the downstream extant and

has valley length of 452 m. Reach 2 is the middle reach at 312-m in elevation and has a valley length of 526-m. Reach 3 is the upper reach at 363-m elevation and has a valley length of 602 m.

**Table 4.1**. Site characteristics for each of three modeled reaches

| Reach | Channel Width (m) | Channel Length (m) | Valley Length (m) | Slope (m/m) | Sinuosity | Mean Raster Floodplain Vegetation Density (stems/$m^2$) | Mean Raster Vegetation Stem Diameter (m) |
|---|---|---|---|---|---|---|---|
| 1 | 12.0 | 494 | 452 | 0.005 | 1.09 | 0.02 | 0.10 |
| 2 | 10.0 | 596 | 526 | 0.006 | 1.13 | 0.04 | 0.13 |
| 3 | 11.5 | 649 | 602 | 0.011 | 1.08 | 0.09 | 0.17 |

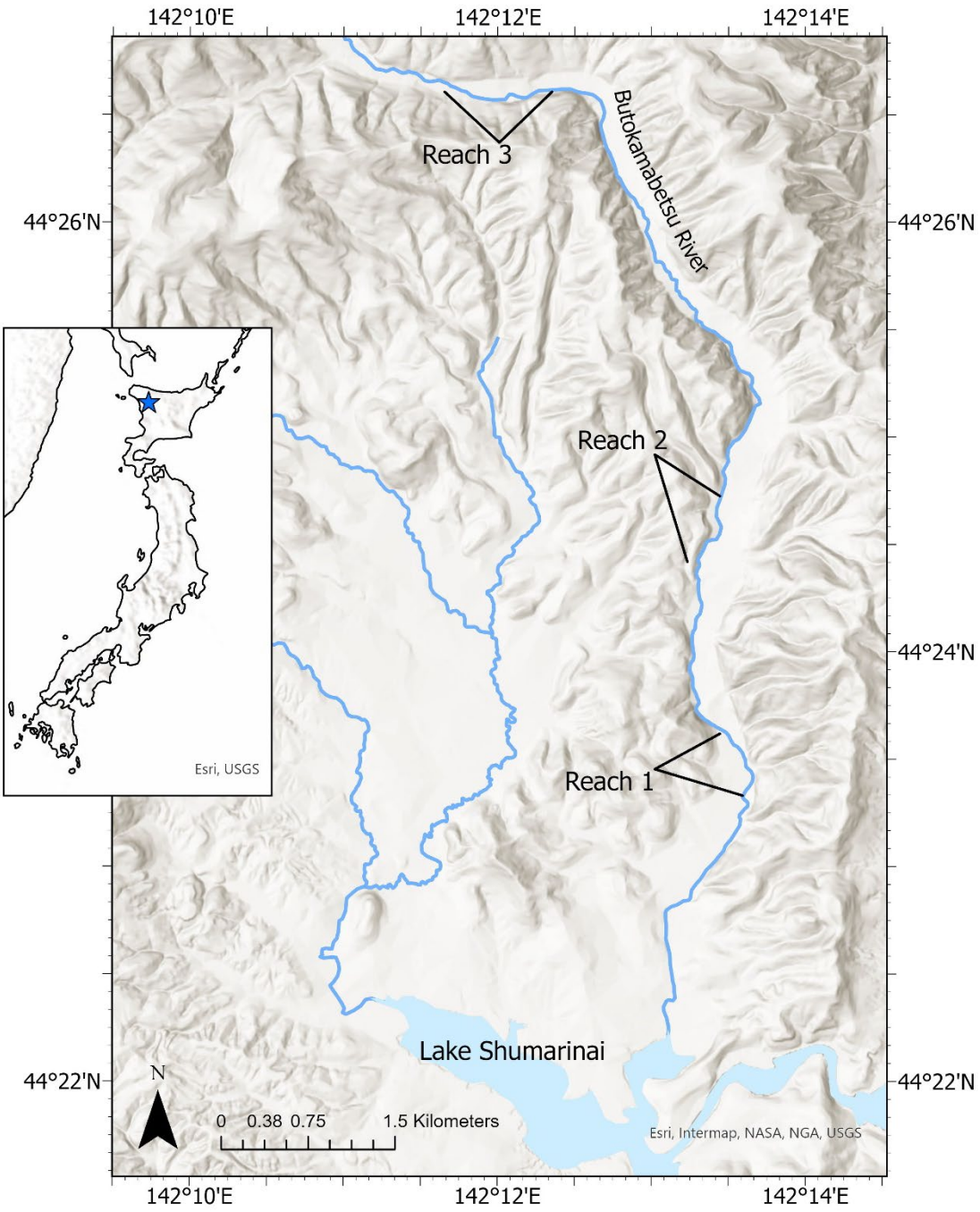


**Figure 4.1.** Site map. LiDAR data was collected at each of the three reaches shown in the figure where floodplain vegetation characteristics were measured. Floodplain vegetation hydraulic roughness maps were developed for all three reaches and hydraulic modeling conducted.

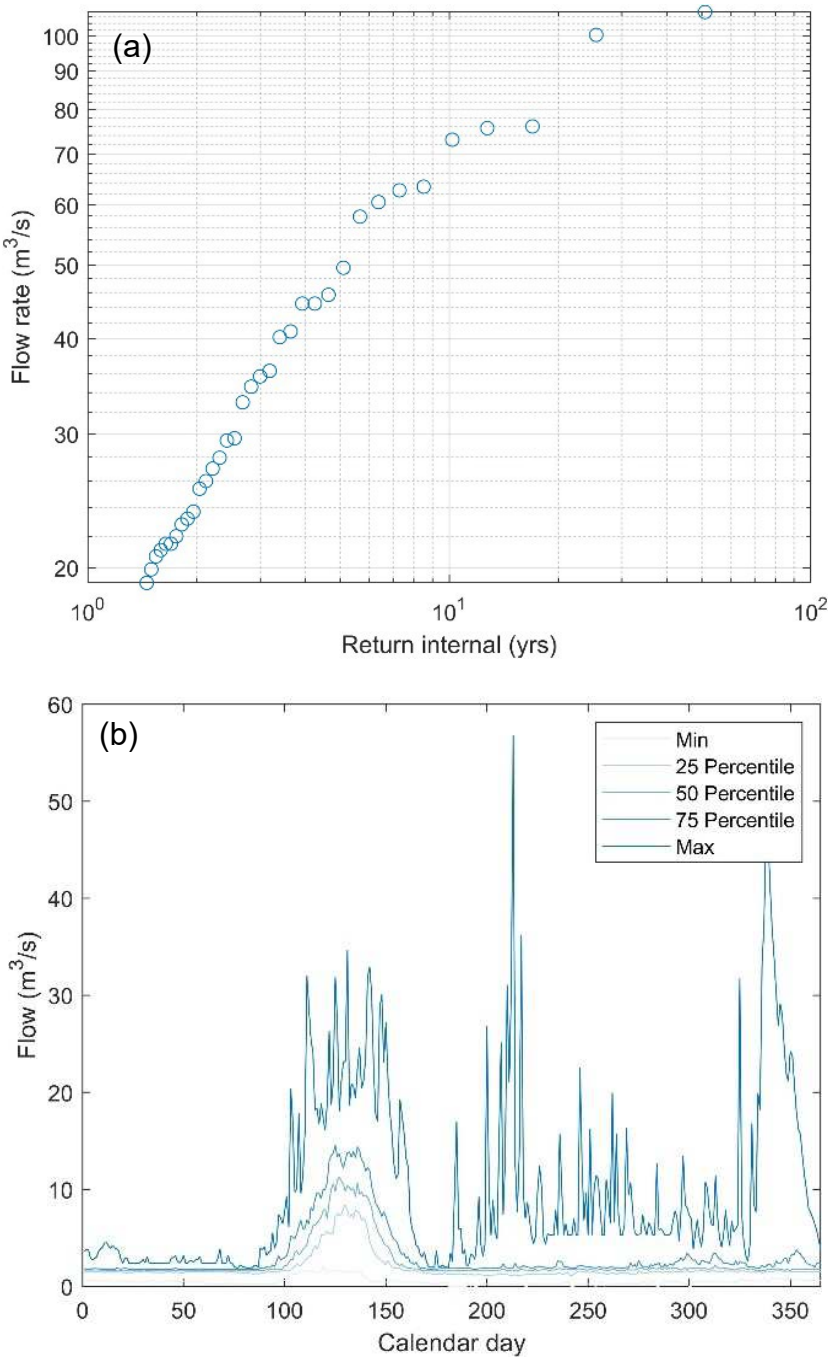


**Figure 4.2.** (a) Peak annual instantaneous discharge return intervals for the period of record. (b) Percentiles of mean daily discharge for the period of record. The hydrograph is characterized by typical annual snowmelt that occurs in April and summer typhoon rainstorms.

## 4.3 Methods

To investigate the influence of varied floodplain vegetation conditions and estimated roughness coefficients, I investigate the reach-scale hydraulic response to four experimental floodplain roughness scenarios informed by aerial LiDAR tree detection surveys. LiDAR was collected at each of the three reaches after which I used TreeLS ("TreeLS," 2023), a point cloud vegetation processing R package, to identify and estimate tree characteristics including diameter at breast height (DBH), stem density, and stem height. I estimated hydraulic roughness as Manning's coefficient due to these trees and developed hydraulic models in the Hydrologic Engineering Center's River Analysis System (HEC-RAS) program.

### *4.3.1 Vegetation detection and classification*

The aerial LiDAR scans (ALS) were conducted on 01 November 2022 using a DJI Zenmuse LiDAR scanner on the DJI Matrice 300 RTK UAV platform. The flights were conducted at a height of 100 m, speed of 2 m/s, with a 90% front and side overlap. The LiDAR sample rate was 160KHz.

The LiDAR point clouds were classified to identify ground, water, and non-ground points using the classify LAS ground tool in the ArcGIS spatial analyst toolbox. I then manually classified the water within the channel. To characterize the woody vegetation in each of the three study reaches, I performed tree segmentation and stem classification using TreeLS, an R language point cloud processing package (de Conto et al., 2017). The TreeLS package and functions were accessed at the TreeLS GitHub repository (2023).

TreeLS utilizes a Hough transformation to denoise the point cloud and detect stem points. The Hough transformation in this application analyzes horizontal slices of a ground-normalized point cloud and searches for circular shapes oriented orthogonal to the ground. Circles with a

range of radii as defined by the user are compared to surrounding pixels and the circle with a radius that has the most common adjacent LiDAR pixels is identified circle characterizing that horizontal slice of the LiDAR point cloud. A statistical random sample consensus (RANSAC) algorithm then compares all points in 3 dimensions identified by the Hough transformation and fits a circle to the stem segments stacked vertically to estimate stem diameter and height. This statistical fit is displayed graphically in Figure 4.3 below (from Figure 5 in de Conto et al., 2017). In the TreeLS program, there are various functions and parameters that can be adjusted to best suit the point cloud data and being analyzed and optimize processing time.

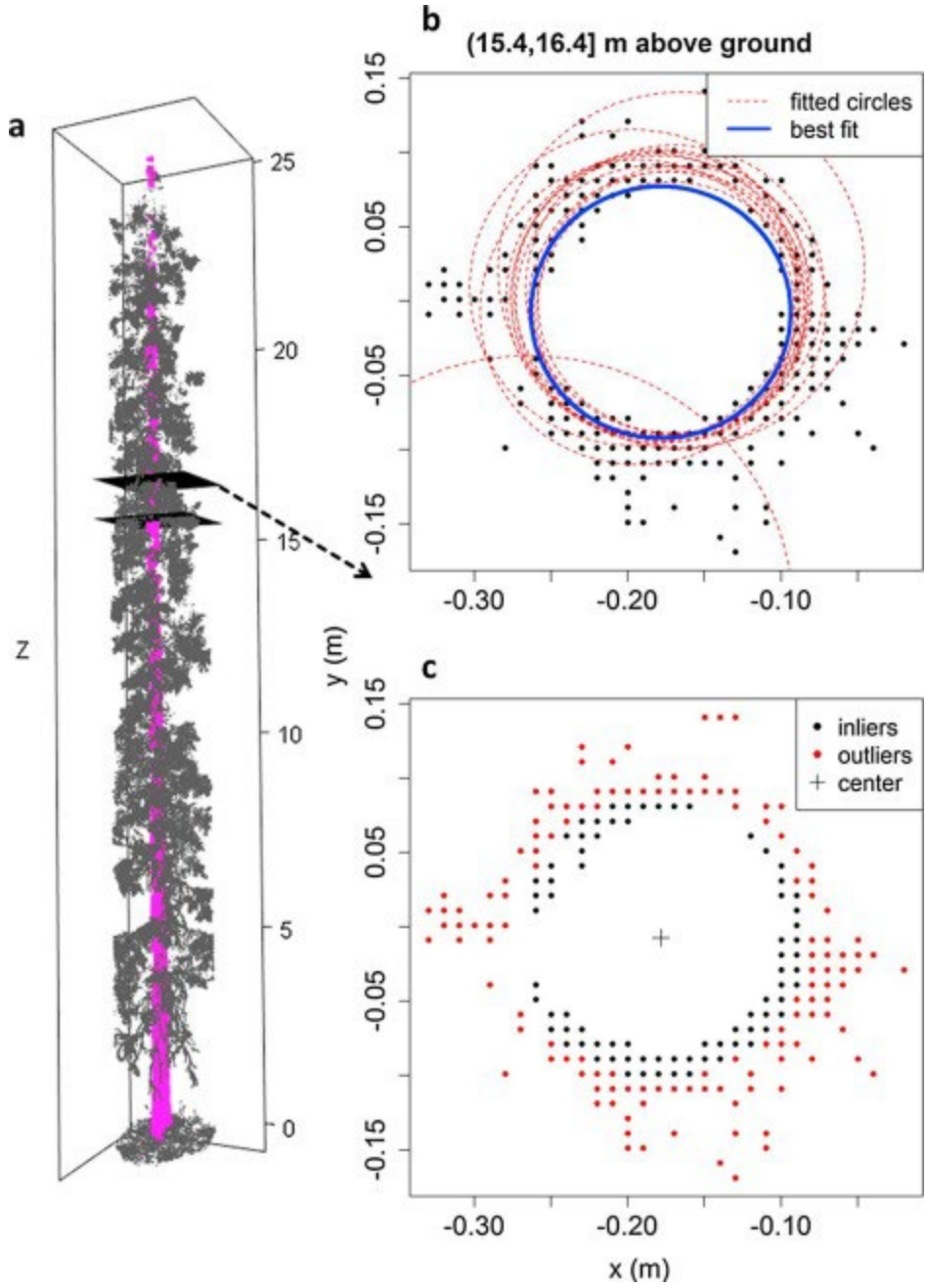


**Figure 4.3.** Figure from de Conto et al. (2017) depicting one of two methods for classifying stems. In this method, a random sampling consensus (RANSAC) algorithm computes the probability that a sample of points contains no outliers and identifies a best fit circle to approximate the stem diameter and height.

I normalized the point cloud using the TreeLS function, tlsNormalize, so that each ground classified point is positioned at an elevation of 0 and thinned the point cloud by voxel using the TreeLS function, tlsSample, with a voxel size of 0.01 $m^2$. I then performed the Hough transformation and established a maximum stem diameter of 3 m for optimization as this was the upper range of tree diameter identified through visual inspection of drone imagery survey and the LiDAR point clouds. Once the LiDAR point clouds were processed I the TreeLS program, I visually assessed the accuracy of the stem segmentation by overlaying detected stem points on drone imagery that was taken the day of the LiDAR flight. I also visually checked the output point cloud including the identified stem points such as those shown in Figure 4.4b and Figure 4.4c. The program performed best identifying stems where shrubby vegetation was absent, where floodplain topographic relief was minimal, and where stems were less dense. Where there were tall shrubs (height > 1.37 m), it occasionally misidentified them as stems, particularly where the shrub point cloud density was highest, however, Figure 4.4 depicts the accuracy of the stem detection and resulting computed density.

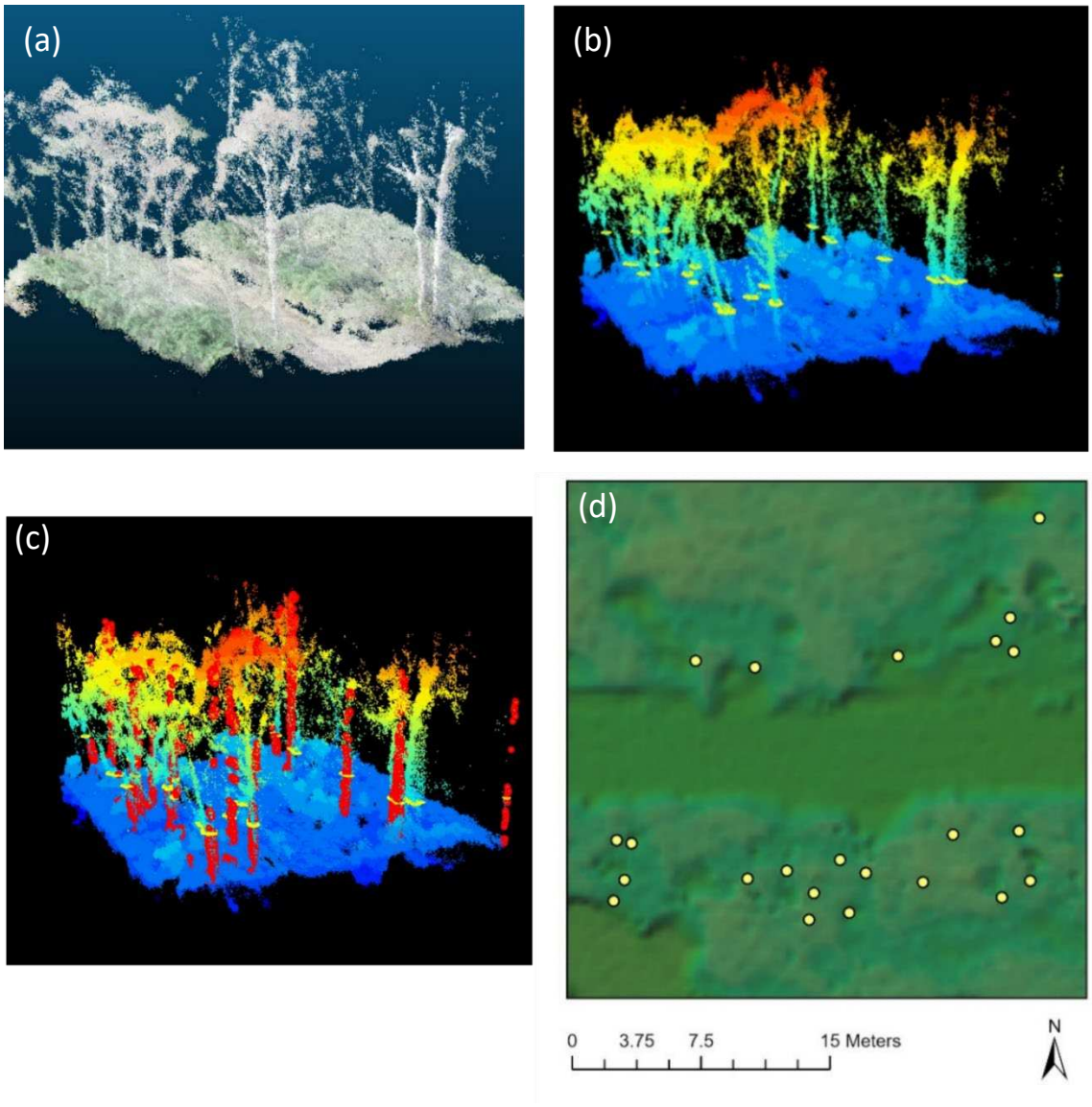


**Figure 4.4.** Display of TreeLS tree inventory survey using aerial LiDAR point cloud. (a) LiDAR point cloud .las tile with RGB point coloration. (b) The same LiDAR tile with a rainbow color gradient height ramp with trees identified at a height of 1.37-m above the ground. The yellow discs shown represent individual stems and are slightly larger than the estimated stem diameter for visibility. (c) The points in red indicate those that fall within the random sampling consensus best fit circle included for interpretability. (d) Aerial view of stem locations plotted over a ground-classified hillshade.

*4.3.2 Computing Manning's roughness due to rigid, emergent, vegetation*

I followed a similar approach to Chaulagain et al. (2022) using the Baptist et al. (2007) approach to estimate hydraulic roughness due to vegetation. However, in my approach I focus primarily on the large trees that dominate the floodplain vegetation along the Butokama River rather than simply using LiDAR point density to compute vegetation density. Using the emergent, rigid, vegetation characteristics, I calculate *C*, the Chezy resistance coefficient

$$C = \sqrt{\frac{1}{\left(\frac{1}{C_b^2}\right) + \left(\frac{C_d m D_s h}{2g}\right)}} \tag{3}$$

where $m$ is vegetation density (stems/m$^2$), $D_s$ is plant stem diameter (m), $C_b$ is the Chezy coefficient resulting from bed roughness, and $h$ is flow depth (m). I determined $C_b$ in the model calibration process and converted Manning's coefficient to $C$ using the following equation which relates Manning's coefficient, the roughness parameter built into the modeling program, HEC-RAS, to $C$:

$$n = \frac{1}{C} h^{1/6} \tag{4}$$

where $h$ is the flow depth. For the purpose of this study, I used an estimated flow depth of 0.1 m, which is representative of high flows proximal to the channel in each reach that were captured with the game-camera imagery. An iterative process could be used to converge on the most appropriate estimate of calibrated hydraulic roughness coefficients, such as the method described by Chaulagain et al., (2022), however, the software developed for that study is not publicly available. In this study, my intent is not to most closely estimate a Manning's roughness coefficient for floodplain flow, but to investigate the feasibility of using advanced LiDAR tools

for characterizing floodplain vegetation and investigate flow response to varied vegetation densities similar to Chapter 2, in a natural river corridor.

*4.3.3 Model development and calibration*

In HEC-RAS 2D, I used the 2D diffusive wave equations for the numerical simulations. The computational mesh upon which the computations were performed was generated with a cell spacing of 3 m on the floodplain and 1 m within the main and side channels. The topography associated with the computational grid was extracted from the LiDAR point clouds by removing vegetation in ArcGIS Pro using the classify LAS ground tool in the spatial analyst toolbox. The aerial LiDAR surveys were conducted during the winter low flow season and as such capture a significant portion of the channel topography, however there was 1.6 $m^3/s$ in the active channel and underlying bathymetry that needed to be accounted for in the hydraulic model as the LiDAR survey only captured the water's surface.


**Figure 4.5.** Photos from Reach 1 pointed toward a large side channel. This photo sequence shows an example of the methods described to calibrate the Manning's coefficient values in the channel. In (a), taken 04 May 2022, the side channel is fully hydraulically connected. In (b), taken 05 May 2022, the channel is at the threshold of being fully hydraulically connected. This is the target stage identified to achieve a calibrated Manning's roughness. In (c), taken 11 May 2022, there is no surface flow in the side channel.

I estimated channel bathymetry by hydroflattening the water surface and cutting a 0.21-m high trapezoid into the channel where water was present. I use 0.21-m because this was the depth of flow on the date that the aerial LiDAR surveys were conducted. Although applying a uniform depth through the channel for all three reaches may neglect the topographic characteristics of the bed, this likely has little influence on the results that I focus on in this study as flow in the active channel at that depth only accounts for approximately 1% of the total discharge for the three flow rates analyzed. The channel Manning's coefficient values were calibrated using time-series images that were captured at side channels located in each of the three reaches and the corresponding flow rate at the time of the photo. The stage at which the side channels became fully hydraulically connected to the main channel via surface flow was noted and the main and side channel Manning's coefficient values were adjusted to achieve the same hydraulic connectivity between main and side channel. Full hydraulic connectivity between main and side channel was determined using the Plot Hydraulic Connectivity tool in RAS Mapper and I determined that it had been achieved when a continuous line through the entire side channel was visible. In addition, I visually compared the time-series images with modeled flow depth to further validate the calibrated channel Manning's coefficient values.

*4.3.4 Model scenarios and analysis*

*4.3.4.1 Floodplain roughness and flow*

For each of the three reaches, I simulated four floodplain roughness scenarios. Scenario 1 was developed using the TreeLS classified stem distribution, computed density, $m$, mean stem diameter, $D_s$, assumed depth, $h$, and the bed roughness value, $C_b$, that was calculated using the calibrated Manning's coefficient value and Equation 4. The spatially variable total roughness coefficient, $C$, was then converted back to Manning's coefficient to use in HEC-RAS. Scenario 2

is a spatially homogenous floodplain Manning's coefficient computed as the mean floodplain roughness value of Scenario 1. The Scenario 3 Manning's coefficient was computed by increasing the vegetation density value, $m$, from Scenario 1 by 0.2 stems/m$^2$. Where vegetation was detected across the floodplain and represents a medium-density floodplain vegetation simulation. The Scenario 4 Manning's coefficient was computed by increasing the vegetation density value, $m$, from Scenario 1 by 0.4 stems/m$^2$ and represents a high-density floodplain vegetation simulation.

Manning's coefficient for Scenarios 1, 3, and 4, were computed as raster grids with 6-m cell size, slightly larger than the HEC-RAS model floodplain computational grid size so that no roughness grid cells were ignored in the model runs. Vegetation density, and stem diameter were also computed for 6-m grid cells. Density was computed as the number of vegetation elements per square meter within the 6-m grid cell, and stem diameter was mean stem diameter of trees within the grid cell.

Three flow rates were simulated for each of the roughness scenarios: 75 m$^3$/s, 100 m$^3$/s, and 150 m$^3$/s. Each flow rate tested was much larger than the discharge sufficient to fill the main channel so that there were observable channel-floodplain interactions to investigate exchange flows. 75 m$^3$/s is a 12-year return interval flood, 100 m$^3$/s is a 25-year return interval flood, and 150 m$^3$/s represents a flood larger than the system has experienced and is an end-member scenario.

*4.3.4.2 Vegetation characteristics and comparison with flume study*

Rigid cylindrical elements simulating floodplain vegetation described in Chapters 2 and 3 had stem diameters that scaled to approximately 0.5-m prototype with a 1:20 length scaling ratio.

This is comparable to the stem diameters estimated using the TreeLS stem detection tool with distributions shown in Figure 4.6.

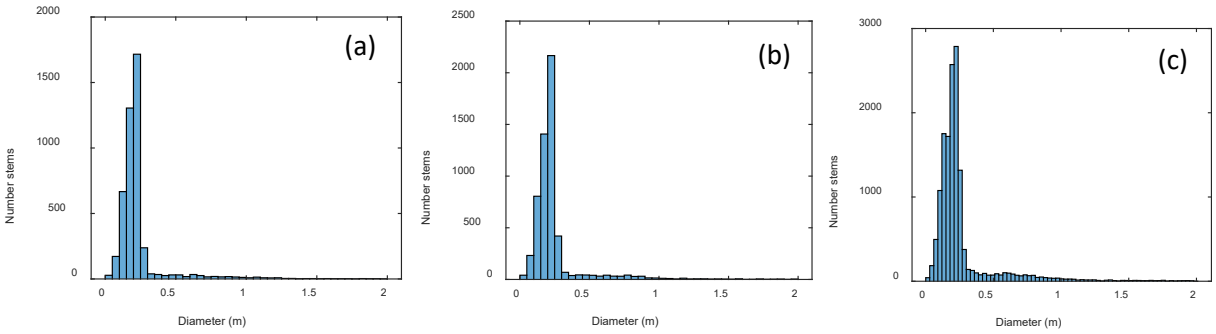


**Figure 4.6.** Stem diameter histograms for (a) Reach 1, (b) Reach 2, and (c) Reach 3.

For comparison, the flume channel scaled at that ratio would be approximately 20-m wide, larger than the Butokamabetsu River, but of similar size that comparison of the model results to the results presented in this chapter has meaningful applicability. Channel slope among the three reaches ranged from 0.005 to 0.011, similar to the slope in the flume experiments (0.007). The stem densities simulated in Chapter 2 and 3 scale to 0 stems/m$^2$ for the bare floodplain runs, 0.008 stems/m$^2$ for the low-density runs, and 0.03 stems/m$^2$ for the high-density runs. This is comparable to the average vegetation densities estimated using the TreeLS stem detection tool in Reach 1 (0.02 stems/m$^2$), Reach 2 (0.04 stems/m$^2$), and Reach 3 (0.09 stems/m$^2$).

*4.3.4.3 Channel-floodplain exchange flow*

I followed methods similar to those outlined in (Czuba et al., 2019) and in Chapter 3 to estimate channel-floodplain hydrologic connectivity as influenced by the four model roughness scenarios. Channel-floodplain exchange was computed at approximately 1.5-m evenly spaced points along the left and right banks following the topographic grade-break that becomes

inundated during floods. The HEC-RAS model outputs including depth, $h$, and velocity, $V$, were interpolated from the flexible computational mesh into an evenly spaced grid with 0.5-m spacing. I then computed bank unit discharge at each bank point a downstream distance, $s$, with superscripts, $L$, or $R$, indicating the left or right bank, respectively. The equation for bank unit discharge was

$$\boldsymbol{q}_s^B = \boldsymbol{U}_s^B h_s^B \tag{5}$$

were $h$ is the depth of flow over the floodplain at each point. I then computed the unit exchange flow, $\widehat{\boldsymbol{q}}_s^B$ at location $(s, B)$ as the dot product of the bank unit discharge and the unit normal vector at distance $s$, and bank $B$, as

$$\widehat{\boldsymbol{q}}_s^B = \boldsymbol{q}_s^B \cdot \widehat{\boldsymbol{n}}_s^B \tag{6}$$

where $\widehat{\boldsymbol{n}}$ is the unit normal vector perpendicular to the channel centerline and oriented away from the channel such that positive unit exchange flux at the right bank would indicate flow exiting the channel, and negative unit exchange flow at the left bank would indicate flow entering the channel. This unit exchange flow can be interpreted in terms of local momentum flux patterns along the channel-floodplain interface since the unit exchange vector scales with momentum. To investigate general patterns of channel-floodplain exchange flows and the influence of floodplain vegetation, I then integrated the unit exchange flow over the length of reach, such that

$$\overline{\hat{q}^B} = \frac{1}{L}\int_0^L \hat{q}^B(s)\, ds \tag{7}$$

where $\overline{\hat{q}^B}$ is the integrated reach unit exchange flow, $\hat{q}^B(s)$, is the unit exchange flow at distance *s*, and *L* is the reach length. I then discretized this integral such that $ds \cong \Delta s$, where $\Delta s$ is the incremental downstream distance (0.5-m). The discretized equation can be written as

$$\overline{\hat{q}^B} = \frac{1}{L}\sum_{i=1}^{n} \hat{q}_i^B \Delta s \tag{8}$$

where $n$ is the number of local exchange flow measurements, and $L$ is the reach length.

## 4.4 Results

### *4.4.1 Estimation of Manning's coefficient due to vegetation*

In Reach 1, the density of rigid vegetation elements ranged from 0 to 0.28 stems/m$^2$ with a mean density of 0.02 stems/m$^2$ (See Figure 4.7a). Stem diameter ranged from 0 to 1.9 m with a mean diameter of 0.1 m. Manning's coefficient in Reach 1 ranged from 0.045 to 0.058 across the floodplain with a mean of 0.046. In Reach 1, much of the floodplain had low-density vegetation with a small patch of high-density vegetation along the channel toward the upstream end of the reach.

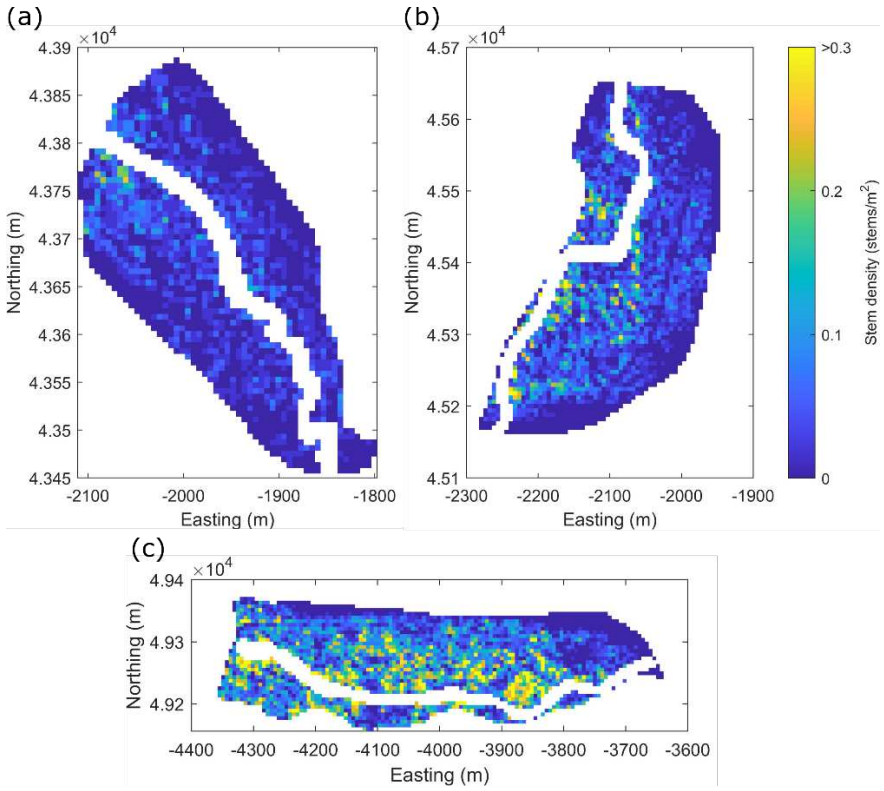


**Figure 4.7**. Floodplain vegetation density for (a) Reach 1, (b) Reach 2, and (c) Reach 3. I verified the point density estimates by overlaying point locations on aerial imagery collected the same day as the LiDAR surveys. Possible errors associated with misidentification of stems or shrubs is described in section 4.3.1.

In Reach 2, the density of rigid vegetation elements ranged from 0 to 0.58 stems/m$^2$ with a mean density of 0.04 stems/m$^2$. Stem diameter ranged from 0 to 1.75 m with a mean diameter of 0.13 m. Manning's coefficient in Reach 2 ranged from 0.045 to 0.068 across the floodplain with a mean of 0.047. Trees were distributed more uniformly across the floodplain in Reach 2 than Reach 1, however, the densest patches were located near the channel and between the main channel and a large side channel (See Figure 4.7b)

In Reach 3, the density of rigid vegetation elements ranged from 0 to 0.59 stems/m$^2$ with a mean density of 0.09 stems/m$^2$ across the floodplain. Stem diameter ranged from 0 to 1.97 m with a mean diameter of 0.17 m. Manning's coefficient in Reach 2 ranged from 0.040 to 0.062

across the floodplain with a mean of 0.043. In Reach 3, there was a very dense patch of trees adjacent to the channel on an island, and in general, Reach 3 had the densest vegetation compared to the other two reaches (See Figure 4.7c). Reach 3 also had trees with the largest mean diameter. Reach 3 is positioned approximately 50 m in elevation higher in the watershed than Reach 2, and approximately 70 m in elevation higher than Reach 1 and may be better suited to the growth of the large birch trees in this reach.

In Figure 4.8, the distribution of Manning's coefficient across the model domain of Reach 2 is displayed to demonstrate the variation in roughness between roughness Scenario 1, 2, 3, and 4. Figure 4.8a, represents the TreeLS surveyed vegetation density and resulting Manning's coefficient distributions, Figure 4.8b shows a reach-averaged roughness value applied to the floodplain, an approach commonly taken by practitioners when calibrated roughness values aren't available, and Figures 4.8c and 4.8d represent the manually increased vegetation density and resulting Manning's coefficient distributions.

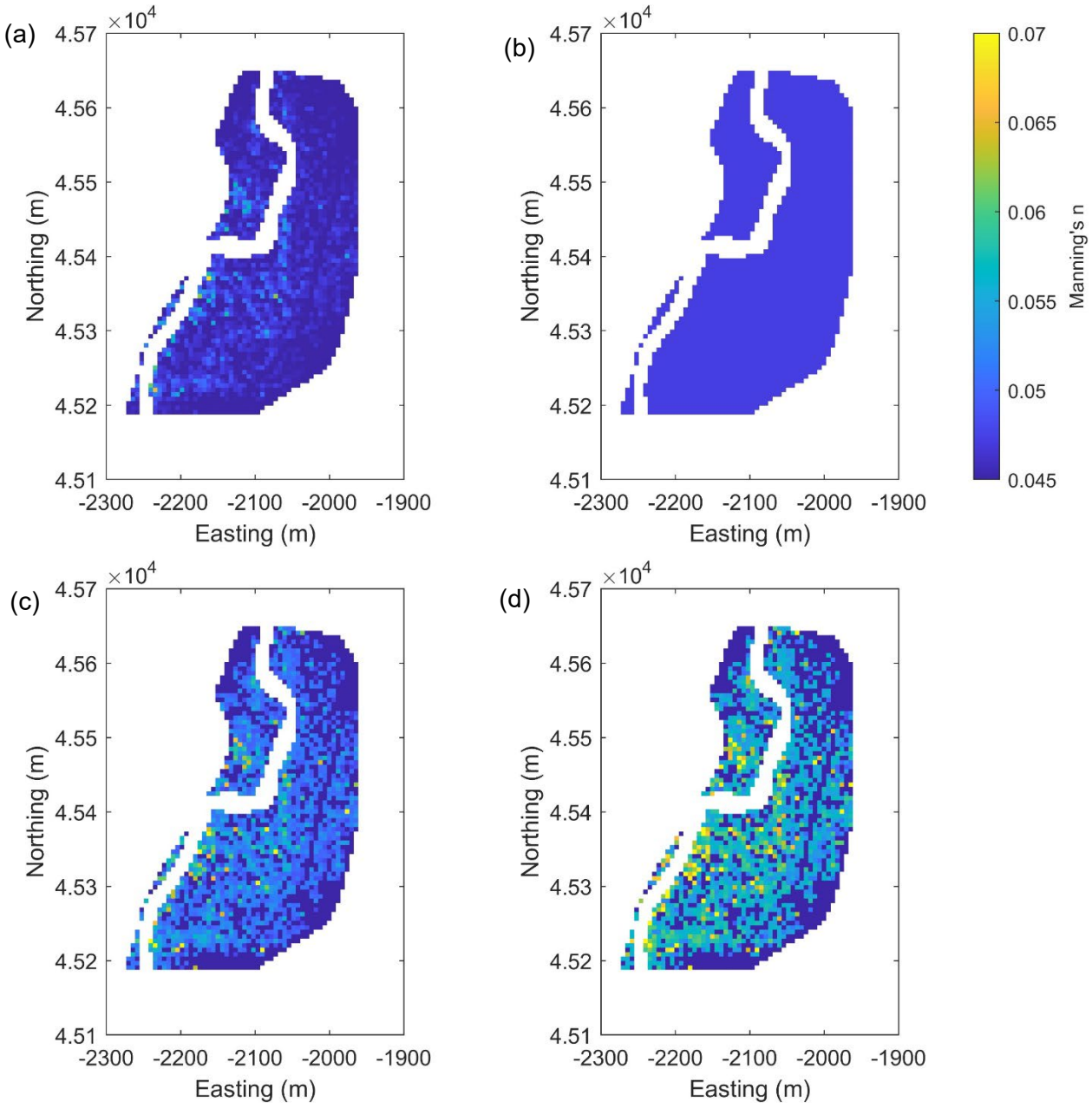


**Figure 4.8**. Floodplain Manning's roughness for four modeled scenarios along Reach 2. (a) Scenario 1. Estimated vegetation density using TreeLS survey output. (b) Scenario 2. Reach-averaged vegetation density applied to floodplain and computed Manning's coefficient. (c) Scenario 3. Density was increased from surveyed values by 0.2 stems/m$^2$ and Manning's coefficient computed. (d) Scenario 4. Density was increased by 0.4 stems/m$^2$ and Manning's coefficient computed.

*4.4.2 Model Results*

I analyze 2D model outputs including depth and velocity. A cursory observation of the distribution of velocity and depth for each of the four floodplain roughness scenarios does not

reveal any significant differences and inundation regions were quite similar for all scenarios as well (See Figure 4.9). This result is different than the results presented in Chapter 3 where high-density vegetation significantly altered the flow field both on the floodplain and within the channel at both overbank flow depths. For all roughness scenarios and in Reaches 1, 2, and 3, highest velocities occurred within the main channel, and in some of the larger side channels that become inundated on an annual basis. Low lying areas adjacent to the main channel experienced moderate flow velocities, and many paleo-channels that become inundated at a less-than yearly basis were flooded during the 75, 100, and 150 $m^3/s$ flows.

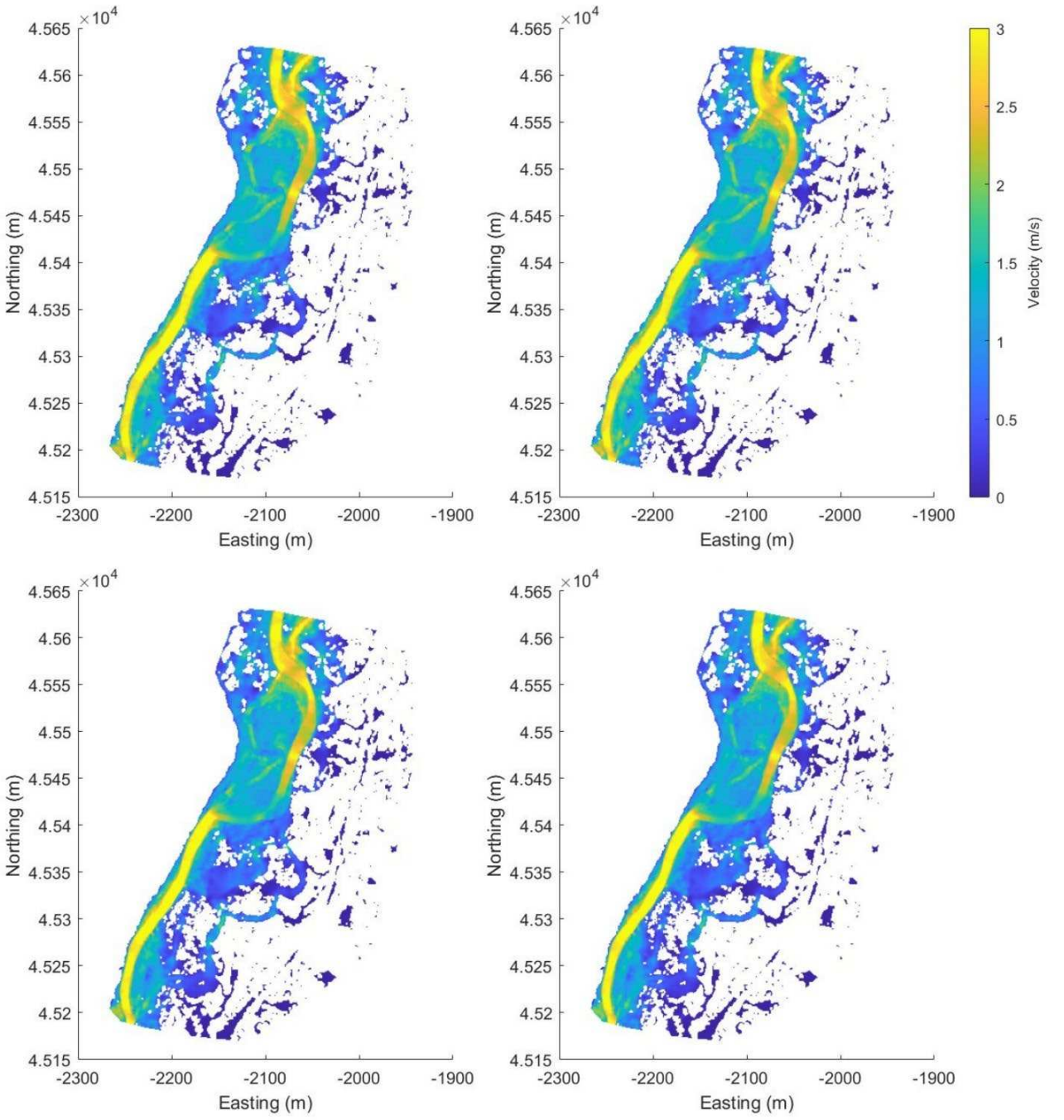


**Figure 4.9.** Velocity distribution from model outputs of Reach 3 at 150 $m^3/s$. (a) Spatially distributed vegetation roughness using TreeLS results. (b) Reach averaged Manning's coefficient. (c) Increased TreeLS density by 0.2 stems/$m^2$ (d) Increased stem density by 0.4 stems/$m^2$.

#### *4.4.2.1 Channel-floodplain exchange flow*

In Figure 4.10, unit exchange flow is depicted as red and blue vectors scaled by the magnitude of flow as it enters and exits the channel. Red vectors represent unit exchange flow at the left bank and blue vectors represent unit exchange flow at the right bank. In general, high unit exchange flow is most closely associated with areas where bank height is low allowing flow to pass freely from channel to floodplain. However, when comparing patches of high-density vegetation adjacent to the bank, there also appears to be less unit exchange flow than in areas where vegetation was absent or where there were patches of low-density vegetation. For example, in Figure 4.10a, the densest vegetation patches were located along the banks at the upstream end of the reach, which also appears to be where the lowest unit exchange flow occurred. In Reach 3 (Figure 4.10c), there was a high-density patch of vegetation adjacent to the channel's left bank, which is also a location where unit exchange flow was lowest.

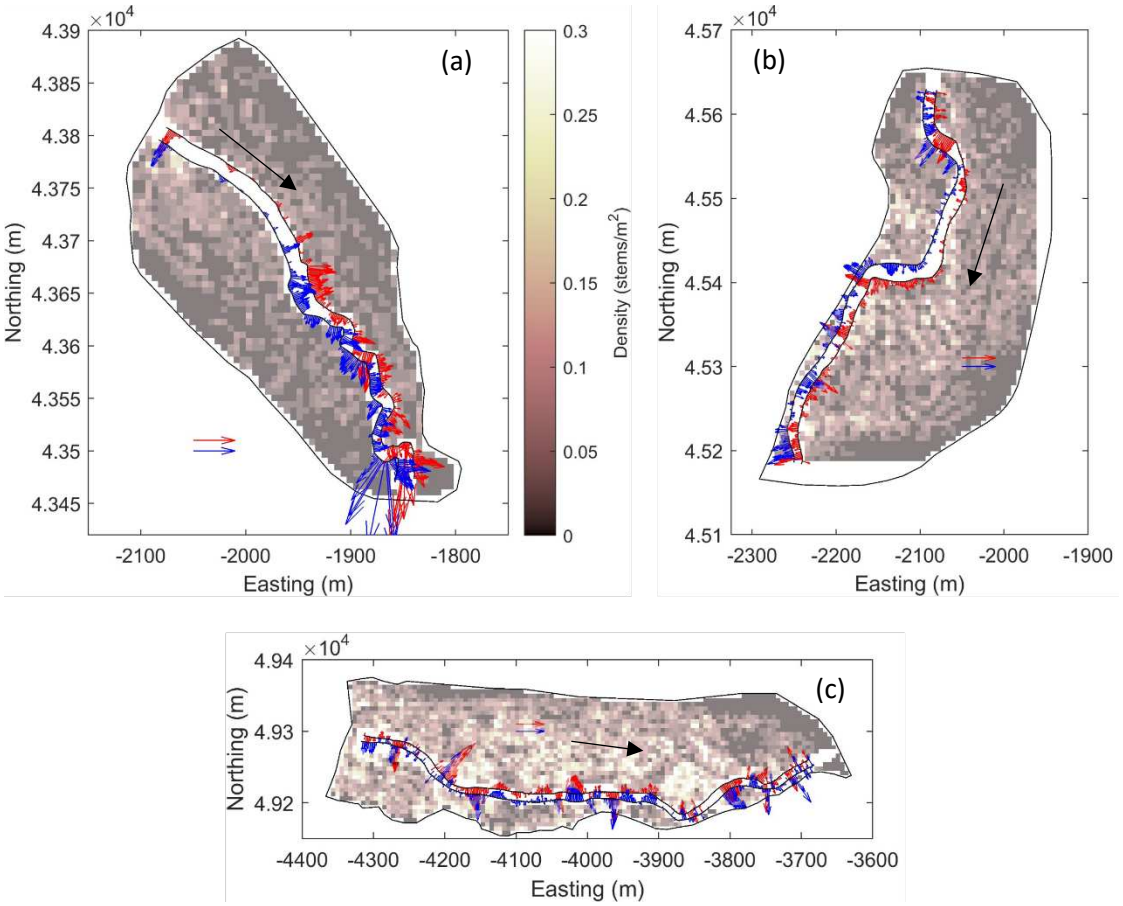


**Figure 4.10.** Unit exchange flow ($m^2/s$) at left and right banks at a discharge of 150 $m^3/s$. Red vectors indicate left bank unit exchange flow magnitude and blue vectors indicate right bank exchange. The black arrow indicates the direction of flow. (a) Reach 2. (b) Reach 2. (c) Reach 3. In all Figures 4.10a, 4.10b, and 4.10c, the red and blue vectors distant from the channel represent 4 $m^2/s$ unit exchange flow.

I computed the magnitude of reach-integrated unit exchange flow, $\overline{\hat{q}^B}$, for all model simulations and compare geomorphic reach characteristics including sinuosity (Figure 4.11) and slope (Figure 4.12). The reach-integrated unit exchange flow was highest for all four floodplain roughness scenarios in Reach 3 at flows of 100 and 150 $m^3/s$. The high unit exchange flow in Reach 3 is likely due in part to a large side channel where the flow exists the main channel at the right bank toward the downstream end of the modeling domain, which can be seen in Figure 4.10a. Had flow not exited the main channel here, reach-integrated unit exchange flow in Reach

3 would have been much lower. An increase in floodplain vegetation density produced a noticeable decrease in reach-integrated unit exchange flow in Reaches 1 and 2; however, unit exchange flow did not vary as greatly in Reach 3. In Figure 4.11, unit exchange flow is compared with the sinuosity of each reach, and I see that in Reaches 1 and 2, the reaches with greater sinuosity, unit exchange flow is more greatly influenced by varied floodplain vegetation density.

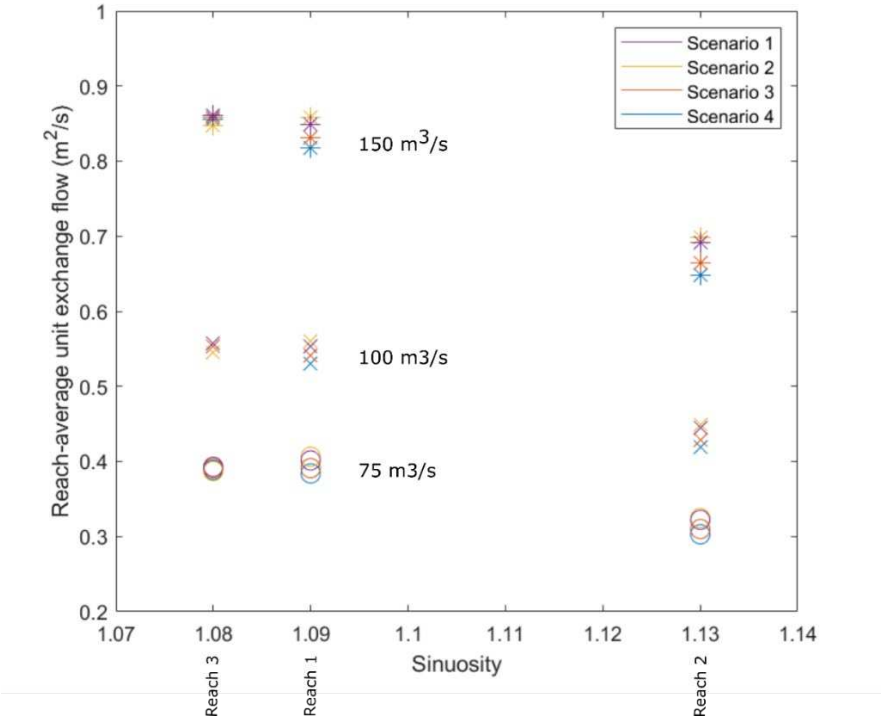


**Figure 4.11.** Reach-averaged unit exchange flow for all 36 model simulations. Asterisks indicate models run at 150 $m^3/s$, x's indicate models run at 100 $m^3/s$, and circles indicate models run at 75 $m^3/s$. There is less variation in unit exchange flow across scenarios in Reach 3, which had the lowest sinuosity. Models run under floodplain roughness values set in Scenario 4 resulted in the least amount of reach-average unit exchange flux for Reaches 1 and 2 across all flow rates.

In Figure 4.12, I compare $\overline{\hat{q}^B}$ with reach-average slope. Reach 3 had a significantly higher slope at 0.011 vs. Reach 2, which has a slope of 0.006 and Reach 1, which has a slope of 0.005. The exchange flow in Reach 3 was least influenced by an increase in vegetation density,

whereas Scenarios 3 and 4 decreased unit exchange flow much more in Reaches 1 and 2. Overall unit exchange flow was lowest in Reach 2.

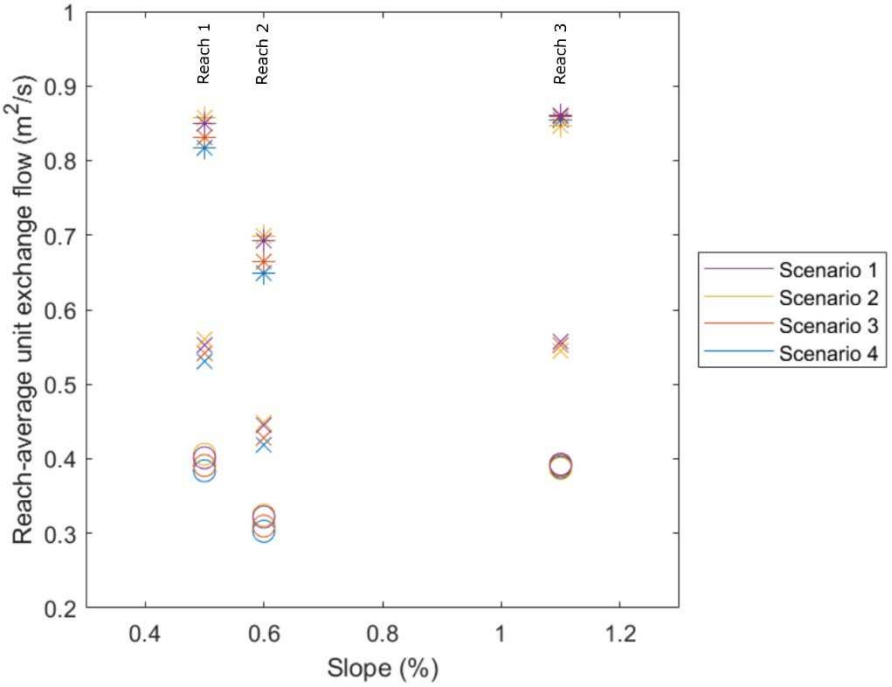


**Figure 4.12.** Reach-average unit exchange flow vs slope.

## 4.5 Discussion

As shown in many studies, flow through vegetation is highly three-dimensional (Nepf, 1999; Tinoco & Coco, 2018; Yager & Schmeeckle, 2013) and this complexity of flow is difficult to simplify to two-dimensional numerical simulations. Because of this, some of the effects that vegetation has on the flow field and its influence on channel-floodplain hydrologic connectivity may not be fully captured in this study. However, the results presented herein do present interesting findings, that are supported by previous studies such as the way in which floodplain vegetation attenuates flow and reduces the magnitude of unit exchange flow at the channel-floodplain boundary.

The Butokamabetsu River is geomorphically distinctive in the abundance of small side channels, many of which are hydrologically connected to the main channel at a range of flows, some at recurrence intervals of less than 0.5 years. These side channels and other topographic irregularities across the floodplain are strong drivers of the floodplain flow dynamics observed in the hydraulic modeling output. As shown by Uno et al. (2022), these side channels provide important refugia and unique habitat for aquatic organisms in this watershed. The magnitude of exchange flux concentrated at main-side-channel confluences accounts for a large volume of exchange flow. In these model scenarios, floodplain vegetation did not have a primary influence on the distribution or magnitude of exchange flows which varies markedly from my flume results where high-density floodplain vegetation significantly slowed flows across the floodplain, increased conveyance within the channel, and decreased unit exchange flow by as much as half compared to the low-density vegetation conditions.

In these model simulation results, flows with high recurrence intervals > 20 years did not completely submerge the floodplain which may have been limiting in the model's ability to fully

analyze flow patterns across the floodplain. This is likely largely in part to the underestimation of hydraulic roughness of the vegetated floodplain.

*4.5.1 Study limitations*

The methods used in this manuscript to quantify floodplain vegetation characteristics do not fully account for the hydraulic roughness due to floodplain topography, shrubs, and other elements that cannot be classified as rigid cylinders. However, the TreeLS package and its associated statistical tools used to segment, classify, and measure physical characteristics of trees in the Butokamabetsu River corridor is shown to be an effective tool. This tool is likely particularly useful for vegetation surveys in river corridors dominated by large woody trees that are closely spaced across the floodplain. To expand its utility and value for hydrodynamic modeling simulations, it would be beneficial to couple the TreeLS package with other point cloud processing methods to quantify a composite Manning's coefficient including various elements such as roughness due to shrubby vegetation, roughness due to grasses, roughness to do topographic floodplain irregularities, and roughness due to surface grain size. Each of these elements have very distinct physical characteristics that require unique tools to accurately account for and estimate a spatially distributed hydraulic roughness map that can be used in 1D, 2D. and 3D numerical modeling and estimation of reach-scale roughness coefficients in data sparse rivers such as the Butokamabetsu. The methods described in this paper to estimate floodplain vegetation roughness can also be improved by iteratively solving for and converging on a floodplain depth value rather than arbitrarily selecting a depth value.

*4.5.2 Future opportunities*

I monitored the effectiveness of the TreeLS stem detection tool by doing a visual inspection of the tiled LiDAR point clouds as they were being processed (i.e. Figure 4.4),

however, because the tool was developed for tree stands with readily detectable, straight, uniformly spaced stems, it may not be as effective in river corridors where trees may be irregularly shaped and spaced. It would be beneficial to perform rigorous statistical analysis of the accuracy of the TreeLS tool.

It would be beneficial to test these methods in a river system where more data are available describing flood stage to accurately calibrate floodplain roughness coefficients and compare the influence of floodplain vegetation compared to total floodplain roughness as well as the effectiveness of the tool. It would also be beneficial to develop an approach using remotely sensed data such as LiDAR to estimate partitioned floodplain roughness elements such as shrubby vegetation, topographic variability, grain size, floodplain side channels, etc. There are tools similar to this that require field surveys (Arcement & Schneider, 1989) and on-the ground measurements such as vegetation frontal area, that may be reframed to use remote sensing.

*4.5.3 Implications for river management*

River managers are often tasked with identifying reaches that may benefit from river restoration projects such as reconnection of the channel and floodplain, construction of in-stream habitat, or planform modifications. Studies have shown that low gradient, low valley confinement reaches often termed ‘beads’ connected in a watershed network by confined, steep ‘string’ reaches may be disproportionately important for increasing watershed resilience (Wohl et al., 2018, 2022). The results presented in this paper support the idea that beads may be important to prioritize in the context of utilizing floodplain vegetation in river restoration, because as shown in Figures 4.11 and 4.12, the low gradient, higher sinuosity reaches showed greater attenuation of channel-floodplain exchange flux than Reach 3, the steeper, less sinuous reach.

River managers may also incorporate the positive benefits of reconnecting channels with vegetated floodplains, particularly in reaches classified as river beads.

### 4.6 Conclusion

I investigated methods to detect and characterize rigid emergent floodplain vegetation near the Butokamabetsu River in Hokkaido, Japan using aerial LiDAR surveys. I then used the measured vegetation characteristics to calculate hydraulic roughness as Manning's coefficient using an empirical relationship developed from flume studies and performed a series of hydraulic modeling simulations in HEC-RAS 2D. In these numerical experiments, I account only for the partitioned roughness coefficient due to vegetation as well as a base surface roughness coefficient and investigate the influence of vegetation density on channel-floodplain hydrologic connectivity by manually increasing stem density to test four floodplain roughness scenarios. A common practice in flood modeling is the use of a reach-wide estimate of floodplain roughness coefficients. In these modeling scenarios, a reach-wide floodplain roughness estimate predicted similar flow dynamics as the spatially varied roughness coefficient dependent on individual plant characteristics. This suggests that either the 2D model poorly captures the hydrodynamic influence of floodplain vegetation on overbank flows, or that perhaps in some situations, a single roughness estimate may be sufficient for river engineering design and analysis when investigating reach-scale flow characteristics.

I estimated channel-floodplain hydrologic connectivity by computing exchange flow at the channel-floodplain boundary along the left and right banks of three reaches with unique geomorphic characteristics including a range of slope and sinuosity. I found the unit exchange flow was greatest along the bank where there were topographic low points regardless of vegetation density. I found that in the reach with highest slope and lowest sinuosity floodplain

vegetation density has a smaller influence on channel-floodplain hydrologic connectivity than in more sinuous, lower gradient reaches. I found that high density vegetation attenuates channel-floodplain exchange flow more than low density vegetation. These observations are similar to those presented in Chapter 3 of this dissertation and highlight the influence of floodplain vegetation on river-corridor connectivity dynamics. In future work, the tools used to estimate floodplain vegetation characteristics could be combined with other remote sensing tools to parameterize hydraulic roughness of floodplains due to leafy, shrubby vegetation, large wood, topographic variability, and other roughness elements to produce a representative estimate of total floodplain hydraulic roughness coefficients for accurate hydraulic modeling.

## 4.7 References

Aberle, J., & Järvelä, J. (2013). Flow resistance of emergent rigid and flexible floodplain vegetation. *Journal of Hydraulic Research*, *51*(1), 33–45. https://doi.org/10.1080/00221686.2012.754795

Anderson, B. G., Rutherfurd, I. D., & Western, A. W. (2006). An analysis of the influence of riparian vegetation on the propagation of flood waves. *Environmental Modelling & Software*, *21*(9), 1290–1296. https://doi.org/10.1016/j.envsoft.2005.04.027

Arcement, G. J., & Schneider, V. R. (1989). *Guide for selecting Manning's roughness coefficients for natural channels and flood plains* (Report No. 2339). https://doi.org/10.3133/wsp2339

Baldwin, D. S., & Mitchell, A. (2000). The effects of drying and re-flooding on the sediment and soil nutrient dynamics of lowland river–floodplain systems: a synthesis. *Regulated Rivers: Research & Management: An International Journal Devoted to River Research and Management*, *16*(5), 457–467.

Baptist, M. J., Babovic, V., Uthurburu, J. R., Keijzer, M., Uittenbogaard, R. E., Mynett, A., & Verwey, A. (2007). On inducing equations for vegetation resistance. *Journal of Hydraulic Research*, *45*(4), 435–450. https://doi.org/10.1080/00221686.2007.9521778

Benke, A. C. (2001). Importance of flood regime to invertebrate habitat in an unregulated river–floodplain ecosystem. *Journal of the North American Benthological Society*, *20*(2), 225–240.

Boulange, J., Hanasaki, N., Yamazaki, D., & Pokhrel, Y. (2021). Role of dams in reducing global flood exposure under climate change. *Nature Communications*, *12*(1), 417.

Box, W., Järvelä, J., & Västilä, K. (2022). New formulas addressing flow resistance of floodplain vegetation from emergent to submerged conditions. *International Journal of River Basin Management*, 1–17.

Chaulagain, S., Stone, M. C., Dombroski, D., Gillihan, T., Chen, L., & Zhang, S. (2022). An investigation into remote sensing techniques and field observations to model hydraulic roughness from riparian vegetation. *River Research and Applications*, *38*(10), 1730–1745. https://doi.org/10.1002/rra.4053

de Conto, T., Olofsson, K., Görgens, E. B., Rodriguez, L. C. E., & Almeida, G. (2017). Performance of stem denoising and stem modelling algorithms on single tree point clouds from terrestrial laser scanning. *Computers and Electronics in Agriculture*, *143*, 165–176. https://doi.org/10.1016/j.compag.2017.10.019

Czuba, J. A., David, S. R., Edmonds, D. A., & Ward, A. S. (2019). Dynamics of Surface-Water Connectivity in a Low-Gradient Meandering River Floodplain. *Water Resources Research*, *55*(3), 1849–1870. https://doi.org/10.1029/2018WR023527

Dosskey, M. G., Vidon, P., Gurwick, N. P., Allan, C. J., Duval, T. P., & Lowrance, R. (2010). The role of riparian vegetation in protecting and improving chemical water quality in streams 1. *JAWRA Journal of the American Water Resources Association*, *46*(2), 261–277.

Elosegi, A., & Sabater, S. (2013). Effects of hydromorphological impacts on river ecosystem functioning: a review and suggestions for assessing ecological impacts. *Hydrobiologia*, *712*(1), 129–143. https://doi.org/10.1007/s10750-012-1226-6

Gregory, K. J. (2006). The human role in changing river channels. *Geomorphology*, *79*(3–4), 172–191.

Gregory, S., Wildman, R., Hulse, D., Ashkenas, L., & Boyer, K. (2019). Historical changes in hydrology, geomorphology, and floodplain vegetation of the Willamette River, Oregon. *River Research and Applications*, *35*(8), 1279–1290.

Harvey, J., & Gooseff, M. (2015). River corridor science: Hydrologic exchange and ecological consequences from bedforms to basins. *Water Resources Research*, *51*(9), 6893–6922. https://doi.org/10.1002/2015WR017617

Helton, A. M., Poole, G. C., Payn, R. A., Izurieta, C., & Stanford, J. A. (2014). Relative influences of the river channel, floodplain surface, and alluvial aquifer on simulated hydrologic residence time in a montane river floodplain. *Geomorphology*, *205*, 17–26. https://doi.org/10.1016/j.geomorph.2012.01.004

Henriques, M., McVicar, T. R., Holland, K. L., & Daly, E. (2022). Riparian vegetation and geomorphological interactions in anabranching rivers: A global review. *Ecohydrology*, *15*(2), e2370.

Hershey, J. L., McDill, M. E., Miller, D. A., Holderman, B., & Michael, J. H. (2022). A Voxel-Based Individual Tree Stem Detection Method Using Airborne LiDAR in Mature Northeastern U.S. Forests. *Remote Sensing*, *14*(3), 806. https://doi.org/10.3390/rs14030806

Ielpi, A., & Lapôtre, M. G. (2020). A tenfold slowdown in river meander migration driven by plant life. *Nature Geoscience*, *13*(1), 82–86.

Isibue, E. W., & Pingel, T. J. (2020). Unmanned aerial vehicle based measurement of urban forests. *Urban Forestry & Urban Greening*, *48*, 126574. https://doi.org/10.1016/j.ufug.2019.126574

Junk, W. J., Bayley, P. B., & Sparks, R. E. (1989). The flood pulse concept in river-floodplain systems. *Canadian Special Publication of Fisheries and Aquatic Sciences*, *106*(1), 110–127.

Knox, R., Wohl, E., & Morrison, R. (2021, December 24). A River Ran Through It: Floodplains as America's Newest Relict Landform [poster]. https://doi.org/10.1002/essoar.10509835.1

Knox, R. L., Wohl, E. E., & Morrison, R. R. (2022). Levees don't protect, they disconnect: A critical review of how artificial levees impact floodplain functions. *Science of the Total Environment*, *837*, 155773.

Kondolf, G. M. (1997). PROFILE: Hungry Water: Effects of Dams and Gravel Mining on River Channels. *Environmental Management*, *21*(4), 533–551. https://doi.org/10.1007/s002679900048

Lininger, K. B., & Latrubesse, E. M. (2016). Flooding hydrology and peak discharge attenuation along the middle Araguaia River in central Brazil. *CATENA*, *143*, 90–101. https://doi.org/10.1016/j.catena.2016.03.043

Luhar, M., & Nepf, H. M. (2013). From the blade scale to the reach scale: A characterization of aquatic vegetative drag. *Advances in Water Resources*, *51*, 305–316.

McCallum, A. M., Andersen, M. S., Rau, G. C., Larsen, J. R., & Acworth, R. I. (2014). River-aquifer interactions in a semiarid environment investigated using point and reach measurements. *Water Resources Research*, *50*(4), 2815–2829. https://doi.org/10.1002/2012WR012922

McCluney, K. E., Poff, N. L., Palmer, M. A., Thorp, J. H., Poole, G. C., Williams, B. S., et al. (2014). Riverine macrosystems ecology: sensitivity, resistance, and resilience of whole river basins with human alterations. *Frontiers in Ecology and the Environment*, *12*(1), 48–58. https://doi.org/10.1890/120367

Nehal, L., Yan, Z., Xia, J., & Khaldi, A. (2012). Flow through non-submerged vegetation: A flume experiment with artificial vegetation. Presented at the 6 th International Water Technology Conference, Istanbul, Turkey, Citeseer.

Nepf, H. M. (1999). Drag, turbulence, and diffusion in flow through emergent vegetation. *Water Resources Research*, *35*(2), 479–489.

Nilsson, C., & Dynesius, M. (1994). Ecological effects of river regulation on mammals and birds: A review. *Regulated Rivers: Research & Management*, *9*(1), 45–53. https://doi.org/10.1002/rrr.3450090105

Nilsson, C., Reidy, C. A., Dynesius, M., & Revenga, C. (2005). Fragmentation and Flow Regulation of the World's Large River Systems. *Science*, *308*(5720), 405–408. https://doi.org/10.1126/science.1107887

Olde Venterink, H., Vermaat, J. E., Pronk, M., Wiegman, F., van der Lee, G. E. M., van den Hoorn, M. W., et al. (2006). Importance of sediment deposition and denitrification for nutrient retention in floodplain wetlands. *Applied Vegetation Science*, *9*(2), 163–174. https://doi.org/10.1111/j.1654-109X.2006.tb00665.x

Poff, N. L., Allan, J. D., Bain, M. B., Karr, J. R., Prestegaard, K. L., Richter, B. D., et al. (1997). The Natural Flow Regime. *BioScience*, *47*(11), 769–784. https://doi.org/10.2307/1313099

Sholtes, J. S., & Doyle, M. W. (2011). Effect of Channel Restoration on Flood Wave Attenuation. *Journal of Hydraulic Engineering*, *137*(2), 196–208. https://doi.org/10.1061/(ASCE)HY.1943-7900.0000294

Thoms, M. C. (2003). Floodplain–river ecosystems: lateral connections and the implications of human interference. *Geomorphology*, *56*(3), 335–349. https://doi.org/10.1016/S0169-555X(03)00160-0

Tinoco, R. O., & Coco, G. (2018). Turbulence as the Main Driver of Resuspension in Oscillatory Flow Through Vegetation. *Journal of Geophysical Research: Earth Surface*, *123*(5), 891–904. https://doi.org/10.1002/2017JF004504

TreeLS. (2023). Retrieved from https://github.com/tiagodc/TreeLS

Uno, H., Yokoi, M., Fukushima, K., Kanno, Y., Kishida, O., Mamiya, W., et al. (2022). Spatially variable hydrological and biological processes shape diverse post-flood aquatic communities. *Freshwater Biology*, *67*(3), 549–563. https://doi.org/10.1111/fwb.13862

Windrim, L., & Bryson, M. (2020). Detection, Segmentation, and Model Fitting of Individual Tree Stems from Airborne Laser Scanning of Forests Using Deep Learning. *Remote Sensing*, *12*(9), 1469. https://doi.org/10.3390/rs12091469

Wohl, E. (2017). Connectivity in rivers. *Progress in Physical Geography: Earth and Environment*, *41*(3), 345–362. https://doi.org/10.1177/0309133317714972

Wohl, E. (2019). Forgotten legacies: understanding and mitigating historical human alterations of river corridors. *Water Resources Research*, *55*(7), 5181–5201.

Wohl, E., Lininger, K. B., & Scott, D. N. (2018). River beads as a conceptual framework for building carbon storage and resilience to extreme climate events into river management. *Biogeochemistry*, *141*(3), 365–383. https://doi.org/10.1007/s10533-017-0397-7

Wohl, E., Marshall, A. E., Scamardo, J., White, D., & Morrison, R. R. (2022). Biogeomorphic influences on river corridor resilience to wildfire disturbances in a mountain stream of the Southern Rockies, USA. *Science of The Total Environment*, *820*, 153321. https://doi.org/10.1016/j.scitotenv.2022.153321

Yager, E. M., & Schmeeckle, M. W. (2013). The influence of vegetation on turbulence and bed load transport. *Journal of Geophysical Research: Earth Surface*, *118*(3), 1585–1601. https://doi.org/10.1002/jgrf.20085

Zhu, X., Skidmore, A. K., Darvishzadeh, R., Niemann, K. O., Liu, J., Shi, Y., & Wang, T. (2018). Foliar and woody materials discriminated using terrestrial LiDAR in a mixed natural forest. *International Journal of Applied Earth Observation and Geoinformation*, *64*, 43–50. https://doi.org/10.1016/j.jag.2017.09.004

# CHAPTER 5: CONCLUSION

## 5.1 Key findings

Global rising flood risk places importance on using science-based management strategies to mitigate the negative impacts of floods. One of these strategies is floodplain reconnection. Connected floodplains give floods space to spread out, decreasing pressure on other flood mitigation infrastructure such as dams and levees, and providing critical habitat. Understanding the interaction of flow and vegetation during floods and exchange fluxes at the channel-floodplain interface will help managers predict and plan for flood conditions. In this dissertation, I present the results of physical and numerical experiments that elucidate the physical processes associated with channel-floodplain interactions as they relate to vegetation.

In Chapter 2, I describe the physical modeling experiments conducted at Colorado State University's Hydraulics Laboratory and describe channel topographic response to varied floodplain vegetation density and flow depth. I found that increasing floodplain vegetation density resulted in greater bedform topographic complexity within the channel at two flood depths, and that at both overbank flow depths, sediment transport was greater than at bankfull. This result is distinct from other meandering compound flume experiments with mobile beds and prompts further investigation into this distinction and possible relation to channel planform.

In Chapter 3, I present results analyzing the flow field and show that increased vegetation density results in a decrease in channel-floodplain exchange flow. I also describe the three-dimensional flow field within the channel that results from varied floodplain vegetation configurations and identify the mechanisms that resulted in highly variable secondary currents across the experiments. During the high-density model scenarios, the secondary helical flow field

was more cohesive with well-defined cells. In model scenarios where no vegetation was present, the flow field appeared much more irregular with less distinct secondary flow patterns.

In Chapter 4, I present the results of a series of numerical modeling experiments in which floodplain vegetation was identified and classified through the use of remote sensing tools. The physical characteristics of the floodplain vegetation were then used to compute Manning's roughness coefficients and map them spatially across the floodplain for three reaches of the Butokamabetsu River in Hokkaido, Japan. I then compared 2D hydraulic modeling outputs using the estimated vegetation Manning's n with three other floodplain roughness scenarios. In these numerical modeling experiments, I found that increasing floodplain vegetation density results in a slight increase in attenuation of channel-floodplain exchange flows, similar to the results of Chapter 3. I also found that in the two reaches with higher sinuosity and lower valley gradient, increasing floodplain vegetation density had a more significant influence on the rate of channel-floodplain exchange flows than in the reach with high slope and low sinuosity. The 2D hydraulic model did not, however, capture the effects of high-density floodplain vegetation that we observed in Chapters 2 and 3 where floodplain flow velocity was significantly lower than bare and low-density floodplain vegetation.

Similar conceptual takeaways emerge from these three dissertation chapters. Flow through vegetated floodplains is highly three-dimensional influencing channel-forming forces in ways that are difficult to approximate with the use of depth-averaged relationships or 2D hydraulic models. Although not the primary focus of this dissertation, each chapter points to the fact that channel planform and slope, when analyzed in the context of existing scientific literature, develop hydrodynamic feedbacks with floodplain vegetative cover. Planning for

channel equilibrium processes and optimizing beneficial services provided by vegetated river-corridors can by optimized when considering these results.

**5.2 Floodplain vegetation in the context of river management**

In Chapters 2 and 4 of this dissertation the results indicate that the beneficial characteristics of floodplain vegetation such as channel-floodplain exchange and sediment flux attenuation are accentuated in channels with higher sinuosity. The term 'beads' has been used to describe low gradient, wide, unconfined valley reaches within a larger watershed network that are connected by steep, narrow reaches termed 'strings'. River managers are often tasked with selecting sites where river restoration activities will be most effective or where the river is most degraded. Planning for and incorporating vegetation planting schemes in-conjunction with bead site selection may prove effective to achieve project targets.

In Chapter 4, I tested remote sensing tools that may be utilized by hydraulic engineers to estimate the effects of floodplain vegetation on flow dynamics through meandering channels. I found that the scale of modeling analysis is particularly important to consider when utilizing tools such as remote sensing of floodplain vegetation characteristics. Upon analysis of the results, it appears that the 2D hydraulic model did not fully capture the effect of increased vegetation-density on channel-floodplain hydraulic connectivity that was documented in Chapter 3. Flow through vegetation is complex and highly three-dimensional and additional empirical relationships describing the enhanced 3D flow structure in simplified 2D terms, would be beneficial for predicting flood hydraulics.

In conclusion, with support from many other studies, I find that river processes are not simply limited to the interaction of flow and sediment. Biological drivers such as rigid vegetation heavily influence hydrodynamics in meandering rivers in ways that must be considered for

effective river-corridor management and science in the face of changing global hydrologic conditions, societal challenges, and to sustain functional ecosystems around the world.

# APPENDIX

Supplemental Figures A1 through A7 include all velocity measurements taken within the channel using the P-ADV.

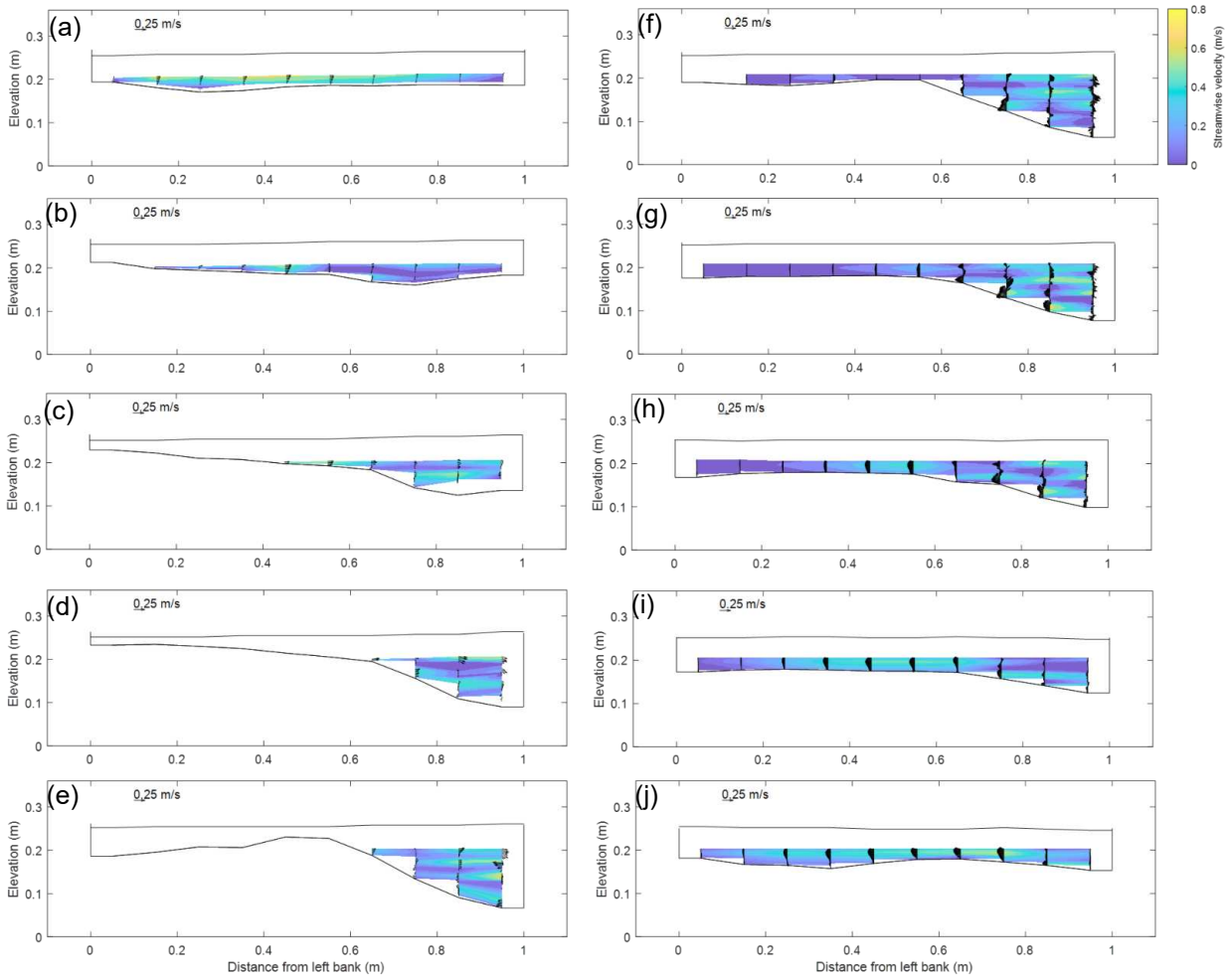


**Figure A1.** Run 1. Bankfull depth. (a-j) Cross sections 1-10 listed following sub heading alphabetic order.

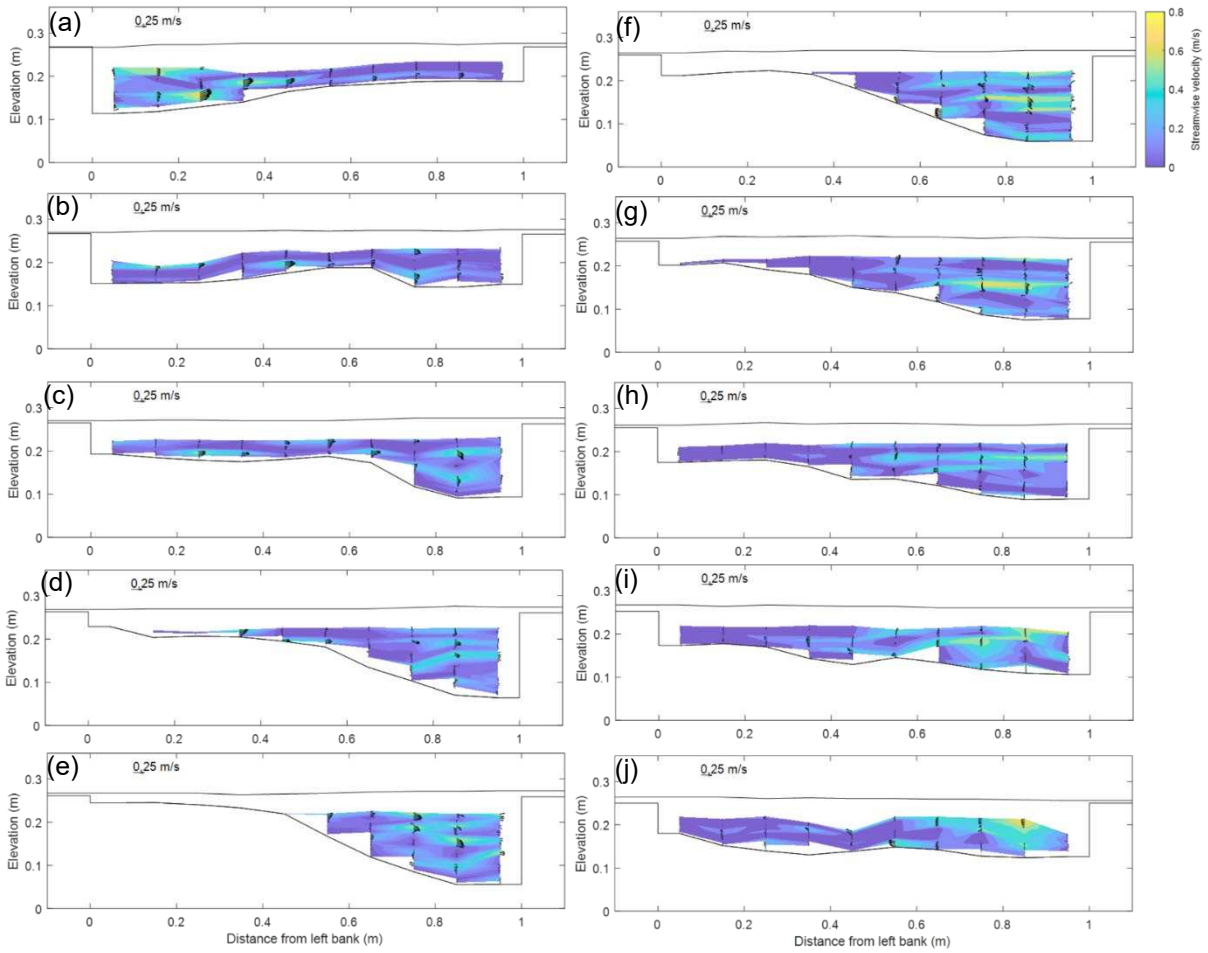


**Figure A2.** Run 2. Bare floodplain, $D_r = 0.1$. (a-j) Cross sections 1-10 listed following sub heading alphabetic order.

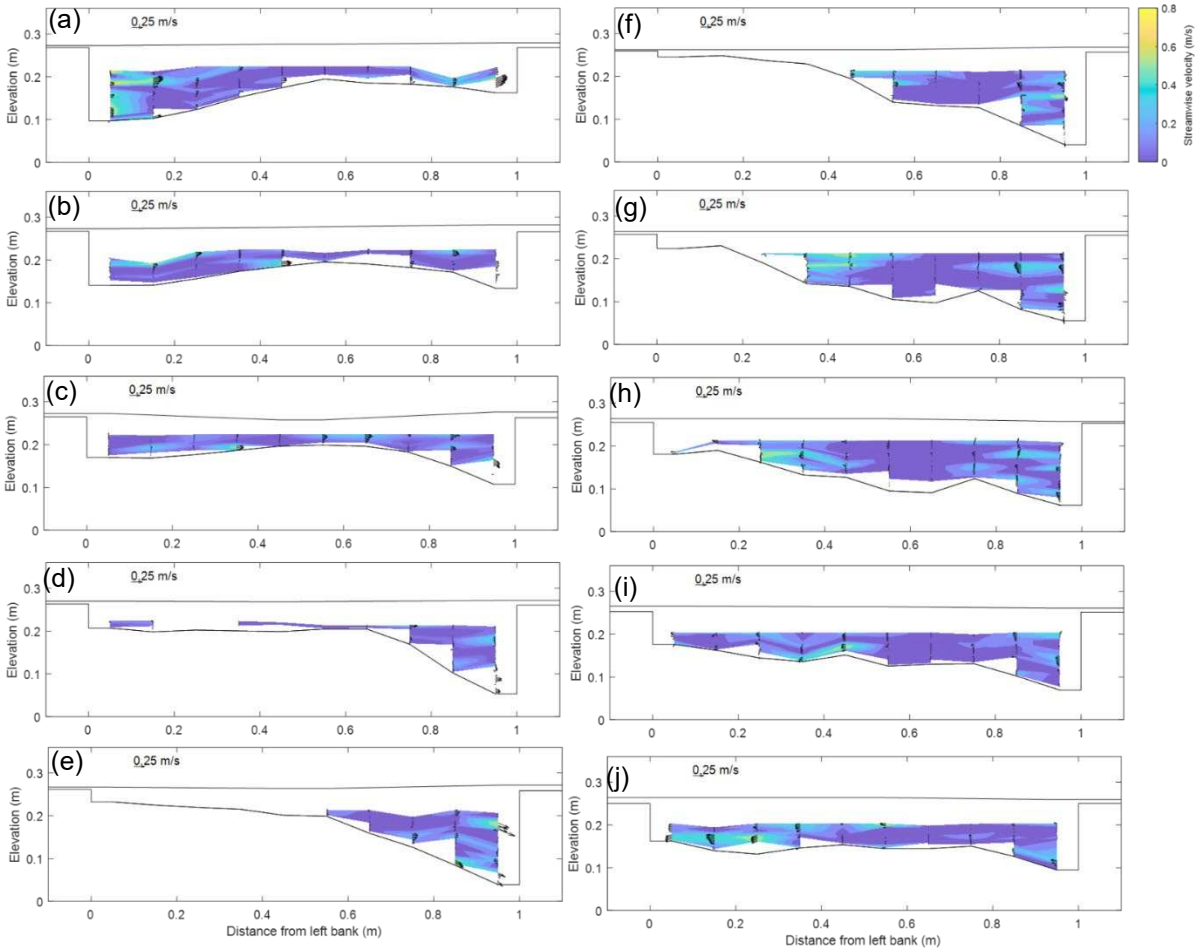


**Figure A3.** Run 3. Low-density vegetation, $D_r = 0.1$. (a-j) Cross sections 1-10 listed following sub heading alphabetic order.

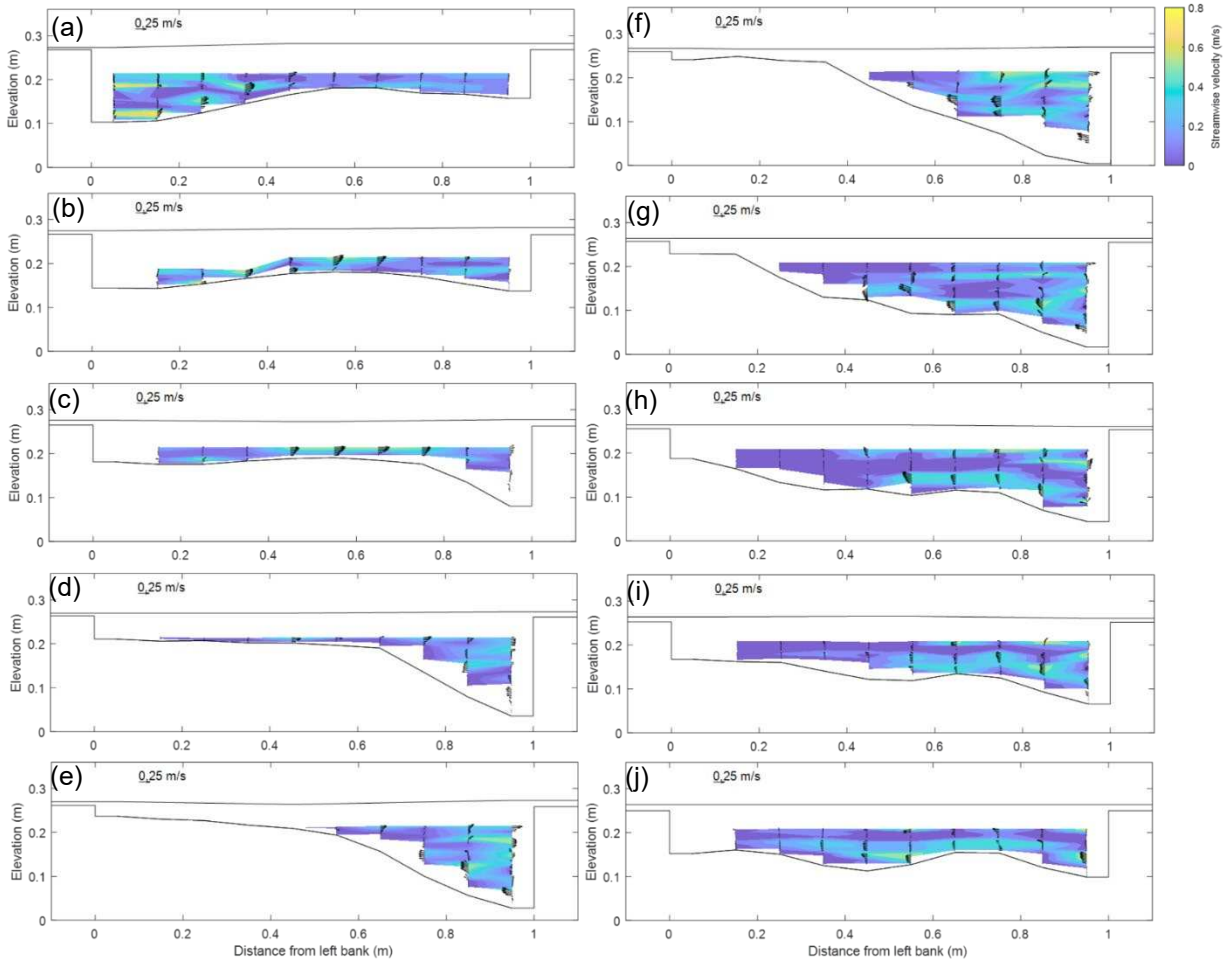


**Figure A4.** Run 4. High-density vegetation, $D_r = 0.1$. (a-j) Cross sections 1-10 listed following sub heading alphabetic order.

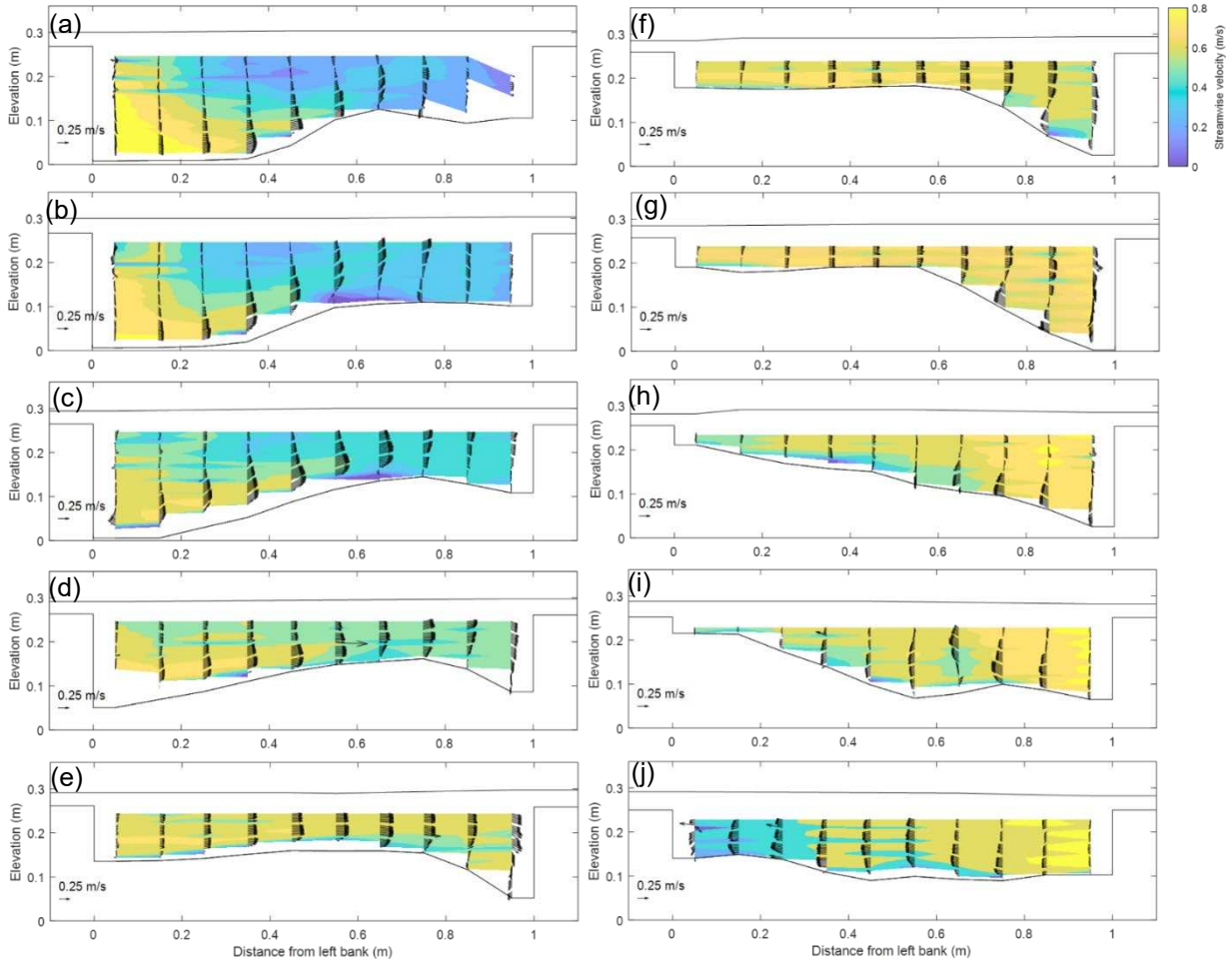


**Figure A5.** Run 5. High-density vegetation, $D_r = 0.25$. (a-j) Cross sections 1-10 listed following sub heading alphabetic order.

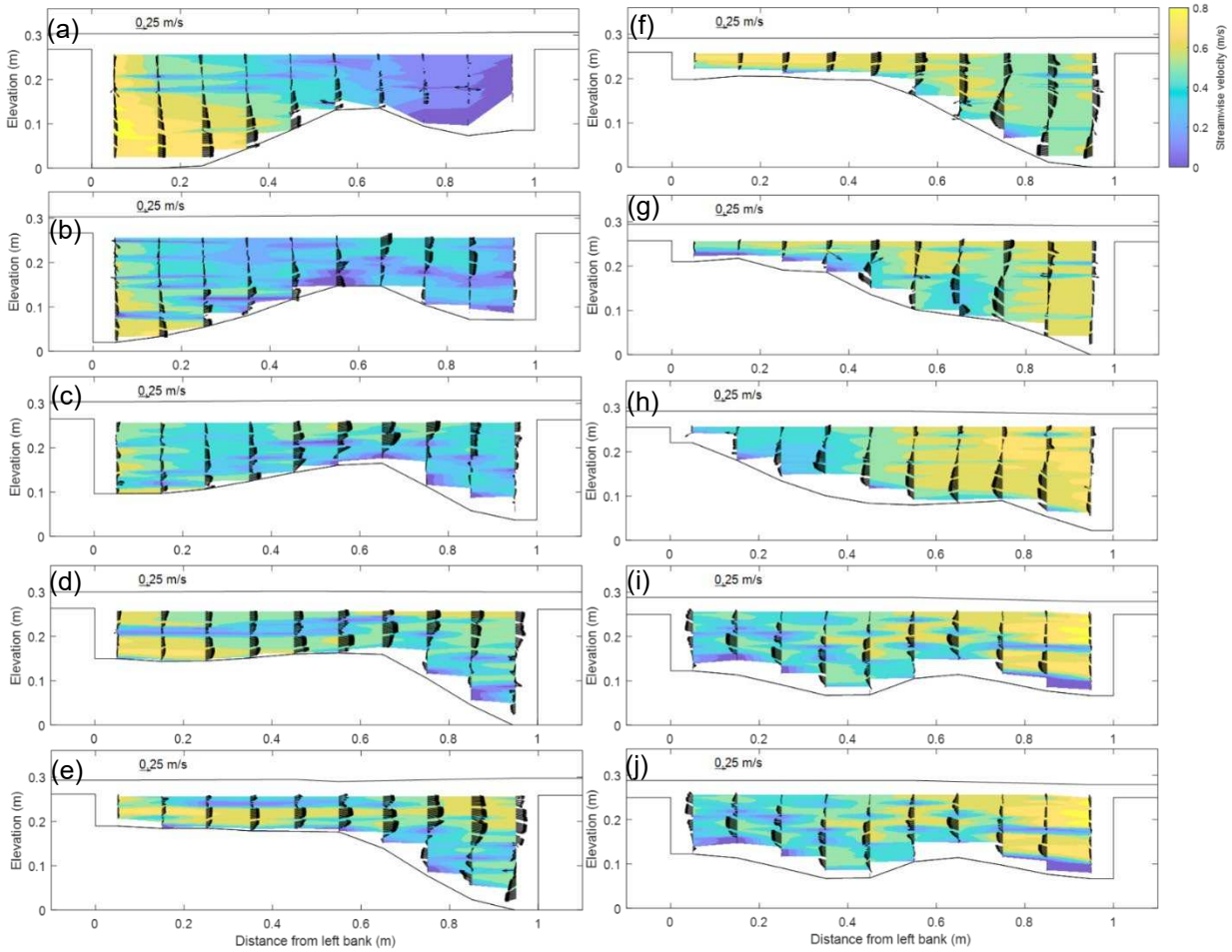


**Figure A6.** Run 6. Low-density vegetation, $D_r = 0.25$. (a-j) Cross sections 1-10 listed following sub heading alphabetic order.

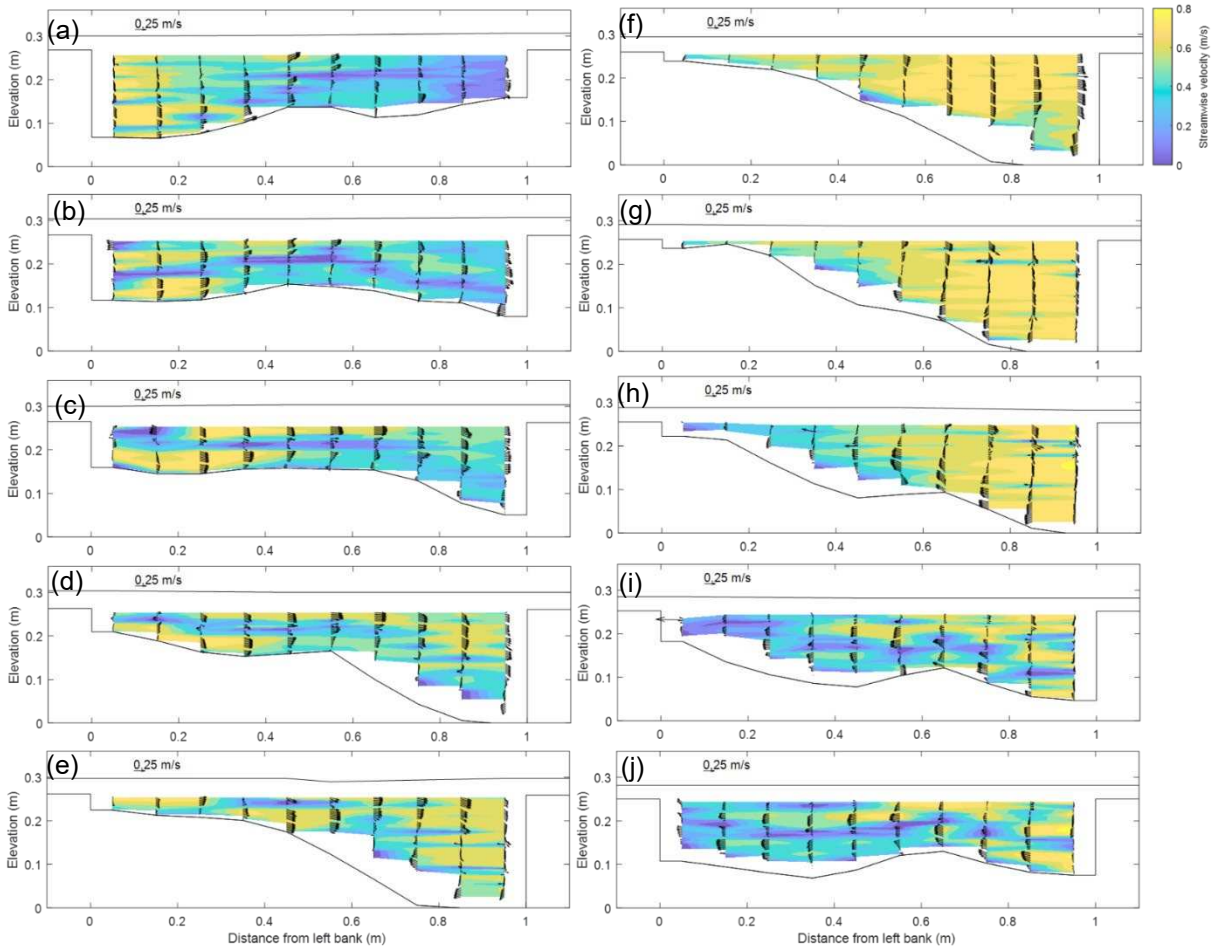


**Figure A7.** Run 6. Bare floodplain, $D_r = 0.25$. (a-j) Cross sections 1-10 listed following sub heading alphabetic order.

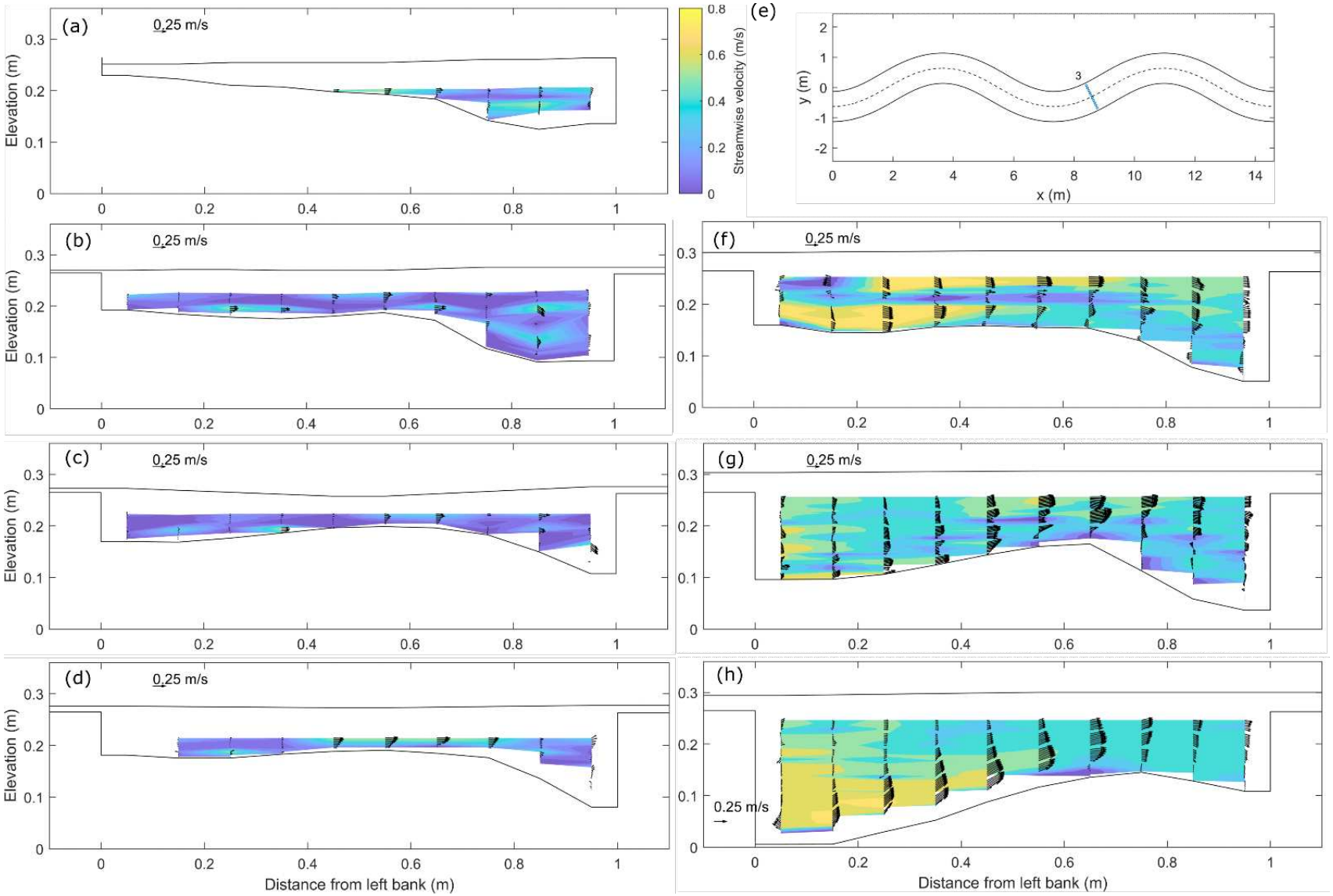


**Figure A8**. XS 3 Cross over region. (a) Run 1. (b) Run 2. (c) Run 3. (d) Run 4. (e) Flume schematic. (f) Run 5. (g) Run 6. (h) Run 7.

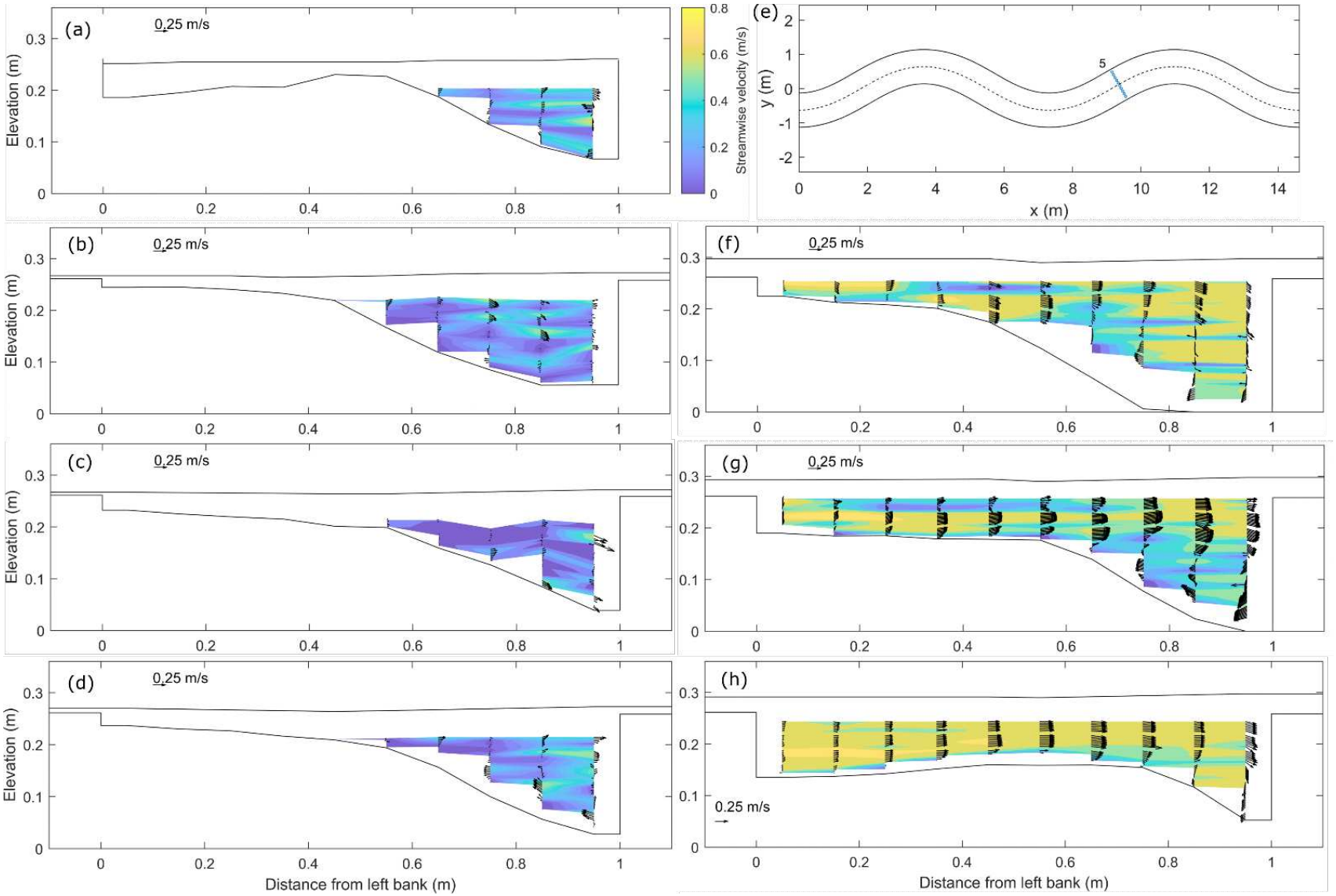


**Figure A9**. XS 5 (a) Run 1. (b) Run 2. (c) Run 3. (d) Run 4. (e) Flume schematic. (f) Run 5. (g) Run 6. (h) Run 7.

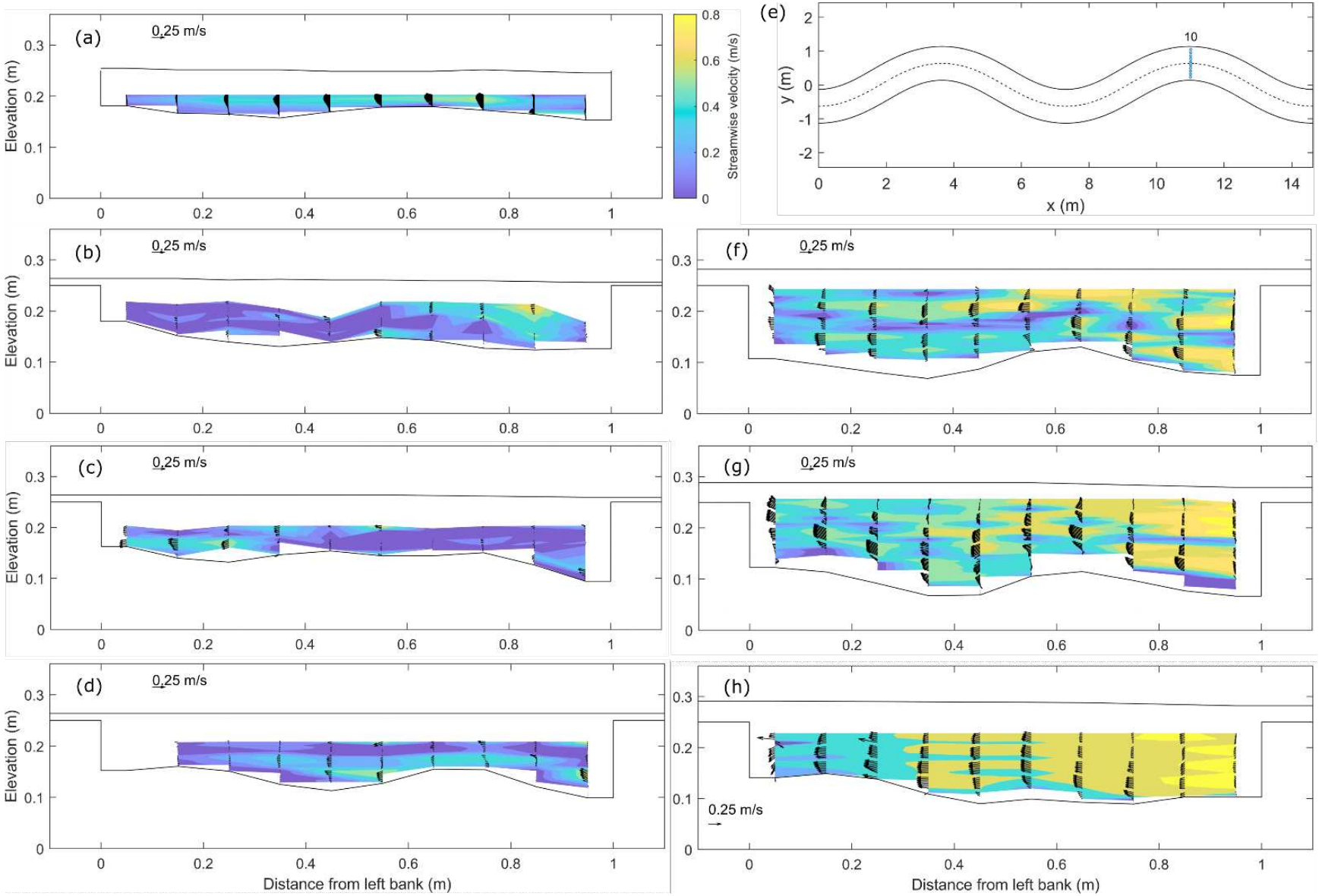


**Figure A10**. XS 10. (a) Run 1. (b) Run 2. (c) Run 3. (d) Run 4. (e) Flume schematic. (f) Run 5. (g) Run 6. (h) Run 7.

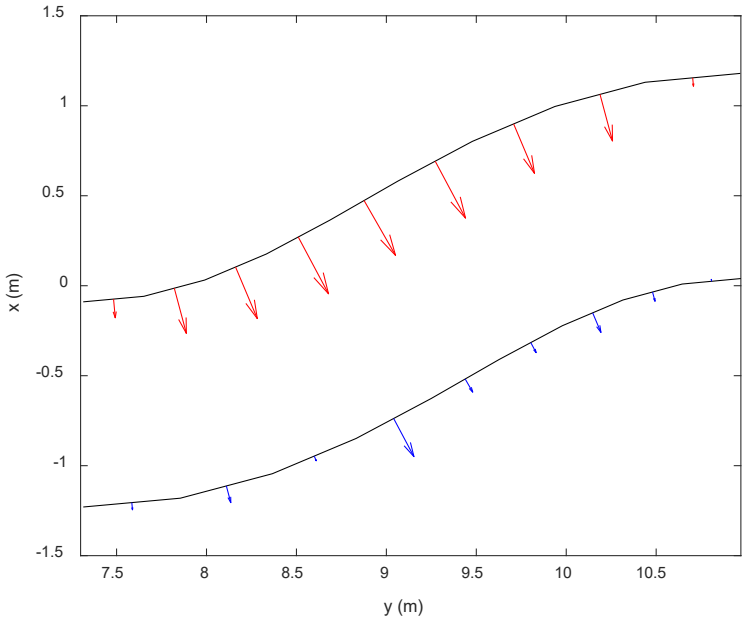


**Figure A11.** Graphical representation of channel-floodplain exchange flux during Run 7 as represented by lateral component of unit discharge vectors at nine points along the half meander of interest.